Azimuthal Asymmetries in polarized Vector-Meson Production at the COMPASS Experiment

Jochen Barwind

Physikalisches Institut
Albert-Ludwigs-Universität Freiburg

Azimuthal Asymmetries in polarized Vector-Meson Production at the COMPASS Experiment

Diplomarbeit

vorgelegt
von

Jochen Barwind

Physikalisches Institut
Albert-Ludwigs-Universität
Freiburg

Oktober 2008

Contents

List of Figures VI

List of Tables VII

1 Introduction 1

2 Theoretical Motivation 3

2.1 Inclusive Deep Inelastic Scattering 3

2.1.1 Kinematical Variables 3

2.1.2 Cross Section 4

2.1.3 Parton Distribution Functions and Structure Functions 5

2.2 Semi-Inclusive Deep Inelastic Scattering 7

2.3 Exclusive Deep Inelastic Scattering 8

2.3.1 Generalized Parton Distribution Functions 9

2.3.2 Hard Exclusive Meson Production 11

2.3.3 Deeply Virtual Compton Scattering 13

2.3.4 Transverse-Target Single-Spin Asymmetry 14

3 The COMPASS Experiment 17

3.1 The Beam 17

3.2 The Polarized Target 17

3.3 The COMPASS Spectrometer 19

3.3.1 Tracking Detectors 19

3.3.2 Particle Identification 20

3.3.3 Trigger System and Front End Electronics 21

3.4 Data Reconstruction and Initial Data Sample 21

4 Target Position, Data Quality and Event Selection **23**

4.1 Target Position 23

4.1.1 General Remarks 24

4.1.2 Target Position in Z-Direction 25

4.1.3 Target Position in the XY-Plane 26

4.2 Data Quality Tests 30

4.2.1 Bad Spill Analysis 30

4.2.2 Bad Run Analysis 30

4.2.3 Clean Data Sample 32

4.3 Selection of Exclusively Produced ρ^0-Meson Events 32

4.3.1 The Primary Vertex 32

4.3.2 The Beam Muon μ and the Scattered Muon μ' 33

4.3.3 Exclusivity and Precut Data Sample 34

4.3.4 Semi-Inclusive Deep Inelastic Scattering 35

4.3.5 Outgoing Hadrons 35

4.3.6 ρ^0 - Mesons 36

4.4 Final Data Sample 39

5 Method for Extraction of the Azimuthal Asymmetries **45**

5.1 General Remarks 45

5.1.1 Reasonable Assumption 46

5.1.2 Target Polarization and Dilution Factor 46

5.2 The 2D Fit To Counts Method 47

5.2.1 Motivation 47

5.2.2 General Remarks 48

5.2.3 Poisson Statistic 49

5.2.4 The Levenberg-Marquardt Algorithm 50

5.2.5 Corrections due to Finite Bin Size 51

5.2.6 Obtaining the Physical Asymmetry 52

5.3 Extracting the Physical Asymmetry for the whole Data Sample 53

5.3.1 Data Grouping 53

5.3.2 Calculating the overall Asymmetry 53

6 Results and Discussion **55**

6.1 The Calculated Asymmetries 55

6.2 Compatibility of the Results 58

6.3 Comparison with Theoretical Predictions 59

6.3.1 General Remarks 59

6.3.2 Comparison with Calculations from Goeke et al. 61

6.4 Comparison with Calculations and Measurements from the HERMES Experiment 64

6.5 Comparison with Data measured on a Deuteron Target at COMPASS . 66

6.6 Outlook 67

7 Summary **69**

A Numerical Values for the calculated TTSAs and for the Binning **71**

References **73**

Deutschsprachige Zusammenfassung **77**

List of Figures

2.1 Schematic Picture of the Inclusive Deep Inelastic Scattering Process . . 4

2.2 Handbag Diagram of the DIS Process 5

2.3 Illustration of Momentum, Helicity and Transversity Distribution Function 6

2.4 Schematic Picture of the Semi-Inclusive Deep Inelastic Scattering Process 7

2.5 Handbag Diagram of the Hard Exclusive Meson Production Process . . 8

2.6 Descriptive Interpretation of GPDs 11

2.7 Handbag Diagram of the Deeply Virtual Compton Scattering Process . 13

2.8 Definition of the Azimuthal Angles ϕ_h and ϕ_S 14

3.1 Side View of the COMPASS polarized NH_3-Target 18

3.2 Artistic View of the COMPASS Experiment 19

4.1 Sketch of the Target Container with colored Structures 23

4.2 X-, Y- and Z-Distribution of the Vertex Position of the raw Data . . . 24

4.3 Distribution of the Errors on the X-, Y- and Z-Position of the raw Data 25

4.4 Z- and XY-Distribution of the Vertex Position with a Cut on $\Delta Z_{\text{Vertex}} <$ 0.25 cm and $r > 2.6$ cm 26

4.5 Range of 2 cm around one Filling Hole of the Target Container 27

4.6 Linear Fit for obtaining the XY-Position of the Target with the first Method 28

4.7 Linear Fit for obtaining the XY-Position of the Target with the second Method 29

4.8 Example Plot for the Bad Spill Analysis 31

4.9 Vertex Z- and XY-Distribution 33

4.10 Distribution of the Missing Energy E_{miss} 36

4.11 Distribution of the Transverse Momentum Component p_T^2 37
4.12 Distribution of the Invariant Mass M_ρ 39
4.13 Distribution of the kinematical Variables x_{Bj} and Q^2 41
4.14 Distribution of the kinematical Variables p_T^2 and $-t'$ 42
4.15 Distribution of the kinematical Variables y and W 43

5.1 Illustration of the Target Configuration 45
5.2 Description of the Angular Distributions ϕ_h and ϕ_S in 2D 47
5.3 Illustration of the 8×8 Grid used for the 2D Fit to Counts Method . . . 48

6.1 Results for the TTSAs $A_{UT}^{\sin(\phi_h-\phi_S)}$ for x_{Bj}, Q^2, p_t and y 56
6.2 Results for the TTSAs $A_{UT}^{\sin(\phi_h-\phi_S)}$ for $-t'$, p_T^2, E_{miss} and M_ρ 57
6.3 Compatibility of the Results 58
6.4 Ratio $R = \frac{\sigma_L}{\sigma_T}$ for different kinematical Regions 60
6.5 Definition of the Angle θ 60
6.6 $\cos\theta$-distributions for the five different Q^2 Bins 61
6.7 $\cos\theta$-distributions and kinematical Values for the two additional Bins in Q^2 62
6.8 Comparison of the obtained TTSAs with Theoretical Predictions from Goeke et al. 63
6.9 Comparison of the obtained TTSAs with Theoretical Predictions and Measurements for x_{Bj} obtained at HERMES 64
6.10 Comparison of the obtained TTSAs with Theoretical Predictions and Measurements for $-t'$ obtained at HERMES 65
6.11 Comparison of the obtained TTSAs with Measurements from the HERMES Experiment for Q^2 65
6.12 Comparison of the obtained TTSAs with Results on a Deuteron Target 66

List of Tables

2.1 Quantities used to describe the DIS Process 4

2.2 Quantities used to describe the SIDIS Process 7

2.3 Quantities used to describe the HEMP Process and the DVCS Process 9

3.1 Tracking Detectors used at the COMPASS Experiment 20

4.1 Z-Position of the three Target Cells 26

4.2 Position of the Target Center perpendicular to the Beam Direction . . . 29

4.3 The three sets of Observables monitored for the Bad Spill Analysis . . . 30

4.4 Event Rejection Rates to obtain the Clean Data Sample 32

4.5 Summary of the applied Cuts 38

4.6 Number of ρ^0-Events after applying the Event Selection 40

4.7 Mean Values of the relevant kinematical Variables 40

5.1 Data grouping into Double-Periods 53

A.1 Numerical Values for Binning and TTSAs for x_{Bj}, Q^2 and p_T 71

A.2 Numerical Values for Binning and TTSAs for y, p_T^2, $-t'$, E_{miss} and M_ρ 72

1. Introduction

Since measurements of the anomalous magnetic moment of proton and neutron have revealed the existence of a substructure of the nucleon, a lot of experimental and theoretical research has been performed in order to investigate this substructure in detail. As a result, experiments carried out at the Stanford Linear Accelerator Center (SLAC) in 1970, verified the quark model established by Gell-Mann and Zweig in 1964 [1, 2]. However, the spin structure of the nucleon could not be explained adequately.
A first attempt to describe the nucleon spin by the sum of the spins of its valence quarks failed when the European Muon Collaboration (EMC) at CERN[1] explored in 1983 that the spins of the quarks contribute with only about 30% to the nucleon spin [3]. This so-called "spin crisis" even raised the question of the validity of the quark model. Ever since, many experiments, for example at CERN or DESY[2], have been trying to solve this spin puzzle.
Nowadays, the spin of the nucleon is described by a sum rule based on Quantum Chromodynamics and introduced by Jaffe and Manohar [4]:

$$\frac{1}{2}\hbar = \frac{1}{2}\Delta\Sigma + \Delta G + L_q + L_g, \tag{1.1}$$

with $\Delta\Sigma$ being the contribution of the quark helicity to the nucleon spin, ΔG the contribution of the gluon helicity and finally L_q and L_g the contribution of the orbital angular momentum of the quarks and the gluons respectively. Recent results for $\Delta\Sigma$ obtain about 30% for the contribution of the quark spin and 20 - 30% for the contribution of the gluon spin to the nucleon spin [5], whereas it is still unclear and the subject of present experiments where the rest of the spin comes from.

Introduced in 1994, Generalized Parton Distribution Functions (GPDs) [6, 7] yield new opportunities for solving the spin puzzle. Apart from their huge potential in obtaining a deeper understanding of the nucleon structure, they make the determination of the total angular momentum J^q and J^g, carried by the quarks and gluons, possible. This was first pointed out in a sum rule introduced by Ji [8].
There are two ways to access the Generalized Parton Distribution Functions. One is the Hard Exclusive Meson Production (HEMP) and the other the Deeply Virtual Compton Scattering (DVCS). HEMP will be the topic of this thesis, which will mainly focus on the production of the ρ^0-mesons and is based on data taken in 2007 at the COMPASS experiment (Common Muon and Proton Apparatus for Structure and Spectroscopy)

[1] CERN = Conseil Européen pour la Recherche Nucléaire (European Organization for Nuclear Research)

[2] Deutsches Elektronen-Synchrotron

at CERN in Geneva, Switzerland [9]. At the time of data taking, the experiment was equipped with a proton target, whereas a former thesis on HEMP was performed on data taken in 2002-2004 on a deuteron target [10].

This thesis is structured in seven chapters. In chapter 2 the theoretical concepts will be derived, with a main focus on GPDs and the Hard Exclusive Meson Production channel. Hereby, the Transverse-Target Single-Spin Asymmetry Amplitude $A_{UT}^{\sin(\phi_h-\phi_S)}$, the physical observable extracted in this thesis, will be introduced.
The setup of the spectrometer, used to record the data at the COMPASS experiment in 2007, will then be presented in chapter 3, in which the depth of the descriptions of the several spectrometer parts will be chosen in such a way that they reflect their importance for the analysis.
Chapter 4 will introduce several studies, which are necessary to be performed before starting with the extraction of the asymmetry amplitude. Those are studies performed in order to obtain the exact position of the target in respect to the COMPASS reference system, studies about the data quality to obtain a clean and reliable data sample, and finally the event selection, so that only exclusively produced ρ^0-mesons are selected. Apart from this, the distributions of several kinematical variables of this ρ^0-sample will be presented.
The method used to extract the asymmetry amplitude will be introduced in chapter 5, the so-called "2D Fit to Counts Method".
In chapter 6, the results obtained by the chosen method will be presented and discussed. They will be compared to different theoretical predictions, to results obtained at the HERMES experiment, and to results obtained at a deuteron target at COMPASS.
As a conclusion to this thesis a final summary will be given in chapter 7.

2. Theoretical Motivation

This chapter gives a brief introduction to the theoretical concepts used in this thesis. It is divided into three special cases of Deep Inelastic Scattering (DIS), namely inclusive DIS (sec. 2.1), semi-inclusive DIS (sec. 2.2) and exclusive DIS (sec. 2.3), whereas the latter is the most important for this work. All three DIS processes are introduced with their special kinematical variables and, in some cases, their cross sections. Depending on the several DIS processes, the sections are dealing with Parton Distribution Functions, Fragmentation Functions and Generalized Parton Distribution Functions, as these functions give interesting interpretations to the associated process and continuative understanding about the nucleon.
The exclusive DIS process and its special case, the Hard Exclusive Meson Production with its corresponding Transverse-Target Single-Spin Asymmetry, is described in more detail because of its feasibility to access Generalized Parton Distribution Functions.

2.1 Inclusive Deep Inelastic Scattering

Deep Inelastic Scattering is one of the main tools for investigating the spin structure of the nucleon. This section will treat DIS in the kinematical range covered by the COMPASS experiment, for which the exchange particle can safely be assumed to be a virtual photon. First the basic kinematical variables for the DIS process will be introduced, then the cross-section of this process will be presented and finally Parton Distribution Functions and Structure Functions will be described and a descriptive physical interpretation for these functions will be given.

2.1.1 Kinematical Variables

In the inclusive scattering processes of DIS an incoming lepton $l(k,s)$ scatters off a nucleon $N(P,S)$ via the exchange of a virtual photon $\gamma^*(q,\sigma)$.[1] The outgoing scattered lepton $l'(k',s')$ is detected while the hadronic remnant X of the nucleon remains undetected (see figure 2.1)

$$l(k,s) + N(P,S) \longrightarrow l'(k',s') + X. \tag{2.1}$$

The quantities used to describe such a process are given in table 2.1, where all quantities are Lorentz invariant except for the scattering angle θ.

[1] k, P and q denote the four-momenta, s, S and σ the spin vectors of the correspondent particles.

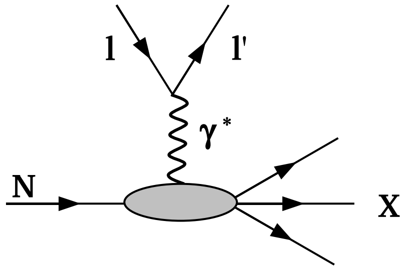

Figure 2.1: Schematic picture of the inclusive Deep Inelastic Scattering process. An incoming lepton l interacts via a virtual photon γ^* with the nucleon N. The outgoing lepton l' is detected, while the hadronic remnant X stays undetected.

Table 2.1: The quantities used to describe a DIS process. M is the nucleon mass at rest, $E(E')$ the energy of the incoming (outgoing) lepton and the laboratory frame is defined by the nucleon at rest.

Scattering angle (lab)	θ	
Virtual photon four-momentum	q	$= k - k'$
Neg. squared virtual photon four-momentum	Q^2	$= -q^2 \overset{lab}{\approx} 4EE' \sin^2\left(\frac{\theta}{2}\right)$
Virtual photon energy	ν	$= \frac{P \cdot q}{M} \overset{lab}{=} E - E'$
Bjorken scaling variable	x_{Bj}	$= \frac{Q^2}{2 \cdot P \cdot q} = \frac{Q^2}{2M\nu}$
Fractional energy loss of the lepton	y	$= \frac{P \cdot q}{P \cdot k} \overset{lab}{=} \frac{\nu}{E}$

2.1.2 Cross Section

The Born cross section in the inclusive DIS process factorizes (for a review see [11]) and can therefore be expressed in terms of the leptonic tensor $L_{\mu\nu}$ and the hadronic tensor $W_{\mu\nu}$:

$$\frac{d^2\sigma}{dQ^2 d\nu} = \frac{4\pi\alpha^2}{Q^4 E^2} L_{\mu\nu} W^{\mu\nu}, \tag{2.2}$$

with the QED coupling constant $\alpha \approx \frac{1}{137}$. While $L_{\mu\nu}$ is directly calculable from QED, $W_{\mu\nu}$ stays unknown and has thus to be parametrized. This can be done in a model-independent way with four dimensionless Structure Functions. For reasons of symmetric requirements (e.g. Lorentz invariance, gauge invariance, symmetry of the strong interaction under charge and parity transformation) the symmetric part of the tensor $W_{\mu\nu}$ can be expressed by the unpolarized Structure Functions $F_1(x_{Bj}, Q^2)$ and $F_2(x_{Bj}, Q^2)$, while the antisymmetric part is parametrized by the polarized Structure Functions $g_1(x_{Bj}, Q^2)$ and $g_2(x_{Bj}, Q^2)$ [12]. The handbag diagram[2] in figure 2.2 illustrates the factorization, in which the hadronic tensor is represented by the blob.

[2] A handbag diagram represents the square of the forward scattering amplitude, which is connected to the cross section via the optical theorem. For more information see for example.

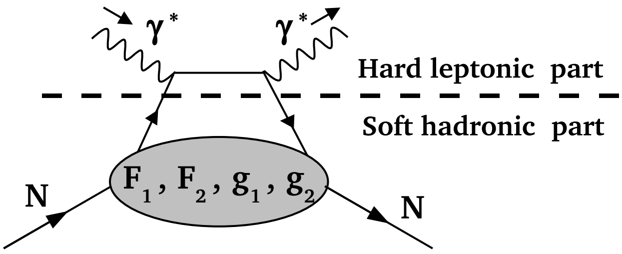

Figure 2.2: DIS process shown as handbag diagram, with factorization into hard and soft processes. The hard leptonic interaction can be treated with perturbative QED, while the soft hadronic part is parameterized with the Structure Functions F_1, F_2, g_1 and g_2, represented by the blob.

2.1.3 Parton Distribution Functions and Structure Functions

In the so-called Quark-Parton-Model (QPM) the nucleon is assumed to consist of point-like particles, the partons [13].[3] Additionally to that, the nucleon is set in the infinite momentum frame, often referred to as the Bjorken scaling limit with $Q^2 \to \infty$, $\nu \to \infty$. This leads to a model in which the partons can be treated as massless non-interacting particles, and DIS can be interpreted as elastic scattering between the incoming particles and the partons. In this model the Structure Functions do not depend on Q^2, an effect known as scaling.

The Structure Functions can be expressed in terms of the Parton Distribution Functions (PDFs) $q_f(x_{Bj})$ and $\Delta q_f(x_{Bj})$ of the different quark flavors f[4]

$$F_1(x_{Bj}) = \frac{1}{2}\sum_f e_f^2 q_f(x_{Bj}), \tag{2.3}$$

$$F_2(x_{Bj}) = x_{Bj}\sum_f e_f^2 q_f(x_{Bj}), \tag{2.4}$$

$$g_1(x_{Bj}) = \frac{1}{2}\sum_f e_f^2 \Delta q_f(x_{Bj}), \tag{2.5}$$

$$g_2(x_{Bj}) = 0, \tag{2.6}$$

where e_f is the charge of the quark with flavor f. The unpolarized PDFs $q_f(x_{Bj})$ are also called momentum distribution functions, the polarized PDFs $\Delta q_f(x_{Bj})$ are sometimes referred to as helicity distribution functions.
The unpolarized Structure Functions F_1 and F_2 are related via the Callan-Gross relation [14]

$$F_2(x_{Bj}) = 2x_{Bj}F_1(x_{Bj}), \tag{2.7}$$

[3] Everything in this section is valid for leading order approximation.
[4] Usually $f = u, \bar{u}, d, \bar{d}, s, \bar{s}$.

a consequence of the experimentally confirmed assumption that quarks carry spin 1/2. In the infinite momentum frame and applying the Quark-Parton-Model, some variables can be interpreted as follows:

- The Bjorken scaling variable x_{Bj} as a fraction of the four-momentum of the nucleon carried by one parton.
- Q^2 as a quantity for spatial resolution.
- Momentum distribution functions as the probability $q_f(x_{Bj})dx_{Bj}$ of finding a quark with flavor f and momentum fraction between x_{Bj} and $(x_{Bj} + dx_{Bj})$.

When taking the interactions between quarks and gluons into account, the Quark-Parton-Model is only an approximation and precise measurements show that the unpolarized Structure Functions become dependent on Q^2. This is called scaling violation.

For the polarized PDFs an interpretation can be given as well: The helicity function in a longitudinally polarized nucleon can be interpreted as the difference in probability between finding a quark with its helicity parallel to the nucleon helicity and a quark with its helicity anti-parallel to the nucleon helicity.
By including transverse spin effects to the approach, one additional PDF has to be introduced, the so-called transversity distribution function $\Delta_T q_f(x_{Bj})$. In the transversity base the transversity distribution function can be interpreted in the same way as the helicity distribution function, but for a transversely polarized nucleon.
An illustration of the three distribution functions is shown in figure 2.3.

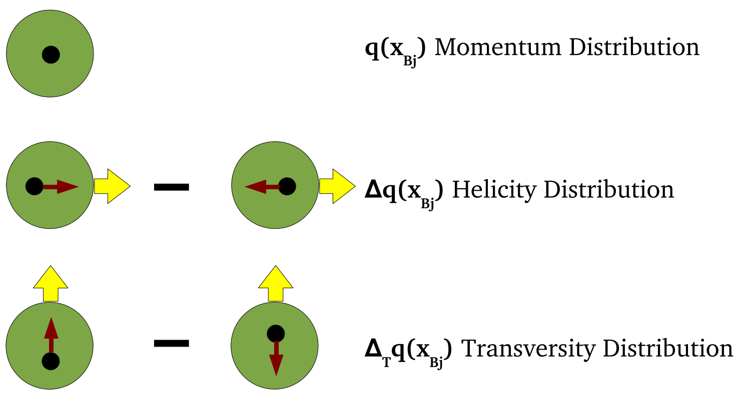

Figure 2.3: Illustration of momentum, helicity and transversity distribution function. The green circles denote the nucleon, the black dots denote quarks. The spin direction for quark and nucleon is indicated by the arrows. The distribution functions have a probabilistic interpretation, e.g. the helicity distribution as the difference in probability between finding a quark with its helicity parallel to the nucleon helicity and a quark with its helicity anti-parallel to the nucleon helicity.

Whereas $\Delta q_f(x_{Bj})$ can be measured in polarized inclusive DIS, $\Delta_T q_f(x_{Bj})$ needs to be measured in semi-inclusive DIS: $\Delta_T q_f(x_{Bj})$ is a chiral-odd object, which is why it has to be combined with another chiral-odd object in order to make the cross section parity even.

2.2 Semi-Inclusive Deep Inelastic Scattering

In semi-inclusive DIS (SIDIS), at least one hadron is detected in addition to the outgoing scattered lepton

$$l(k,s) + N(P,S) \longrightarrow l'(k',s') + h + X. \tag{2.8}$$

A schematic picture of the process is given in figure 2.4.

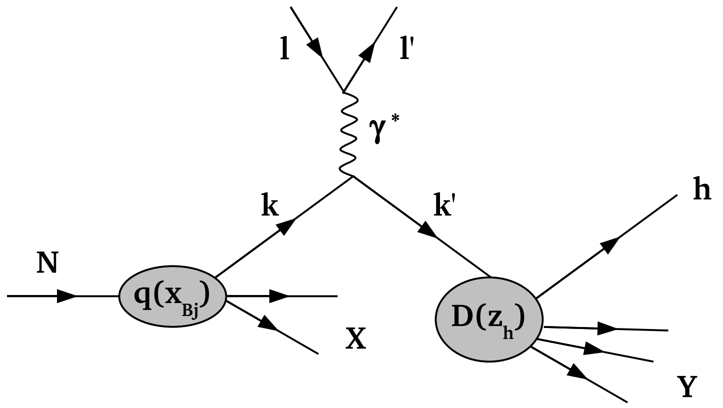

Figure 2.4: Schematic picture of the semi-inclusive Deep Inelastic Scattering process. In addition to the outgoing lepton l' at least one hadron h has to be detected in the final state. The two blobs represent the interactions which cannot be treated perturbatively. The internal structure of the nucleon, described by a Parton Distribution Function $q(x_{Bj})$, is represented by the blob on the left hand side. The fragmentation process, described by a Fragmentation Function $D(z_h)$ is represented by the blob on the right hand side.

In order to describe the SIDIS process, two more variables have to be added to the ones already introduced for the inclusive DIS process in table 2.1. These additional variables are given in table 2.2.

Table 2.2: The additional quantities to describe a SIDIS process with P_h as the four-momentum and E_h as the energy of the detected hadron.

Fraction of the photon energy carried by the hadron	z_h	$= \frac{P \cdot P_h}{P \cdot q} \overset{lab}{=} \frac{E_h}{\nu}$
Transverse momentum of the hadron with respect to the virtual photon	p_T	

The SIDIS process allows the measurement not only of the PDF $\Delta q(x_{Bj})$ but also of the transverse momentum dependent PDF $\Delta_T q(x_{Bj})$.[5] The scattering process and the fragmentation into hadrons are independent from each other [15], depicted in figure 2.4. In this figure, the two blobs represent the interactions not to be treated perturbatively: the internal structure of the nucleon described by the PDFs introduced in section 2.1.3 and the fragmentation process parameterized with a Fragmentation Function (FF) $D(z_h)$. Fragmentation Functions can be interpreted as the probability for a quark with flavor q to fragment into a hadron h with the energy fraction z_h.
As Fragmentation Functions and SIDIS do not contribute to the results of this thesis, they will not be discussed any further and were just mentioned for reasons of completeness, as they play an important role in the COMPASS physics program[6].

2.3 Exclusive Deep Inelastic Scattering

For an exclusive process all n products in the final state have to be detected

$$l(k,s) + N(P,S) \longrightarrow l'(k',s') + \sum_{i=1}^{n} h_i. \tag{2.9}$$

This section will cover two special cases of exclusive DIS, because they are the only two channels appropriate to measure Generalized Parton Distribution Functions (GPDs): Hard Exclusive Meson Production (HEMP) and Deeply Virtual Compton Scattering (DVCS). A handbag diagram of the HEMP channel can be found in figure 2.5 and the additional kinematical variables required for the description of HEMP and DVCS are given in table 2.3.

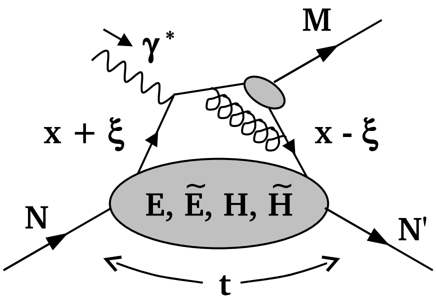

Figure 2.5: Handbag diagram of the Hard Exclusive Meson Production process. The two blobs represent a priori unknown functions. The lower one represents the Generalized Parton Distribution Functions E, $\tilde{E}$, H and $\tilde{H}$, while the upper blob represents a meson distribution amplitude. The initial parton carries the longitudinal momentum fraction $x+\xi$ when interacting with the incoming virtual photon. It is then fragmenting into a meson, described by the meson distribution amplitude, before returning to the nucleon with a longitudinal momentum fraction of $x - \xi$. The variables are defined in table 2.3.

[5] In the following, the flavor indices f will be omitted, q_f will be replaced by the variable q which will represent quarks in general as well as quark flavors. The index g will represent gluons.

[6] More information about the COMPASS physics program can be found for example in [9, 16, 17].

Table 2.3: Quantities used to describe the HEMP Process and the DVCS Process

Average longitudinal momentum fraction of the active quarks in the loop	x
Momentum transfer	$\Delta = P' - P$
Longitudinal momentum fraction of Δ (only valid in the Bjorken limit)	$\xi = \frac{x_{Bj}}{2-x_{Bj}}$
Momentum transfer between the initial and final nucleons	$t = \Delta^2$

This section will first describe the framework of GPDs in detail together with a descriptive physical interpretation. Afterwards, the HEMP channel used in this thesis will be presented followed by a description of its observable, the Transverse-Target Single-Spin Asymmetry Amplitude (TTSA). Additionally, the DVCS channel will be discussed briefly.
The foundations of this section are the reviews and works about GPDs from [18, 19, 20].

2.3.1 Generalized Parton Distribution Functions

Generalized Parton Distributions (GPDs) can be understood as a generalized combination of form factors, parton densities and distribution amplitudes, to which GPDs transit in their limiting case. They thus hold a huge potential and are very interesting to study. Their connection to the nucleon structure was first introduced in the works of Mueller [6], Radyushkin [7] and Ji [8]. Ways to extract GPDs are the HEMP channel and the DVCS channel.
The handbag diagram for the HEMP process is given in figure 2.5, where the lower blob represents four a priori unknown functions, namely the GPDs H, $\tilde{H}$, E and $\tilde{E}$. They all conserve quark helicity and depend upon the three kinematical variables x, ξ and t as defined in table 2.3. GPDs are defined for each quark flavor as well as for gluons, distinguished by a superscripted q and g respectively.
The longitudinally polarized vector-meson channel, which includes the ρ^0-meson channel treated in this work, is only sensitive to the GPDs H and E, while pseudo-scalar meson channels would be sensitive to the GPDs $\tilde{H}$ and $\tilde{E}$. In the ρ^0-meson channel, quark and gluon GPDs enter in the same order of magnitude. Hence this channel appears as one of the rare cases where gluon GPDs may be accessed [21].

Next, a descriptive interpretation of GPDs will be deduced by pointing out the relation between GPDs and form factors or PDFs respectively. Additionally, a way to access the total angular momentum of quarks and gluons in the nucleon through GPDs will be treated.

First Moments

When calculating the first moments of the GPDs it appears that they are related to the form factors known from elastic scattering at the nucleon [22]. By taking a quark of flavor q and any fixed value of ξ, the first moments are given as follows [23]:

$$\int_{-1}^{+1} dx\, H^q(x, \xi = const, t) = F_1^q(t) \qquad \text{Dirac Form Factor} \tag{2.10}$$

$$\int_{-1}^{+1} dx\, E^q(x, \xi = const, t) = F_2^q(t) \qquad \text{Pauli Form Factor} \tag{2.11}$$

$$\int_{-1}^{+1} dx\, \tilde{H}^q(x, \xi = const, t) = g_A^q(t) \qquad \text{Axial Form Factor} \tag{2.12}$$

$$\int_{-1}^{+1} dx\, \tilde{E}^q(x, \xi = const, t) = h_A^q(t) \qquad \text{Pseudo-Scalar Form Factor} \tag{2.13}$$

Therefore GPDs contain information about elastic form factors.

Forward Limit

In the limiting case of $\xi = 0$ and $t = 0$, the so-called forward limit, GPDs turn into the Parton Distribution Functions known from DIS:

$$H^q(x, 0, 0) = q(x) \qquad \text{Momentum Distribution} \tag{2.14}$$

$$\tilde{H}^q(x, 0, 0) = \Delta q(x) \qquad \text{Helicity Distribution} \tag{2.15}$$

The same holds for gluon distributions in the forward limit. For $x < 0$ the equations are valid for anti-quarks. Hence, it is evident in the forward limit, that H and $\tilde{H}$ are generalizations of the PDFs.[7] They conserve the helicity of the proton, which, in contrast, E and $\tilde{E}$ do not. Here the proton helicity can be flipped and thus overall helicity is not conserved, as the massless quarks keep their helicity. Therefore, orbital angular momentum must be transfered because the total angular momentum conservation holds. This is only possible for a nonzero transverse momentum transfer, which does not exist within the model of ordinary parton distributions. Thus E and $\tilde{E}$ do not have any counterparts in this model in the forward limit.

Descriptive Interpretation of GPDs

When combining the information obtained from the first moments about elastic form factors as well as from the forward limit about PDFs, GPDs can be interpreted as a three dimensional picture of the nucleon structure [20]. Elastic form factors are Fourier transformations of the charge distribution of the nucleon in position space, so they contain two-dimensional information. PDFs, however, contain one-dimensional information about the momentum distribution. GPDs are thus a combination of these pieces of information and provide a three-dimensional picture of the nucleon, as depicted in figure 2.6.

[7] There are also distribution functions similar to GPDs called generalized transversity, which give the transversity distribution in the forward limit.

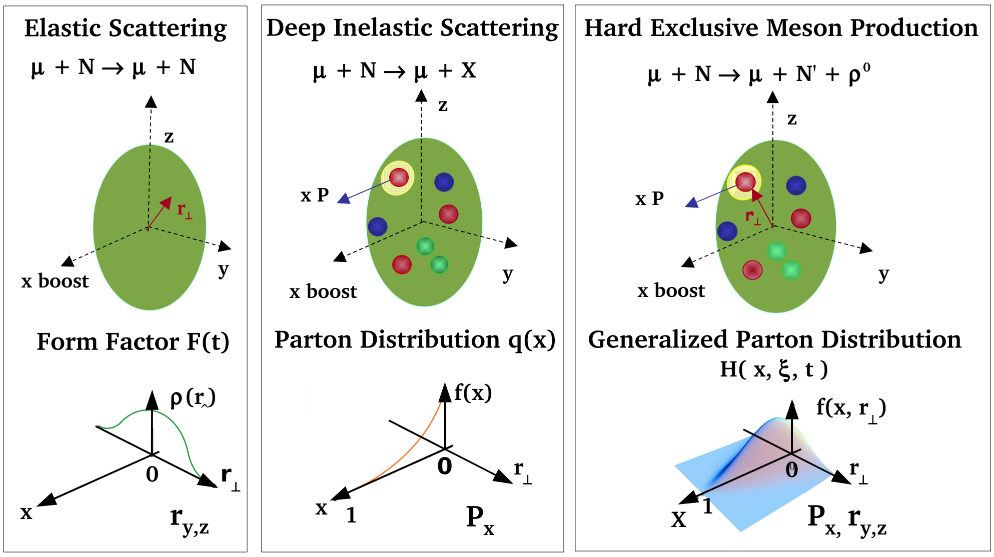

Figure 2.6: Descriptive Interpretation of GPDs. GPDs can be interpreted as a three dimensional picture of the nucleon structure. They contain information about elastic form factors (providing 2D information about the charge distribution of the nucleon in position space) as well as information about Parton Distribution Functions (providing 1D information in momentum space).

Sum Rule

Another very interesting point of GPDs is the fact that they are related to the total angular momentum J^q of quarks in the nucleon and to the total angular momentum J^g of gluons in the nucleon, as first pointed out by Ji in [8]. Ji's sum rule states that the total angular momentum carried by the quarks at $t = 0$ can be accessed by measuring the second moment of the sum of the GPDs H and E:

$$\frac{1}{2}\sum_q \int_{-1}^{+1} dx\, x\,(H^q(x,\xi,0) + E^q(x,\xi,0)) = J^q. \tag{2.16}$$

An equivalent sum rule exists for gluons. As $J^{q,g}$ are part of the spin-puzzle[8], Ji's sum-rule shows once again the importance of studying GPDs. Theoretical models showing how to calculate the total angular momentum for the up- and down-quarks (J^u and J^d) from GPDs can be found in [18, 21]. These models will be used in the discussion of the results.

2.3.2 Hard Exclusive Meson Production

The channel used in this thesis to access GPDs is the Hard Exclusive Meson Production (HEMP) as depicted in figure 2.5, in which only one meson (e.g. $\pi^{0,+,-}$, η, …, $\rho^{0,+,-}$, ω,

[8]Given already in equation 1.1 the spin puzzle can also be expressed in terms of the total angular momenta: $\frac{1}{2}\hbar = \left(\frac{1}{2}\Delta\Sigma + L_q\right) + (\Delta G + L_g) = J^q + J^g$.

ϕ, ...) is detected in the final state. As the ρ^0-meson decays into two charged particles (π^+, π^-) its invariant mass gives a clear resonance signal. From all the measurable mesons, the cross-section of the ρ^0-meson is the largest. Therefore, it provides the largest counting rates and is thus chosen to perform the analysis:

$$l(k,s) + N(P,S) \longrightarrow l'(k',s') + N'(P',S') + \rho^0. \tag{2.17}$$

The handbag diagram for this process is given in figure 2.5, where the lower blob represents GPDs and the outgoing meson M is in case of the present analysis a ρ^0-vector-meson.

In the parton picture this diagram can be interpreted as follows: The initial parton carries the longitudinal momentum fraction $x+\xi$ while the returning one carries $x-\xi$. So there are two different states of the nucleon and the GPDs can be understood as the interconnection in between and thus correlate different parton configurations in the nucleon at a level of quantum mechanics.

But there is another non-perturbative quantity involved in this process: After hard scattering with the virtual photon the initial quark emits a gluon. This gluon disintegrates into a quark-antiquark pair, of which the quark falls back into the nucleon and the antiquark recombines with the initial quark to form the meson. This recombination to the meson is represented by the upper blob in figure 2.5: the meson distribution amplitude.

As the GPD formalism relies on factorization into soft and hard sub-processes, the meson distribution amplitude leads to the additional constraint that the virtual photon has to be longitudinally polarized, otherwise factorization does not hold [24].

Assuming that the concept of s-channel helicity conservation (SCHC) is valid, indicated by experimental data obtained at NMC [25], E665 [26], ZEUS [27], H1 [28] and COMPASS [29, 30], the meson approximately conserves the helicity of the photon and thus is longitudinally polarized. The ρ^0-meson has a very short lifetime, it decays after $4.4 \cdot 10^{-24}$ s to almost 100% into [31]:

$$\rho^0 \longrightarrow \pi^+\pi^-. \tag{2.18}$$

The angular distribution of this decay contains information about the helicity of the vector-meson. Therefore, a measurement of the cross-section for transversely and longitudinally polarized mesons can be translated into cross-sections of transversely and longitudinally polarized photons, from which information about GPDs can be deduced.

The cross section of meson production involving a longitudinally polarized virtual photon $(\gamma_L^* + p \rightarrow M + p)$ is given by

$$\frac{d\sigma_L}{dt} \propto \frac{1}{2} \sum_{h_N} \sum_{h_N'} \left| \mathcal{M}^L \left(\lambda_M = 0, h_N'; h_N \right) \right|^2, \tag{2.19}$$

with the amplitude $\mathcal{M}^L$ for the production of a meson with helicity $\lambda_M = 0$ by a longitudinally polarized photon and the initial and final nucleon helicities h_N and h_N' [18].

According to the discussion lead above, factorization only holds for longitudinally polarized virtual photons, thus a GPD interpretation involving transversely polarized virtual photons can not be given.

2.3.3 Deeply Virtual Compton Scattering

Apart from HEMP there is one more channel to access GPDs, the so-called Deeply Virtual Compton Scattering (DVCS). As this channel is not used in this thesis it will be introduced only briefly, more information about DVCS can be found in [18].

DVCS is measured in exclusive production of real photons

$$l(k, s) + N(P, S) \longrightarrow l'(k', s') + N'(P', S') + \gamma. \tag{2.20}$$

The difficulty in this process is that a single photon and the recoiled nucleon have to be measured. A schema of the DVCS process is shown in figure 2.7.

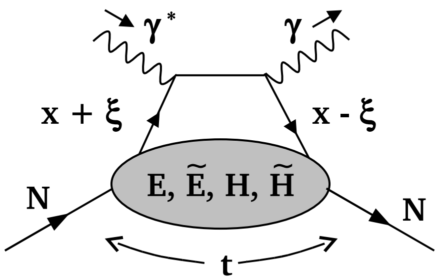

Figure 2.7: Handbag diagram of the Deeply Virtual Compton Scattering process. The lower blob represents the GPDs E, $\tilde{E}$, H and $\tilde{H}$. The initial parton interacts with the incoming virtual photon, then it is emitting a real photon and finally it is going back to the nucleon.

Another problem arises from the fact that the Bethe-Heitler process (BH) contributes to the same final state. In the Bethe-Heitler process a real photon is emitted by the incoming or outgoing lepton. Information about GPDs is contained in the amplitude of the DVCS process as well as in the interference of Bethe-Heitler and DVCS. Depending on the kinematical region this information can be accessed by one or the other process.

DVCS is part of the future physics program of COMPASS. The program contains a Recoil Proton Detector to detect the final state proton, in which read-out electronics from the Freiburg group is included. Additional information about the DVCS-program of COMPASS can be found in [32] and more information about the Recoil Proton Detector in [33].

2.3.4 Transverse-Target Single-Spin Asymmetry

Besides the cross section σ_L given in formula 2.19, there is a second observable which involves only longitudinal amplitudes, the Transverse-Target Single-Spin Asymmetry[9] $A_{UT}(\phi_h - \phi_S)$ [18]:

$$A_{UT}(\phi_h - \phi_S) = \frac{d\sigma^+(\phi_h - \phi_S) - d\sigma^-(\phi_h - \phi_S)}{d\sigma^+(\phi_h - \phi_S) + d\sigma^-(\phi_h - \phi_S)}$$

$$= \frac{d\sigma(\phi_h - \phi_S) - d\sigma(\phi_h - \phi_S + \pi)}{d\sigma(\phi_h - \phi_S) + d\sigma(\phi_h - \phi_S + \pi)} \tag{2.21}$$

The index UT at the asymmetry indicates that it is measured with an unpolarized (U) beam on a transversely (T) polarized target. ϕ_h is the angle between the muon scattering plane and the meson production plane, and ϕ_S is the angle between the muon scattering plane and the target spin vector, both defined in the γN-system (GNS) as shown in figure 2.8. The cross section $d\sigma^+$ represents one configuration of the target spin polarization, while $d\sigma^-$ represents the second one with the target spin flipped.

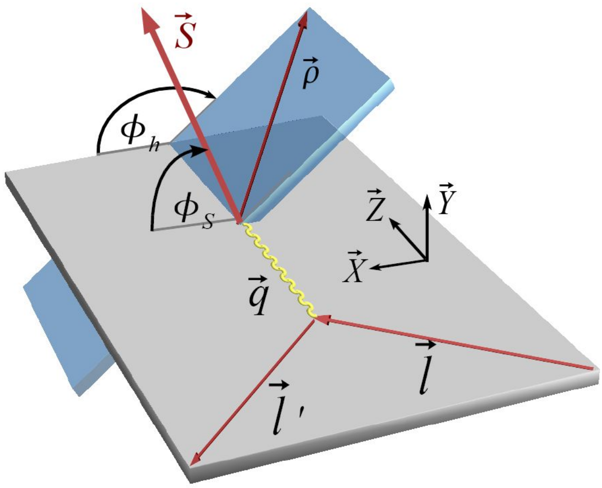

Figure 2.8: Definition of the azimuthal angles ϕ_h and ϕ_S. In the γN-system the incoming and the outgoing lepton define the lepton scattering plane; the virtual photon vector and the outgoing ρ^0-meson define the meson production plane. ϕ_h is defined as the azimuthal angle between the scattering plane and the meson production plane. ϕ_S is defined as the azimuthal angle between the scattering plane and the direction of the spin vector $\vec{S}$.
The Z-axis is defined as the direction of the virtual photon vector, the X-axis is defined perpendicular to the Z-axis and in the lepton scattering plane, and finally the Y-axis is defined in such a way that a right-handed coordinate system is obtained.

[9]The asymmetry is called Transverse-Target Single Spin Asymmetry, because it is defined for a transversely polarized target and an unpolarized beam (single spin).

An asymmetry regarding the target spin configuration is used, since the cross section changes if the target spin is flipped, as it is proportional to the target polarization. All the other parts of the cross section which do not depend on the target spin cancel themselves out, which makes the asymmetry an observable only sensitive to the target spin.
In the next step the azimuthal asymmetry $A_{UT}(\phi_h - \phi_S)$ is now expressed in terms of its amplitude $A_{UT}^{\sin(\phi_h-\phi_S)}$, shorten as TTSA (Transverse-Target Single-Spin Asymmetry Amplitude):

$$A_{UT}(\phi_h - \phi_S) = A_{UT}^{\sin(\phi_h-\phi_S)} \cdot \sin(\phi_h - \phi_S). \tag{2.22}$$

Goeke et al. show in [18] that the TTSA for longitudinal ρ^0-meson production is proportional to the imaginary part of the interference of two amplitudes A and B:

$$A_{UT}^{\sin(\phi_h-\phi_S)} \propto Im(AB^*), \tag{2.23}$$

where A and B for this process[10] are given by [34, 35]:

$$A_{\rho^0_L p} = \int_{-1}^{1} dx \frac{1}{\sqrt{2}} \left(e_u H^u - e_d H^d\right) \left\{ \frac{1}{x-\xi+i\epsilon} + \frac{1}{x+\xi-i\epsilon} \right\}, \tag{2.24}$$

$$B_{\rho^0_L p} = \int_{-1}^{1} dx \frac{1}{\sqrt{2}} \left(e_u E^u - e_d E^d\right) \left\{ \frac{1}{x-\xi+i\epsilon} + \frac{1}{x+\xi-i\epsilon} \right\}, \tag{2.25}$$

where $e_u = +\frac{2}{3}$ and $e_d = -\frac{1}{3}$ are the electrical quark charges of the up and down quarks. These amplitudes contain the GPDs H and E respectively and therefore the TTSA itself depends linearly on them. Thus, extracting the TTSA gives the opportunity to access the GPDs E and H, which are part of Ji's sum rule and can be used to calculate the total momentum contributions J^u and J^d of the up and down quarks to the nucleon spin.

The aim of this thesis will be the extraction of the Transverse-Target Single-Spin Asymmetry amplitude from data taken from a polarized proton target in the year 2007 at the COMPASS experiment. In the following chapter, the COMPASS experiment and its polarized proton target will be described in detail.

[10] Similar formulas exist for the other vector-meson channels.

3. The COMPASS Experiment

This chapter will be dedicated to the description of the fixed target experiment COMPASS, which is located at the M2 beam line of the SPS[1] at CERN in Geneva, Switzerland. Its main goal is to investigate the spin structure of the nucleon, for which a 160 GeV naturally polarized μ^+-beam (sec. 3.1) and a polarized NH_3 target (sec. 3.2) were used during the data taking period relevant to this thesis. Due to the fact that the data analyzed in this thesis was taken in 2007, the spectrometer setup used during this data taking period will be presented (sec. 3.3). Herby, the contents of the sections are chosen in such a way that they reflect the sections' importance for the analysis. Briefly, the data reconstruction process at COMPASS will be introduced (sec. 3.4). More detailed information can mainly be found in [36].

3.1 The Beam

The muon beam is derived from an intense primary proton beam of 400 GeV/c impinging on a Beryllium target. Pions and kaons produced at this target are transported in the M2 beam line [37], by several quadrupoles and dipoles. Along their way, a fraction of the pions and kaons decays into one muon and one neutrino each. The muons get focused and the remaining hadrons are stopped by a hadron absorber. Arriving at the experimental hall, the muons are focused on the polarized target. However, it is not possible that all muons are focused on the target, which is why the beam is accompanied by a large halo.
The muons of the nominal beam have a momentum of about 160 GeV/c with a flux of $2 \cdot 10^8$ muons per SPS cycle and are naturally polarized due to the parity violation of the pion decay. One cycle has a length of 4.8 s, which is called a spill, followed by a break of 12 s. A maximum of 201 spills is collected in a so-called run. Since the muons have a large momentum spread of about 5%, a measurement of the momentum of each muon is required. This is done by the Beam Momentum Station (BMS), which is consisting of several hodoscope planes located in front of the spectrometer.
The halo of the beam has a large diameter with about 16% of the muon beam in an area within 3 - 15 cm of the beam axis, and about 7% of the muon beam even further away.

3.2 The Polarized Target

Among other spectrometer upgrades, a new target-magnet was installed at COMPASS in 2006. In 2007, the ^{6}LiD-target was replaced by a new target with larger diameter.

[1] SPS = Super Proton Synchrotron

The new solid state target consists of irradiated ammonia (NH_3) and is used as a proton target. It is divided into three cells with the central cell being twice as long as the outer cells. The outer cells are 30 cm, the central cell is 60 cm long, while all cells have a diameter of 4 cm. During operation, the outer cells are always polarized in the same direction and, at the same time, in opposite direction to the inner one. As the cells are getting polarized via dynamic nuclear polarization [38], which is obtained by irradiating the paramagnetic centers with microwaves, a gap of 5 cm filled with microwave stoppers is needed between the cells. The polarization is switched once per week, and the data collected in one week is labeled as a period. This configuration reduces false asymmetries arising from variations of the spectrometer acceptance for reaction products originating from the different cells. Figure 3.1 shows a sketch of the NH_3-target.[2]

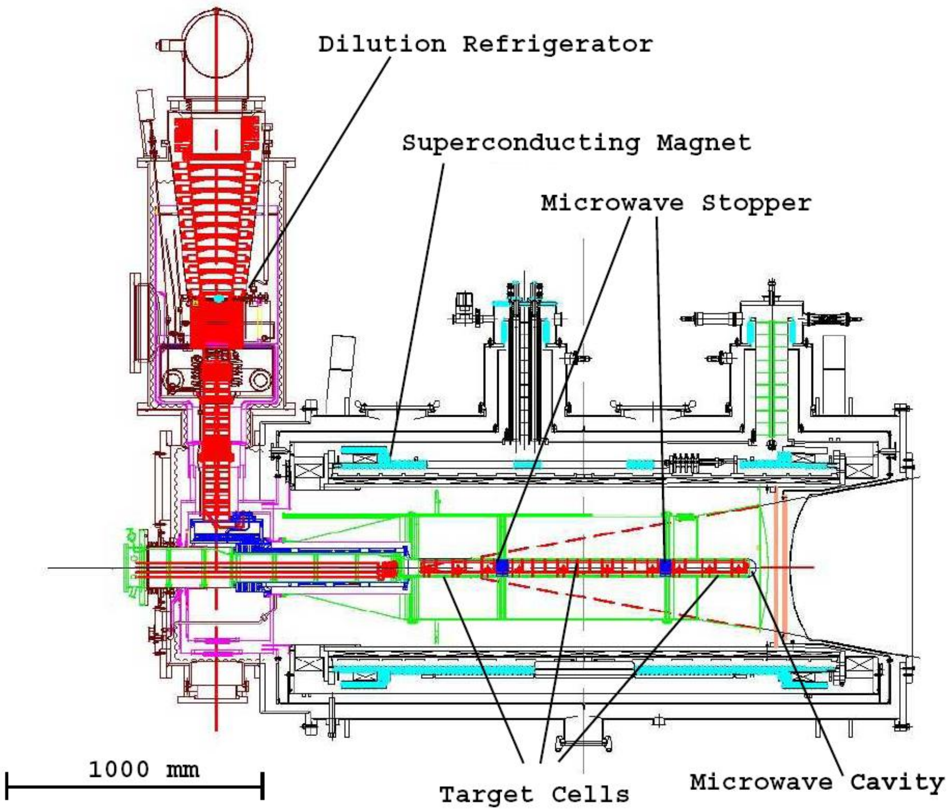

Figure 3.1: Side view of the COMPASS polarized NH_3-target: The dilution refrigerator can cool the target down below 90mK in order to maintain the target in the frozen spin mode. The superconducting magnet produces a 2.5 T holding magnetic field along the beam direction and a 0.5 T holding field perpendicular to the beam axis. The three target cells are separated by microwave stoppers, and the target material in these cells can be polarized in individual directions via the microwave cavity. Picture taken from [39].

[2]Additional information about the COMPASS polarized target can be found in section 4.1.

3.3 The COMPASS Spectrometer

The COMPASS spectrometer [36] consists of two stages in order to allow a large range of momentum and angle measurement: The Large Angle Spectrometer (LAS) and the Small Angle Spectrometer (SAS). Two spectrometer magnets (SM1 and SM2) are used: SM1 for the LAS, SM1 and SM2 for the SAS. Different types of detectors are included in the setup and will be briefly described in this section: Tracking detectors, a Ring Imaging Cherenkov Counter (RICH), muon filters and hadron as well as electromagnetic calorimeters. Furthermore, the trigger system and the front end electronics will be mentioned.
A schematic view is given in figure 3.2.

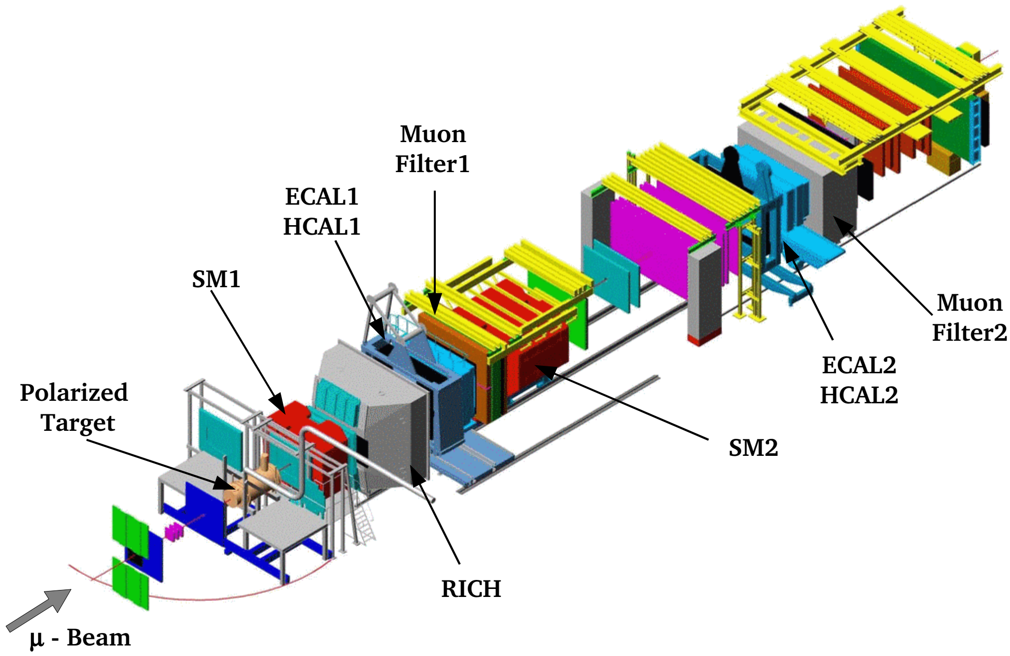

Figure 3.2: Artistic view of the COMPASS experiment in 2007 [36]: The muon beam enters from the bottom left side and is detected by scintillating fibres and silicon detectors before entering the polarized target. In the two stages of the spectrometer, the remnants of the reactions are detected. Particles with large scattering angles are detected in the first stage, which consists of a spectrometer magnet (SM1), different tracking detectors (see table 3.1), calorimeters (HCAL, ECAL) and particle identification detectors (RICH, muon filter). Small angle scattered particles are detected by the second stage, which consists of both spectrometer magnets (SM1 and SM2) and, except for the RICH, similar detectors as in the first stage.

3.3.1 Tracking Detectors

Included in the setup are several tracking detectors, customized to the particle flux in different parts of the detector and to the required spatial resolution. They are used to determine the momenta of charged particles and can be classified into three groups, namely Very Small Area Trackers (VSAT), Small Area Trackers (SAT) and Large Area Trackers (LAT), whereby a typical tracking station consists of one tracker from each group. Table 3.1 lists the tracking detectors used in the spectrometer.

Table 3.1: The three groups of tracking detectors used at the COMPASS experiment.

Group	Used Detector Types
VSAT	Scintillating Fibres, Silicon Micro Strips
SAT	Micromesh Gaseous Structure (MICROMEGAS),
	Gas Electron Multiplier (GEM)
LAT	Drift Champers (DC), Straw Tubes,
	Multi Wire Proportional Chambers (MWPC)

3.3.2 Particle Identification

The particle identification is carried out in two steps. First, the particles are divided into muons and hadrons, using the muon filters and the calorimeters. Second, the particle identification is carried out with the RICH to identify the hadrons. As this analysis does not make use of the RICH, it will not be described here.[3]

Muon Filters

Muon filters take advantage of the fact that muons pass through a much larger amount of material than any other charged particle. Because of this, the muon filters consist of thick iron or concrete walls. Wire chamber detectors in front of and behind these walls detect particles which managed to get through. Only particles having hits in both of this tracking devices, embedding the hadron absorbers, are tagged as muons. In the COMPASS spectrometer, the muon wall detectors are placed at the end of each of the two spectrometer stages.

Calorimetry

At the COMPASS experiment two different kinds of calorimeters are used: Electromagnetic calorimeters (ECAL1 and ECAL2) which are used to determine the energy of electrons and photons and hadronic calorimeters (HCAL1 and HCAL2), which are used to measure the energy of hadrons and distinguish between muons and hadrons, as muons deposit less energy in the HCALs then hadrons. ECALs are homogeneous calorimeters, consisting mainly of lead glass blocks. The HCALs used at the COMPASS experiment are sampling calorimeters, consisting of alternating layers of iron and scintillator plates.

[3] Information about the RICH can be found in [40].

3.3.3 Trigger System and Front End Electronics

Due to the high beam intensity and the high density target the rates of events in the experiment are very high. Therefore, it is necessary that interesting event candidates are pre-selected already on the hardware level. This is done by the trigger system [41], based on fast hodoscope signals, energy deposits in calorimeters and a veto system.
Divided into groups called inner, ladder, middle, inclusive middle and outer trigger, the hodoscopes detect the scattered muon in different kinematical ranges of Q^2 and ν, which is equivalent to the angle under which the muon gets deflected in the spectrometer magnets. Depending on the amount of energy loss, hadron candidates are triggered in the HCALs by the so-called calo trigger. For events triggered only by the calo trigger there is a calo subtrigger consisting of signals from HCAL1, HCAL2 and ECAL1. Finally, the veto hodoscopes in front of the target exclude events originating from the beam halo instead of being a scattered muon candidate.
The data of the triggered events is digitized on front end cards (e.g. [42]) directly on the different detectors, where it is stored until the Data Acquisition System (DAQ) [43] reads out the data and merges it on event builders. From there, the data is copied to the CERN computing center, where it is buffered on disk until it is finally written on tape as so-called raw data.

3.4 Data Reconstruction and Initial Data Sample

After the raw data is obtained and written on tape, several steps have to be performed to bring the data into the format which finally was used in this thesis.
The events are processed by CORAL[4], where track reconstruction, vertex finding and preparation of RICH and calorimeter information take place. Events containing at least one vertex are written in files, which are the basis for further analysis. These files are stored on local terminals and can be processed with the software tool PHAST[5], obtaining either smaller files in the same format for further data processing again with PHAST, or ROOT[6]-Trees containing the desired information to perform the final steps of the analysis using ROOT.

For the present analysis, an initial data sample was produced from the CORAL output files. This initial data sample required the following criteria[7] for every event:

- At least two outgoing tracks from the primary vertex.
- One of this tracks has to be the scattered muon, one a hadron candidate.
- Photon virtuality $Q^2 > 1$ (GeV/c)^2.

In this thesis, PHAST version 7.058 is used on the initial data sample to obtain its results.

[4]CORAL = COMPASS Reconstruction and Analysis Framework [44].
[5]PHAST = Physics Analysis Software Tools [45]
[6]ROOT: An object oriented data analysis framework [46]
[7]In the following, criteria restricting the data will often be referred to as cuts.

4. Target Position, Data Quality and Event Selection

The analysis presented in this thesis is based on data which was recorded during several periods of data taking in 2007 at the COMPASS experiment. Before starting the extraction of the asymmetry amplitude, several checks and studies have to be performed to obtain a reliable data sample on which the final analysis is based. The goal of this chapter is the description of these studies.
First, it will be described how the precise position of the target used in the experiment is determined (sec. 4.1), followed by a brief section covering the data quality aspects (sec. 4.2). Afterwards, the event selection will be covered in detail (sec. 4.3) to obtain the final exclusive ρ^0-meson sample, which will be presented in the final section together with its kinematical distributions (sec. 4.4).

4.1 Target Position

In 2007, the COMPASS experiment used a polarized proton target as described in section 3.2. A target container is used, which contains the target material (see figure 4.1). In the following the term "target" will be used for the target container including the target material.

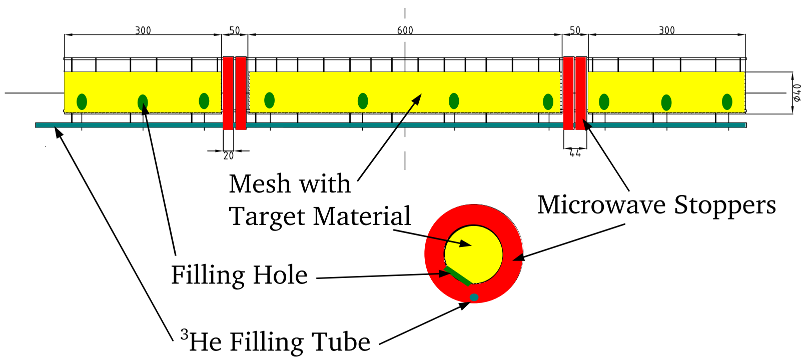

Figure 4.1: A sketch of the target container with colored structures used in this analysis. The mesh in which the target material is located is represented in yellow, the microwave stoppers are represented in red, the filling holes, for filling the target material in the container, are represented in green and the ^{3}He filling tube is represented in light blue. On the upper part the target container is given in the ZX-plane, on the lower part in the XY-plane.

Once the target is installed in the spectrometer and cooled down to its operating temperature of a few millikelvin, there is no way to determine the exact position of the target with respect to the impinging beam. As the target has a finite length, it is essential to determine the precise position to be able to judge if an event occurs in the target material or already outside of it. Therefore, the position of the target in direction of the beam axis (Z-position) is determined (sec. 4.1.2). Before that, some general remarks will be given (sec. 4.1.1). Since the target has a finite diameter in respect to the halo of the beam, it is additionally important to determine the position of the target perpendicular to the beam axis (XY-position) in order to distinguish if the event took place in the target material or already on material surrounding it. This position is determined by two different methods (sec. 4.1.3).
The target position analysis as presented in this section is based on CORAL output files from data taking periods W27, W31, W41, W42 and W43, because statistics from the initial data sample (see sec. 3.4) is not sufficient. For the used set of data, the request for a primary vertex[1] is the only restriction. Detailed information can be found in [47].

4.1.1 General Remarks

The straightforward method to determine the target position would be to look at the distribution of vertices in X-, Y- and Z-direction[2], as presented in figure 4.2. This figure shows a Gaussian distribution in the X- and Y-distribution and a distribution showing the shape of the target in Z-direction. A Gaussian fit would therefore provide

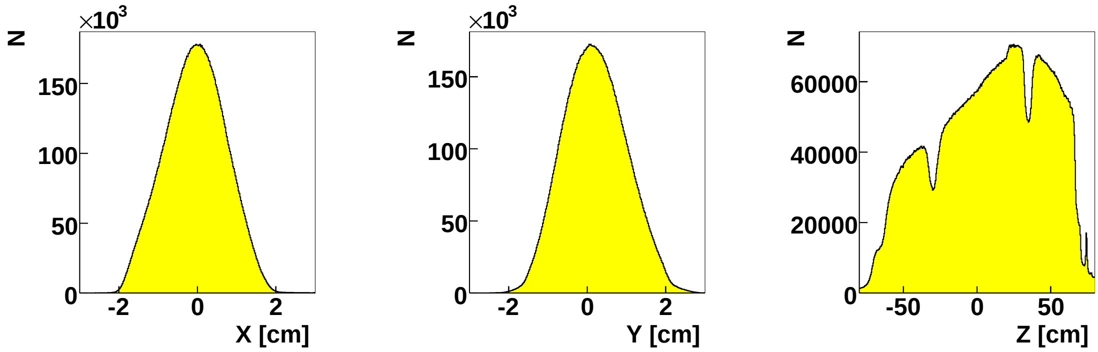

Figure 4.2: X-, Y- and Z-distribution plots of the vertex position of the used data. On the left the X- and in the middle the Y-distribution of the vertex, showing a Gaussian distribution. On the right, the Z-distribution of the vertex showing the three target cells.

the information about the center of the target for the XY-plane. From the shape of the Z-distribution one could estimate the Z-positions of the three target cells.
The problem for this method is that the plots do not show the distribution of the target material itself, they rather represent a convolution of target material distribution and the beam intensity distribution. For the XY-plane this causes a problem when the

[1] The definition of the primary vertex is given in section 4.3.1.
[2] Information about the COMPASS references system is given in figure 2.8.

beam is not centered at the middle of the target, which is not ensured in the present case. A problem would also occur, if the beam intensity did not follow a Gaussian distribution. For the Z-distribution, one can see in figure 4.2, that the borders between the cells are rather fuzzy, and that a precise position determination would be difficult. For this reasons the data is analyzed and browsed through to find structures of the target container itself. These are then used to determine the precise position of the target. The used structures are shown in the sketch in figure 4.1.

4.1.2 Target Position in Z-Direction

In order to determine the position of the target in Z-direction, a cut on the error of the reconstructed vertex Z-position is applied with $\Delta Z_{\mathrm{Vertex}} < 0.25$ cm, to minimize the error on the result. The error is small, if many tracks originate from the vertex, and big in the contrary case. Figure 4.3 shows the distribution of the errors on the X-, Y- and Z-position. The errors on the X- and Y-position are two orders of magnitude smaller than the errors on the Z-position, which is why only a cut on the error of the vertex Z-position needs to be applied.

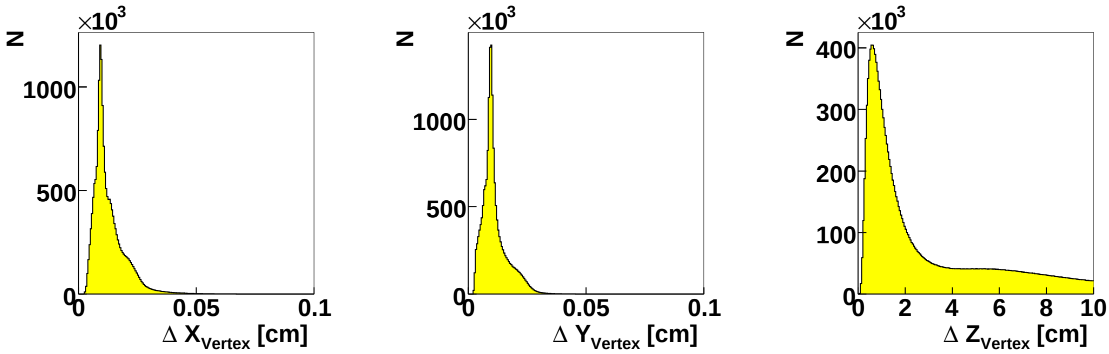

Figure 4.3: Distribution of the errors on the X-, Y- and Z-position of the vertex of the used data. The errors on the X- and Y-position are two orders of magnitudes smaller than the errors on the Z-position.

Furthermore a radial cut with $r > 2.6$ cm is applied on the data. The purpose of this cut is to get rid of the inner part of the target, where the NH_3 target material is located. If the events from the target material itself are not contained in the data anymore, only events which took place at the target container are represented there. In the present case the microwave stoppers become visible because they have a diameter of about 6.9 cm, in contrary to the mesh with the target material which has only a diameter of 4.0 cm. Looking at the vertex distribution after this cut (figure 4.4) the position of the microwave stoppers becomes visible in the Z-distribution and thus the exact position of the target container can be determined, as indicated on the left hand side in figure

4.4.[3] Knowing the exact position of the target container determines the position of the target material as well.

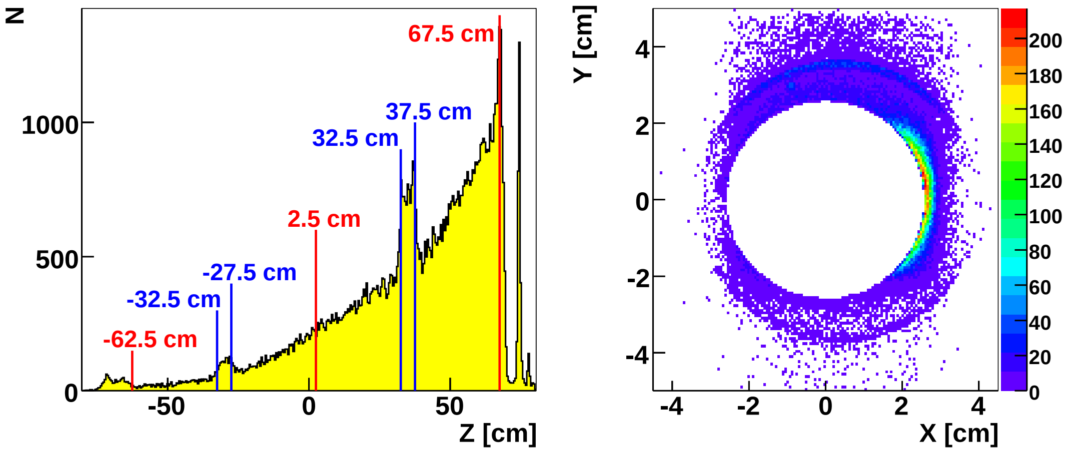

Figure 4.4: Z- and XY-distributions of the vertex position with cuts on $\Delta Z_{\text{Vertex}} < 0.25$ cm and on $r > 2.6$ cm. On the left hand side the Z-distribution with the position of the microwave stoppers indicated in blue, and the beginning, the center and the end position of the target container indicated in red. On the right hand side the XY-plane of the vertex position with the visible cut on $r > 2.6$ cm.

As a summary, the position of the three target cells in the COMPASS reference system is given in table 4.1, the errors are estimated on the basis of the personal bias in reading the values from the plot and the accuracy of the Z-position of the vertex distribution.

Table 4.1: Z-Position of the three target cells.

Cell	Start [cm]	End [cm]
Upstream	-62.5 ± 0.2	-32.5 ± 0.2
Center	-27.5 ± 0.2	32.5 ± 0.2
Downstream	37.5 ± 0.2	67.5 ± 0.2

4.1.3 Target Position in the XY-Plane

The XY-position is determined via two different methods in order to provide two independent results to perform a cross-check. Two cuts are applied on the data: Once again, a cut on the error of the Z-position of the vertex, $\Delta Z_{\text{Vertex}} < 2$ cm, and a radial

[3] The events from the microwave stoppers are not visible in a vertex Z-distribution without a radial cut, because much more events take place in the target material and mask the events from the target container.

cut with $r > 1.5$ cm. The Z-position cut is needed to obtain a small enough error in Z as the Z-position plays a role in this analysis, while the radial cut is only needed to reduce the amount of irrelevant data.
For both of the applied methods a range in Z-direction of 2 cm is placed around each of the ten filling holes as these filling holes are the structures used here. Each of these "2 cm"-samples is analyzed by plotting the spatial XY-distribution and locating special structures of the target container. An example for one of these samples is shown in figure 4.5, where one filling hole, the ^{3}He filling tube, and the mesh of the target cell is visible. These structures are used for the two different methods to obtain the position of the center of the target in the XY-plane.

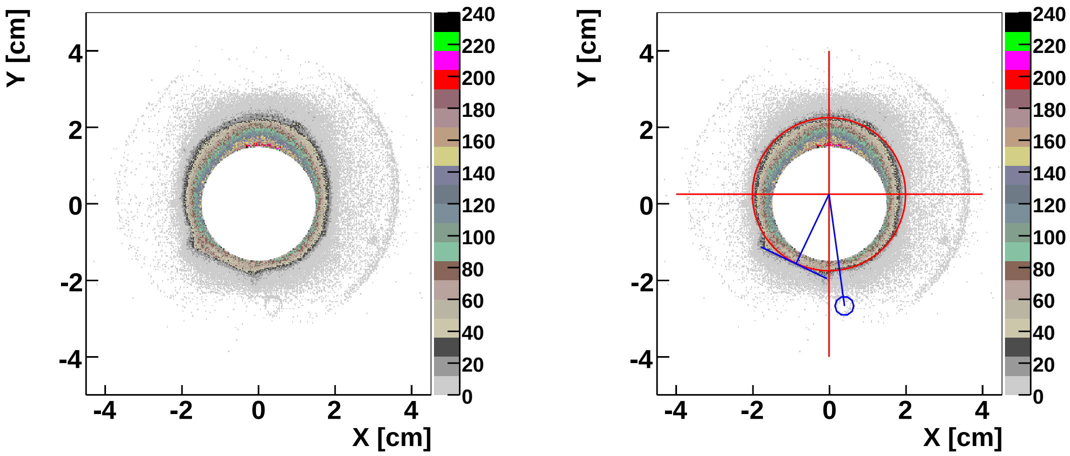

Figure 4.5: Example of a data plot of a 2 cm range around one of the ten filling holes. On the left hand side the XY-plane as provided from the data. On the right hand side the same plot with indicated structures used to determine the XY-position of the target: The mesh of the target container is represented as red circle, the filling hole is represented as blue bar and the ^{3}He filling tube is represented as blue circle.
Both methods used to determine the XY-position are sketched in the figure, the first method is represented in red and the second is represented in blue.

First Method

In the first method, the mesh of the target container is used. A circle with the known radius of 2 cm of the mesh is fitted into the plot and the center of the circle is determined, as indicated in red on the right hand side of figure 4.5. This is done for all of the ten samples. Next, the ZX-distribution and the ZY-distribution of these samples are plotted and a linear fit is applied as shown in figure 4.6. The gradient and the axis intercept given by the fit are taken, to distinguish the position of the target with respect to the Z-position for the X-direction and for the Y-direction respectively. The errors in the plots are obtained by estimating the accuracy with which the center of the circle can be determined, while the Z-values are given by the middle of the used "2 cm"-range.

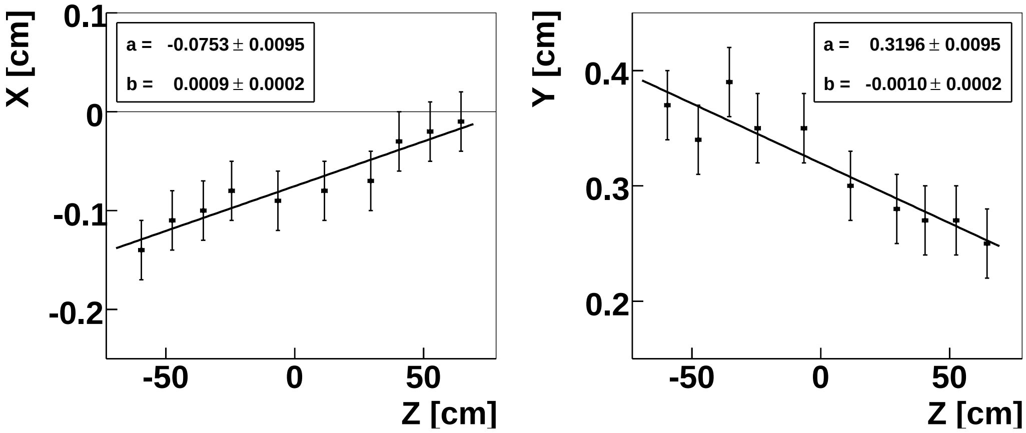

Figure 4.6: Linear fit for obtaining the XY-position of the target with the first method. On the left hand side the ZX-distribution and on the right hand side the ZY-distribution. X and Y values are obtained by specifying the center of the mesh around the target material. The Z value is given by the middle of the used "2 cm"-range for each of the ten filling hole ranges. The gradient b and the axis intercept a given by the fit are used to determine the target position in the XY-plane with respect to the Z-position. The errors are estimated from the accuracy with which the center of the circle can be determined.
When looking at the result of the fit it becomes clear that the errors are overestimated in this case.

Second Method

In the second method, two structures are used: the filling holes for the target material and the ^{3}He filling tube. Here, the position of the center of the ^{3}He filling tube is taken, as well as the touch point of the filling holes on the target material, both in the XY-plane. From these two points, the center of the target is calculated with given distances[4]. This method is indicated in blue on the right hand side of figure 4.5. For the calculated centers a linear fit is performed similar to the fit in method one. The fit is given in figure 4.7, where the error bars are calculated with Gaussian error propagation from the estimated accuracy of the numbers.

Cross-check and Result

In the last step the results of the methods are compared with each other and are found to be compatible.

The final result is obtained by calculating the mean value of the two results and can

[4]Distance center of filling holes to center of target cell: 2.00 cm
Distance center of ^{3}He filling tube to center of target cell: 2.90 cm

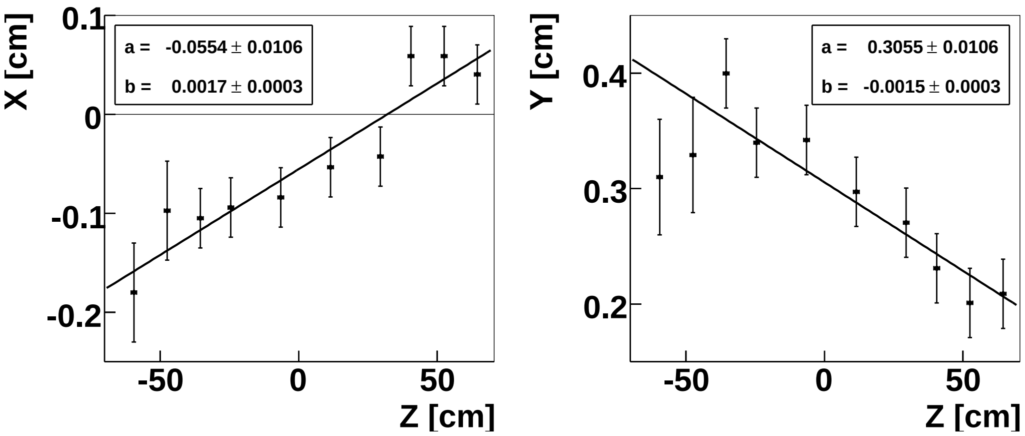

Figure 4.7: Linear fit for obtaining the XY-position of the target with the second method. On the left hand side the ZX-distribution and on the right hand side the ZY-distribution. The X and Y values are calculated from the obtained position where the filling hole touches the mesh and the center of the ^{3}He filling tube. The Z values are given by the middle of the used "2 cm"-range for each of the ten filling hole ranges. The errors are calculated with Gaussian error propagation from the estimated accuracy of the numbers.

be expressed by two formulas to calculate either the X- or the Y-position of the target center depending on the Z-position:

$$X = (-0.007 \pm 0.02)\ \text{cm} + (0.0013 \pm 0.0002) \cdot Z \tag{4.1}$$
$$Y = (0.31 \pm 0.02)\ \text{cm} - (0.0013 \pm 0.0002) \cdot Z \tag{4.2}$$

Therefore, the result for the upstream and the downstream end of the target can be calculated and is given in table 4.2.

Table 4.2: Position of the target center perpendicular to the beam direction.

Target Position	Z-Position [cm]	X-Position [cm]	Y-Position [cm]
Upstream end	-62.5 ± 0.2	-0.15 ± 0.02	0.39 ± 0.02
Downstream end	67.5 ± 0.2	0.02 ± 0.02	0.23 ± 0.02

For reasons of completeness it should be mentioned that, as a final check, it is tested if the target position has been the same during the whole period of data taking and if the target position stays the same for different alignments. Therefore, the data taken in week 27 and week 43 are compared to see if there are any differences in the distributions. This check is performed for the Z- as well as for the XY-position with the result that the target has not moved and that the obtained results are valid for the whole period of data taking and for all alignments.

4.2 Data Quality Tests

To ensure that all data for the analysis is of the equal quality, several stability and data quality checks are performed. They result in a list on which all runs of bad quality are specified (bad run list) and a similar list for all spills not fulfilling the expected stability criteria (bad spill list).
This section will present the methods used to obtain the bad run and the bad spill list and will show how many percent of events are rejected to obtain a data sample with good quality to perform the analysis with. The initial data sample as introduced in section 3.4 is used as starting point. As all the tests will be discussed rather briefly, more information about this topic can be found in [48, 49].

4.2.1 Bad Spill Analysis

To create the bad spill list, a spill by spill check is performed on three different sets of observables as given in table 4.3. Thereby, the procedure is always similar: The values are monitored for one spill and the distribution of the variables per spill are expected to be constant in time. If one of the monitored variables deviates from the mean value of the spills in the same short-time range of several hours, the spill is rejected. A graphical example for this procedure is given in figure 4.8.

Table 4.3: The three sets of observables monitored for the bad spill analysis.

Macro-variables	Number of primary vertices per event
	Number of beam particles per primary vertex
	Number of tracks per primary vertex
Calorimeter variables	Number of charged ECAL1/2 clusters per event
	Number of neutral ECAL1 clusters per event
	Charged ECAL1/2 cluster energy per event
	Neutral ECAL1 cluster energy per event
	Number of charged HCAL1/2 clusters per event
	Charged HCAL1/2 cluster energy per event
Physical trigger variables normalized to beam flux (inclusive/exclusive)	Number of events with middle trigger
	Number of events with ladder trigger
	Number of events with outer trigger
	Number of events with calo trigger
	Number of events with calo sub-trigger
	Number of events with inclusive middle trigger

4.2.2 Bad Run Analysis

The selection of the bad quality runs is performed via two different methods: One using the reconstructed K^0-mesons, as they are a very sensitive quantity for the stability of

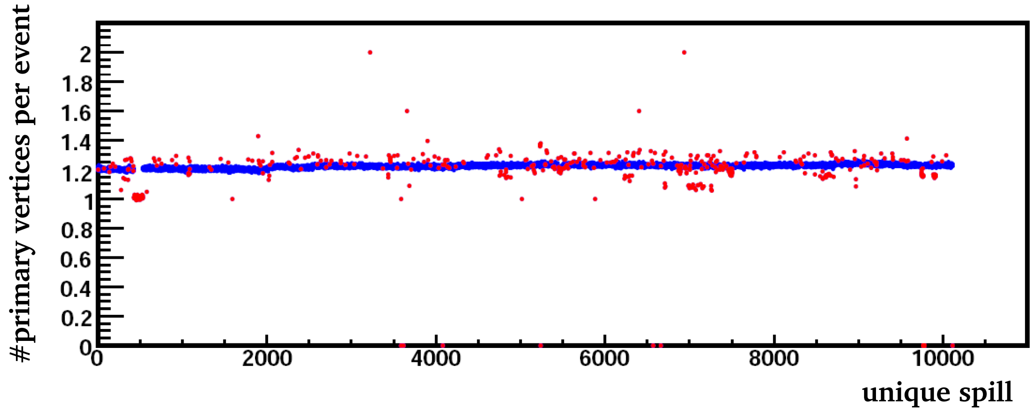

Figure 4.8: An example for the Bad Spill Analysis. Plotted is the number of primary vertices per event against the several unique spills. Marked in red are the spills rejected by the algorithm because this or one of the other observed variables for this spill fluctuate too far away from the mean value.

the spectrometer, and the other one using the stability of physical observables which are used later on in the analysis.

K^0 Stability Checks

For the K^0 stability checks the number of reconstructed kaons per primary vertex is summed up for every run. Afterwards, the distribution of the number of kaons per run is plotted for one period and fitted with a Gaussian distribution. Every run which is outside of a 3σ-range of this distribution is marked as a bad run and excluded from the analysis.

Stability Checks on Observables

The distributions of 14 kinematical variables are monitored and it is checked if they are stable on a run by run comparison. In detail, the variables are binned for each target cell, and then the distributions of the variables from one run are compared with the distributions from every other run from the same period. The same is repeated for all the runs from the corresponding double period partner[5]. The runs are compared with each other by calculating the difference of the normed distributions from the observables, by fitting the difference with zero and thereby obtaining a χ^2 distribution for each run. This χ^2 distribution decides whether the run is good or bad.
The following 14 kinematical variables are observed:

$$x_{Bj},\ p_T,\ y,\ Q^2,\ W,\ P_{\mu'},\ \Theta_{\mu'},\ \phi_{\mu'},\ Z_{\text{prim}},$$

$$\Phi_{\text{Spin,GNS}},\ \Theta_{\text{Hadron,LAB}},\ \Phi_{\text{Hadron,LAB}},\ \Phi_{\text{Hadron,GNS}},\ P_{\text{Hadron}}$$

[5]The calculation of the asymmetry amplitude later on is always performed with two periods with different target polarizations. Such two periods are grouped to one double period.

4.2.3 Clean Data Sample

Starting from the initial data sample introduced in section 3.4, and applying the bad spill as well as the bad run list, event rejection rates as presented in table 4.4 are obtained.

Table 4.4: Event rejection rates to obtain the clean data sample

Week	#Runs	Event Rejection Rate [%]
25	121	33.6
26	94	17.5
39	140	32.4
40	44	27.1
41	99	20.2
42	135	37.9
43	44	17.0

The runs and spills which have not been excluded by these lists are used for the analysis and compose the so-called "clean" data sample. For all the bad runs and spills the reason for the bad quality is analyzed by checking the e-logbook to determine the cause of the lack of quality. However, this will not be discussed any further as this would be beyond the scope of this thesis.

4.3 Selection of Exclusively Produced ρ^0-Meson Events

After performing the stability and data quality checks on the initial data sample, the further procedure is to select the interesting events from the produced clean data sample. In the case of this analysis, interesting events are those with an exclusive ρ^0-particle in the final state. This section will describes how an exclusive ρ^0-data sample is obtained.

4.3.1 The Primary Vertex

The very first restriction is that the event has to be attached to a primary vertex. A vertex is called primary when it is assigned to a beam particle. If more than one primary vertex is reconstructed, the "best" primary vertex is taken: the one with the most outgoing tracks, or with the best reduced χ^2, if two primary vertices have the same amount of outgoing tracks.[6] In addition to the event belonging to a primary vertex, the primary vertex itself must fulfill characteristic requirements. It has to be located inside the target cells; this is why the distance between the vertex position and the target axis has to be smaller than 1.9 cm. To be sure that the vertex is located

[6]The determination of vertex coordinates, as well as of particle tracks, is obtained during reconstruction using a Kalman fit. Therefore the accuracy of these values is given by the reduced χ^2 of the vertex-fit and the particle-track-fit respectively.

inside the target with respect to the Z-axis[7], it has to be positioned in the upstream, the central or the downstream cell, for this purpose the values for the target position obtained by the method described in section 4.1 and presented in [47] are used. Figure 4.9 shows the vertex distribution with respect to the Z-axis and the XY-plane for the primary vertex of the clean data sample. The red lines indicate the applied cuts.

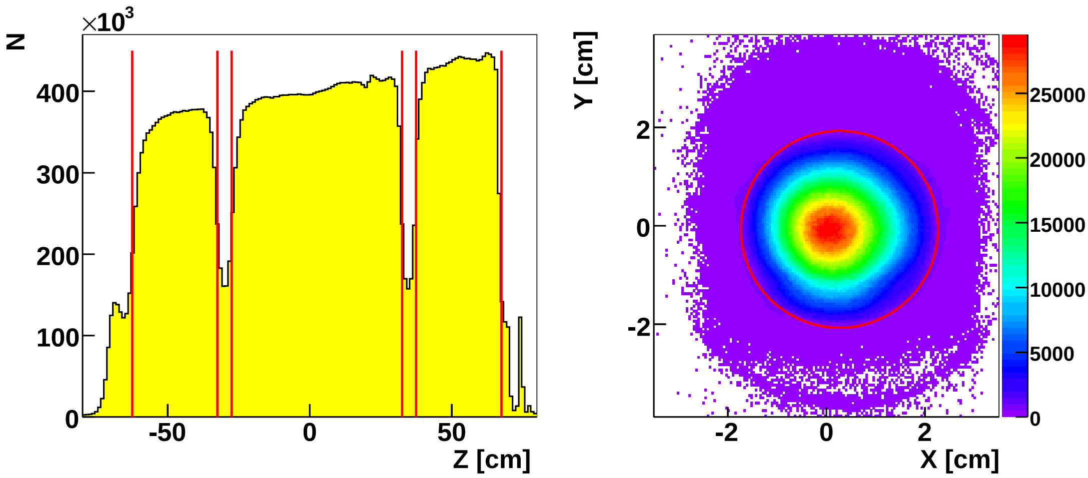

Figure 4.9: Plots of the primary vertex distribution in the COMPASS laboratory system: On the left hand side with respect to the Z-axis, on the right hand side with respect to the XY-plane. The superimposed red lines indicate the applied cuts. The data is taken from the clean data sample.

4.3.2 The Beam Muon μ and the Scattered Muon μ'

As first particles the beam muon μ and the scattered muon μ' are examined in detail to ensure that the tagged μ and especially the tagged μ' are not misidentified and accomplish the claimed quality.

The Beam Muon μ

The beam muon must have a momentum smaller than 200 GeV and a reduced χ^2 of $\chi^2_{red} < 10$, both requirements are needed to guarantee a good quality of the beam particle. Furthermore, the associated track to the beam particle, extrapolated to the most upstream and the most downstream end of the target, has to be inside the target to ensure identical beam intensity in the three different target cells.

The Scattered Muon μ'

A detected particle is tagged as scattered muon μ' when it fulfills the following requirements. Either it is tagged as scattered muon from a CORAL routine during reconstruction, or it is tagged as muon from a recovering process. The recovering process uses

[7]For information about the COMPASS laboratory system see figure 2.8 in section 2.3.4.

hit information of the two Muon Wall detectors MA01 and MA02, where a muon has to have more than three hits in the first and more than five hits in the second Muon Wall to be considered as scattered muon. Additionally, the recovered particle must have positive charge, the associated track must have a measured penetration length[8] of $n = X/X_0 > 30$ and $\chi^2_{red} < 10$. As soon as it fulfills these requirements it is tagged as muon candidate from the recovery algorithm.
Finally, only events containing exactly either one CORAL-tagged muon or one tagged muon candidate from the recovery algorithm, are used for the analysis. If more than one tagged muon and/or candidate are available, the event is discarded.
To be sure that the used scattered muon has the required quality, a check on the penetration length and the reduced χ^2 is performed again, because the CORAL-tagged muon also has to fulfill them.
Another restraint of the scattered muon arises from the fact that there is a problem in the reconstruction of the momentum of the μ' in CORAL. The problem occurs when the μ' is crossing the yoke of the spectrometer magnet SM2, where the magnetic field is not described appropriate. Therefore, events with scattered muons crossing the yoke of SM2 have to be rejected [50].

4.3.3 Exclusivity and Precut Data Sample

The produced ρ^0-meson has one attribute which is of special interest when asking for the demanded exclusive process. It has a very short lifetime of about $4.4 \cdot 10^{-24}$ s, therefore it is not possible to directly detect this meson in the final state. Instead of the ρ^0-meson, the two particles to which the ρ^0-meson decays to almost 100% are detected: the mesons π^+ and π^-. For this reason there are two requirements asked in order to get an exclusive ρ^0-meson in the final state:

- Exactly three outgoing particles, namely the scattered muon and two hadrons as possible decay particles.
- The two outgoing hadrons have to have opposite charge.

These two requests on exclusivity, together with the restrictions on the primary vertex as well as the beam and the scattered muon, reduce the original clean data sample of about a factor of ten, and provide a new precut sample to perform the further event selection. The idea of producing this precut sample is that after selecting only events with probable ρ^0 production, the precut data sample is much smaller than the clean data sample before, and can be handled much easier. One is more flexible and faster when applying further restrictions to the data sample in a second step. The idea at this stage of the event selection is, to apply only restrictions which have to stay in the analysis for sure. In the next step, restrictions which can change during the analysis are applied, for example due to kinematical aspects.
All events fulfilling the required restrictions so far, form the precut data sample.

[8] The penetration length n quantifies the length X of detector material passed by a particle, normalized with the particle-specific radiation length X_0 in this material.

4.3.4 Semi-Inclusive Deep Inelastic Scattering

To select only semi-inclusive DIS events, the following standard kinematical cuts are applied:

- The photon virtuality $Q^2 > 1$ (GeV/c)^2 is required to select DIS events.
- The invariant mass must be $W = (q + P) > 5$ GeV/c^2, to be above the resonance region of the cross section.
- The relative energy transfer y has to be in the range of $0.1 < y < 0.9$, whereas the lower cut eliminates events from the kinematical range of elastic scattering and ensures a good resolution in y, and the upper cut ensures that events, where radiative corrections become important, are discarded.

4.3.5 Outgoing Hadrons

As the ρ^0-meson is detected indirectly via its decay particles π^+ and π^-, there are two outgoing hadrons in the remaining data sample. The cuts applied on them are as follows.
Like the beam and the scattered muon, the hadrons have to fulfill quality criteria as well. Their reduced χ^2 has to be smaller than 10 and their penetration length $n = X/X_0$ smaller than 10. This ensures that the hadrons are well-defined. To reject tracks reconstructed only in the fringe field[9], every particle must have at least one hit behind the spectrometer magnet SM1, which is guaranteed by the requirement on the last measured coordinate $Z_{\text{last}} > 350$cm. As every hadron should belong to the primary vertex, its first measured position has to be in front of SM1, resulting in the cut $Z_{\text{first}} < 350$cm. The position where a hadron can be tracked is defined as $Z_{\text{last}} < 3300$ cm. Behind this position the muon filter MF2 is located and hadrons having hits behind this muon wall have to be rejected because they are misidentified.
Events with hadrons that crossed the yoke of SM2 have to be rejected, as the reconstruction problem mentioned in section 4.3.2, has also to be taken into account here.
As a last cut on the hadrons, one has to check if a hadron is not a misidentified scattered muon. This occurs when the muon goes through the hole close to the beam region in the hadron absorber, and does not, due to this, cross a large amount of material. The muon can then wrongly be identified as a positive hadron while another positive muon coming from the primary vertex is wrongly be assumed to be the scattered muon. To reject these events, the associated tracks of the hadrons are extrapolated to the Z-position of the concrete hadron absorber and it is checked, if the hadron tracks pass through the 40×40 cm^2 hole around the beam region. All events with hadron tracks passing this hole are rejected, with one exception: If the trajectory of the track passes through the active zone of the hodoscope behind the iron absorber located at the very end of the experiment, and no hits are found there, the event is not rejected. In this case it is assumed to be a highly energetic hadron, as it cannot be a muon.

[9]The space between the target and the spectrometer magnet SM1 is called fringe field. Track reconstruction is difficult there, due to the fact that the deflection of the particles is small there, because the effective magnetic field is weak.

4.3.6 ρ^0 - Mesons

After selecting the hadrons from the sample, there are three more cuts needed to identify the ρ^0-mesons in this remaining sample, because it is still contaminated with other particles, for example kaons.
To minimize the non-exclusive background, the amount of energy, which was not detected, is calculated. This so-called missing energy

$$E_{miss} = \frac{M_{P'}^2 - M_P^2}{2 \cdot M_P} = \frac{(P + q - \rho) - M_P^2}{2 \cdot M_P} \tag{4.3}$$

has to be in the range of $|E_{miss}| < 2.5$ GeV. E_{miss} is in principle calculable using the target particle mass M_P subtracted from the invariant mass of the recoiling particle $M_{P'}$, normalized with two times the target particle mass (see formula 4.3). After all, this calculation is not feasible because the recoil particle is not detectable due to the huge amount of material around the target. Because of this, the four-momentum of the recoil particle has to be reconstructed using the known four-momenta P of the target particle, q of the virtual photon and ρ of the ρ^0-meson. The four-momentum of the ρ^0-meson is calculated by using the four-momenta of its decay particles π^+ and π^-. Figure 4.10 shows the distribution of the missing energy before applying the described cut.

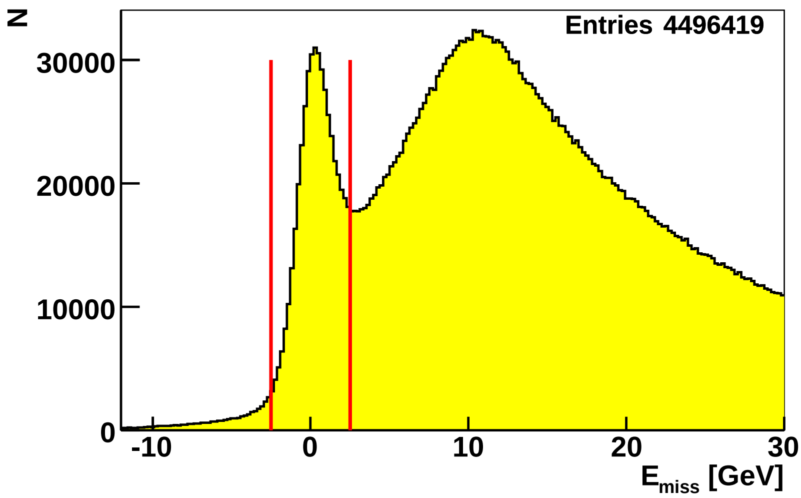

Figure 4.10: Distribution of the missing energy E_{miss} before applying the cut $|E_{miss}| < 2.5$ GeV. The restrictions of the cut are depicted with the superimposed red lines.

The next kinematical variable on which a cut is applied is the transverse momentum p_T^2 of the ρ^0-meson with respect to the direction of the virtual photon. As seen on the left hand side of figure 4.11, the distribution of p_T^2 is a superposition of three individual distributions: coherent scattering, incoherent scattering and background.[10] A cut on

[10]Coherent scattering means scattering on the nucleus. Incoherent scattering means scattering on the quarks themselves.

the lower and higher p_T^2 region is introduced to minimize the coherent scattering and the background part because only the incoherent scattering fraction is necessary for the analysis [51]. The borders of this cut are shown on the right hand side of figure 4.11, the numerical values are:

$$0.01\ (\mathrm{GeV/c})^2 < p_T^2 < 0.5\ (\mathrm{GeV/c})^2. \tag{4.4}$$

For reasons of statistics the lower cut is applied at 0.01 (GeV/c)^2 and not at a higher values as it is proposed by the plot. As a side effect of the lower cut on p_T^2, the angle ϕ_h between the lepton scattering plane and the hadron production plane is well-defined, due to the fact that a transverse component exists.

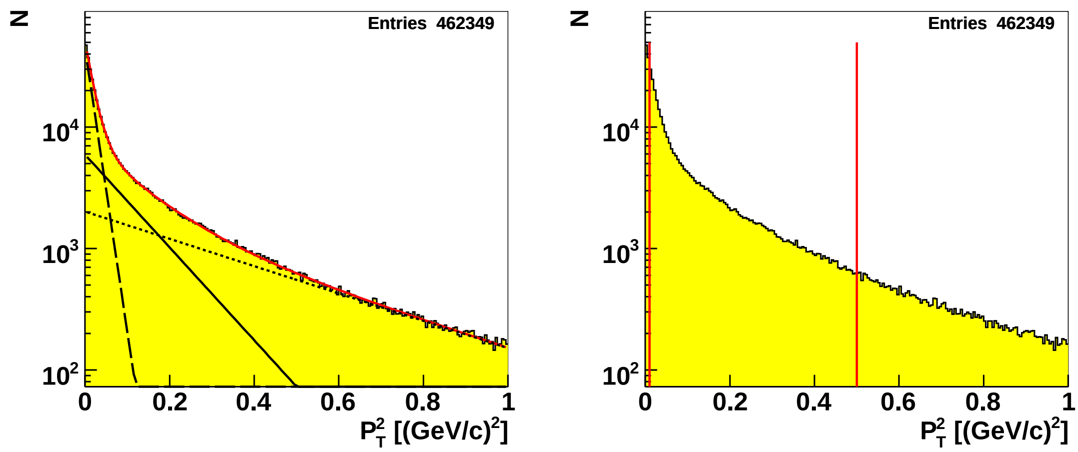

Figure 4.11: Distribution of the transverse component p_T^2. Shown on the left hand side: The distribution superimposed with the coherent part (solid line), the incoherent part (dashed line), the background (fine dashed line) and the superposition of these parts (red line). On the basis of a three-exponential fit on these three distributions, the incoherent part is separated. For reasons of statistics the lower cut is applied at a lower value as proposed by the fit. The upper and lower cut is indicated by the red lines on the right hand side.

Finally the invariant mass distribution given in figure 4.12 is inspected. There, the peak for the ρ^0-mesons is clearly visible at the expected ρ^0 mass of $M_\rho = 775.5$ MeV [31]. The invariant mass distribution has, besides the width of the ρ^0 peak, a small bump below 0.4 GeV/c^2. This small bump originates from the ϕ-mesons located at a wrong invariant mass, as charged pions are assigned to them as decay particles instead of kaons. To ensure that only ρ^0-mesons enter the analysis and to eliminate the non-resonant background, a mass cut around the ρ^0 mass is applied:

$$|M_\rho - M_{\pi\pi}| < 0.3\ \mathrm{GeV/c}^2, \tag{4.5}$$

where $M_{\pi\pi}$ is the calculated mass of the ρ^0-meson from its decay particle and M_ρ the one taken from the Particle Data Group [31].

Applying all these restrictions to the clean data sample, the exclusively produced ρ^0-mesons are selected. The restrictions and their impact is shown in table 4.5.

Table 4.5: Summary of the applied cuts.

Cut Description	Events after Cut
Events at Start (Initial Sample)	69,964,400
Events after Data Quality (Clean Sample)	49,662,410
Vertex:	
Primary Vertex, Vertex in Target	43,020,580
Beam Muon μ:	
High Momentum	43,011,750
Quality Check	42,921,690
Track crossed all Cells	42,627,110
Scattered Muon μ':	
Recovery Process	42,324,210
Quality Check	39,570,320
Crossed Yoke of SM2	37,945,490
Exclusivity:	
Three Outgoing Particles	9,662,080
Hadrons have opposite Charge	6,536,686
SIDIS:	
Photon Virtuality Q^2	6,530,361
Invariant Mass W	5,660,991
Relative Energy Transfer y	5,228,806
Outgoing hadrons (π^+, π^-):	
Quality Check	5,076,115
Hit behind SM1	4,596,661
Belong to Primary Vertex	4,514,751
Crossed Yoke of SM2	4,508,396
Misidentified μ'	4,496,419
ρ^0-Meson:	
Missing Energy E_{miss}	462,349
Transverse Momentum p_T^2	328,607
Invariant Mass M_ρ	262,957
Final Number of ρ^0-mesons	262,957

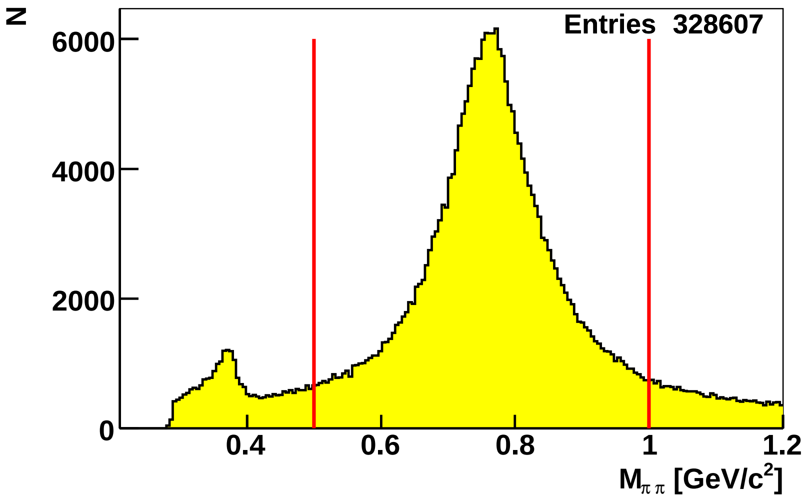

Figure 4.12: Invariant mass distribution with a tall peak originating from the ρ^0-mesons, located at the right invariant mass value, and a small bump, originating from the ϕ-mesons, located at a wrong invariant mass value. The cut to separate only the ρ^0-mesons is indicated by the red lines.

4.4 Final Data Sample

This section will present the distributions of the kinematical variables as well as the statistical values obtained by applying the event selection described in section 4.3.
Table 4.6 gives an overview of the statistics obtained during the 2007 transverse data taking periods. Elements listed in this table are the periods of data taking, the number of recorded runs, the number of events within these runs and finally the obtained number for the selected ρ^0-mesons. Distributions of the kinematical variables x_{Bj}, Q^2, p_T^2, $-t'$, W and y can be found in figures 4.13 - 4.15, their corresponding mean values for the final data sample are given in table 4.7.[11]

For the events of the final data sample, the method for extraction of the asymmetry $A_{UT}^{\phi_h-\phi_S}$ will be presented in the next chapter, the final results will be given and will be discussed in chapter 6.

[11] $t' = t - t_0$, with t_0 being the minimal kinematically allowed value of t.

Table 4.6: Number of ρ^0-events after applying the event selection. W42 is split into W42a and W42b because of the reason that for the asymmetry calculation a double-period partner for W41 and W43 is needed.

Period	# Runs	Events / 10^6	Final Sample
W25	121	8.90	36,651
W26	94	8.01	40,545
W39	140	14.27	46,251
W40	44	8.01	29,305
W41	99	10.75	42,969
W42	135	14.50	44,791
W42a	*98*		*28,288*
W42b	*37*		*16,503*
W43	44	5.53	22,718
SUM	812	69.97	262,957

Table 4.7: Mean values of the relevant kinematical variables.

$\langle x_{Bj} \rangle$	=	0.037
$\langle Q^2 \rangle$	=	2.10 (GeV/c)^2
$\langle p_T^2 \rangle$	=	0.112 (GeV/c)^2
$\langle -t' \rangle$	=	0.123 (GeV/c)^2
$\langle y \rangle$	=	0.255
$\langle W \rangle$	=	8.28 GeV/c^2

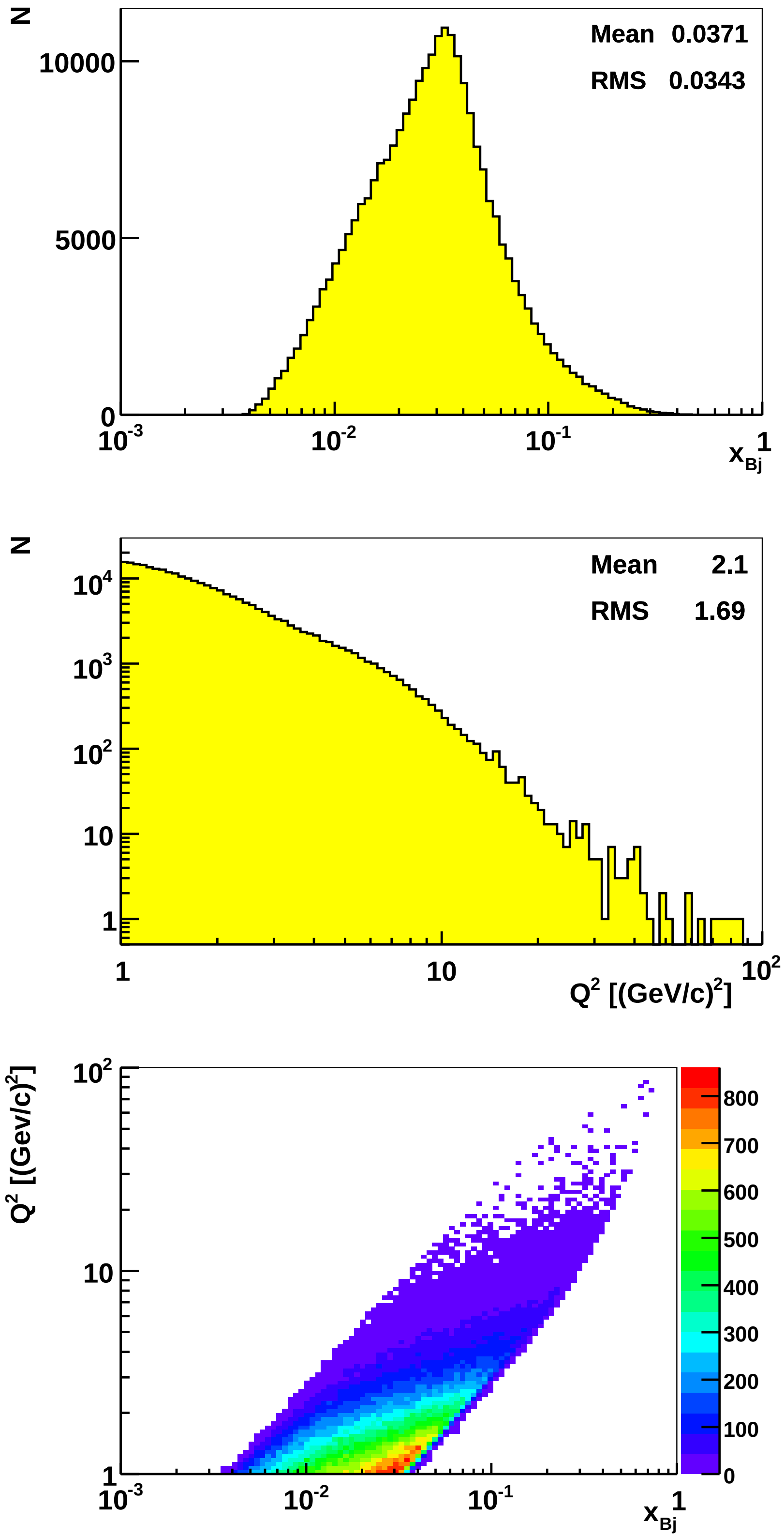

Figure 4.13: Distribution of the kinematical variables x_{Bj} and Q^2, together with a two dimensional plot of x_{Bj} versus Q^2. The 2D plot shows that x_{Bj} and Q^2 are correlated. For higher values of Q^2 higher values for x_{Bj} are found.

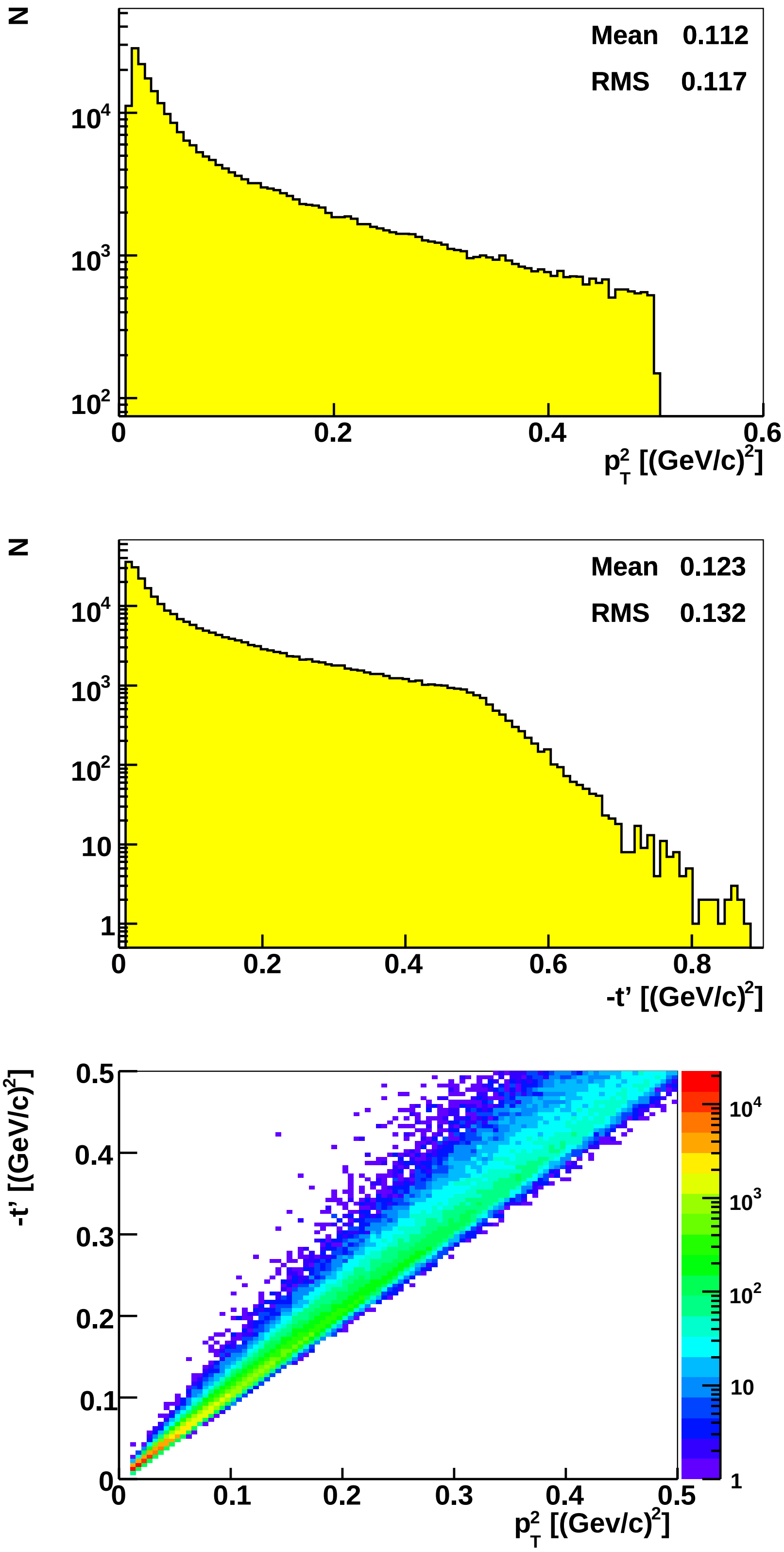

Figure 4.14: Distribution of the kinematical variables p_T^2 and $-t'$, together with a two dimensional plot of p_T^2 versus $-t'$. From the 2D plot it becomes clear, that these two variables are strongly correlated.

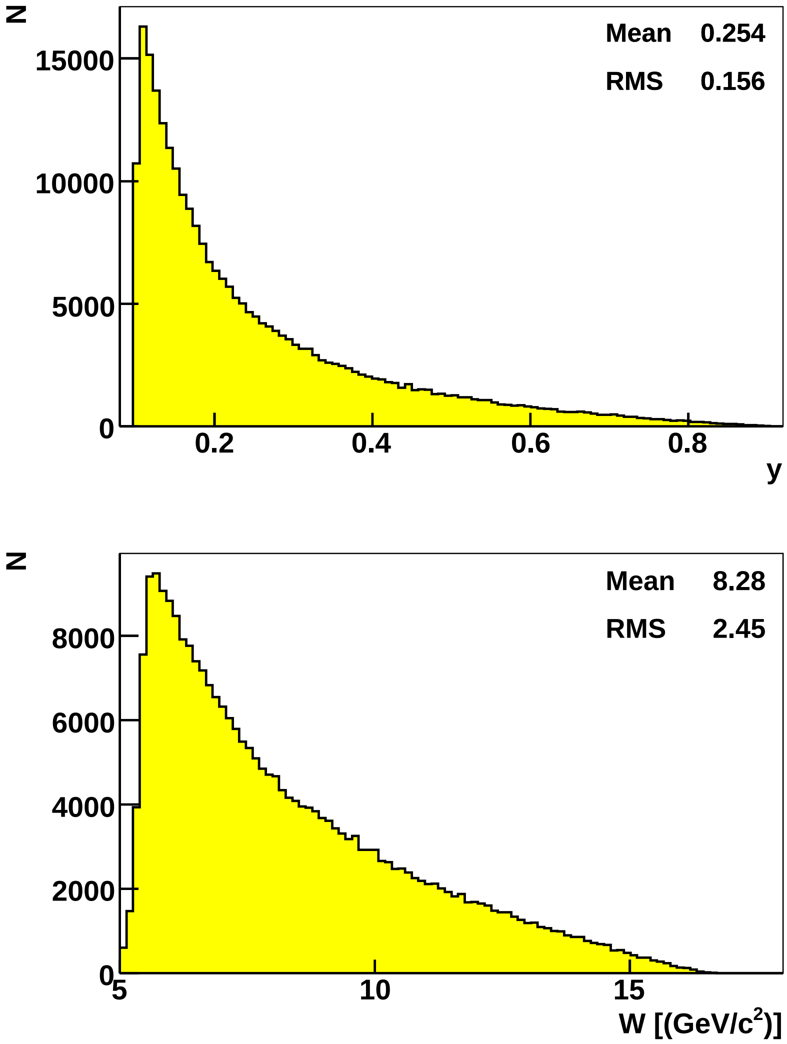

Figure 4.15: Distribution of the kinematical variables y and W.

5. Method for Extraction of the Azimuthal Asymmetries

After having described the selection of the events in the previous chapter, this chapter will introduce the method which is applied for extracting the azimuthal asymmetry. Some general remarks about the framework in which the method is applied will be given (sec. 5.1). After that, the used fit method will be introduced, namely the “Two Dimensional Fit to Counts Method” (sec. 5.2). The chapter will close with the method used to combine the extracted asymmetries amplitudes for the several data taking periods (sec. 5.3).

5.1 General Remarks

For extracting the azimuthal asymmetries it is essential to assign the selected ρ^0-events to the target cell in which the event took place and thus to the corresponding configuration of the target spin. During the 2007 data taking, a target consisting of three cells was used, whereas the central cell had double the size of the two outer cells[1]. Furthermore, the target was always polarized in one direction in the two outer cells and in the opposite direction in the central cell. An illustration of the setup is given in figure 5.1, detailed information about the target can be found in section 3.2.

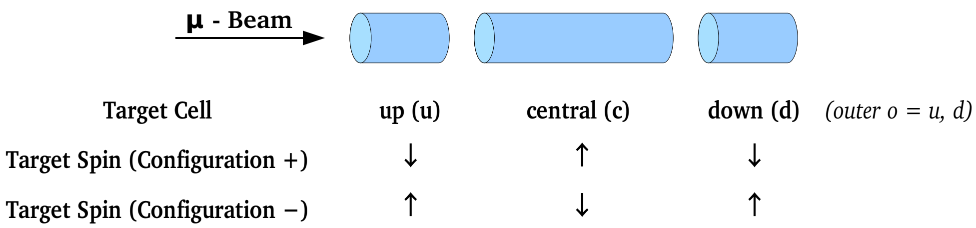

Figure 5.1: Illustration of the target configuration. The target is build up by three cells (up, central, down), with the outer cells (up, down) always having the opposite spin configuration compared to the double-sized central cell.

The number of events N in the outer cells are summed up and will be indicated by the index o, while the number of events in the center cell will be denoted with the index c. The two different target spin configurations are referred to as $+$ and $-$. This results in

[1]The outer cells are sometimes referred to as up/upstream and down/downstream cell.

four different count numbers representing the events taken place in a certain cell and during a certain polarization configuration: $N_o^+, N_o^-, N_c^+, N_c^-$.

Including physics as introduced in equation 2.22 the number of counts can be described by the equation:

$$N_{o,c}^{\pm} = F_{o,c}^{\pm}\, n_{o,c}\, \sigma_0\, \tilde{a}_{o,c}^{\pm}(\phi_h, \phi_S) \cdot \Big(1 \pm P_{T;o,c} \cdot f \cdot A_{UT,raw}^{\sin(\phi_h-\phi_S)} \cdot \sin(\phi_h - \phi_S)\Big)\,, \tag{5.1}$$

with F being the muon flux, n the number of target nucleons, σ_0 the unpolarized cross-section, $\tilde{a}$ the acceptance[2], P_T the degree of polarization of the target and f the so-called dilution factor (information about P_T and f in sec. 5.1.2). $A_{UT,raw}^{\sin(\phi_h-\phi_S)}$ represents the Transverse-Target Single-Spin Asymmetry Amplitude (TTSA) as described in section 2.3.4. It is indexed with a subscripted *raw* because it has to be corrected due to the finite width of the bins, which will be described in detail in section 5.2.5.
Since one cannot discern F, n, σ_0 and $\tilde{a}$ from the number of counts, the normed acceptance is defined:

$$a_{o,c}^{\pm}(\phi_h, \phi_S) = F_{o,c}^{\pm}\, n_{o,c}\, \sigma_0\, \tilde{a}_{o,c}^{\pm}(\phi_h, \phi_S). \tag{5.2}$$

5.1.1 Reasonable Assumption

For the normed acceptances a so-called Reasonable Assumption implies that the ratio

$$\frac{a_o^-(\phi_h, \phi_S)}{a_c^+(\phi_h, \phi_S)} = \frac{a_o^+(\phi_h, \phi_S)}{a_c^-(\phi_h, \phi_S)} \cdot C \tag{5.3}$$

is constant. This is assumed to be valid for every bin. An assumption like this has to be included in order to reduce the number of free parameters in the approach.

5.1.2 Target Polarization and Dilution Factor

The COMPASS experiment used a polarized NH_3 target, which was introduced in section 3.2. It is impossible to completely polarize the NH_3 material in the target. Only the H can be polarized, and thus, not all scattering events take place at a polarized proton.
The degree of target polarization $P_{T;o,c}$ is obtained independently for each of the different target cells. A nuclear magnetic resonance process is used to measure the values during the target is longitudinally polarized. This means for the transverse data taking that values can only be measured when the polarization is flipped between two periods. Therefore, an interpolation for the polarization values of one certain period is performed with the values measured before and after [52]. A polarization of about 70% - 95% was obtained during the present data taking periods [48].

Apart from the degree of polarization another factor must be taken into account for the calculation, due to the fact that there is also material surrounding the target and material contaminating it. In these materials scattering events also take place. The factor

[2]The COMPASS spectrometer has an limited angular acceptance, thus its sensitivity follows a distribution from 0 to 2π.

describing how many scattering events take place on a polarized proton in relation to the overall scattering events is called dilution factor f. For the present target material the dilution factor is taken from [36]: $f = 0.15$.

5.2 The 2D Fit To Counts Method

For extracting the spin dependent asymmetry amplitude a 2D Fit to Counts Method was chosen. This section will first briefly motivate the choice of this method. Then, general aspects about the 2D Fit to Counts Method will be given, before introducing Poisson statistic. The resulting minimization problem will be solved with the help of the Levenberg-Marquardt Algorithm, for that reason it is presented as theoretical approach and applied to the problem. As a binned method is used, a correction factor will be derived to correct the asymmetry amplitude extracted from the fit. Finally, it will be summarized how the physical asymmetry amplitude is extracted using all this components.

5.2.1 Motivation

As introduced in section 2.3.4 the TTSA depends on the difference between the angles ϕ_h and ϕ_S. Their angular distribution reflects a convolution of the acceptance of the spectrometer and the physical asymmetry amplitude. A 2D plot showing the selected events on a ϕ_h-ϕ_S-grid is given in figure 5.2.

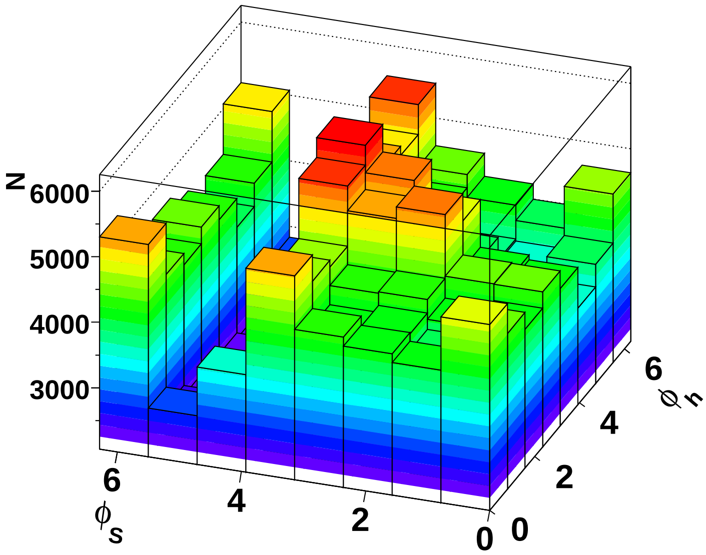

Figure 5.2: Description of the angular distributions ϕ_h and ϕ_S in two dimensions. Their angular distribution reflects a convolution of the acceptance of the spectrometer and the physical asymmetry amplitude. ϕ_S shows a strong angular dependence, ϕ_h a minor angular dependence.

The figure shows that the angular dependence of the two angles differs: ϕ_S shows a strong angular dependence, ϕ_h a minor angular dependence. In order to take the different angular dependences of the two angels into account and thus the acceptance of the spectrometer, a two dimensional fit method is chosen.

In the present case, in which a binned fit method is used, the fit is applied on the counts in each bin. The bins are filled with the number of events N from the event selection. If the number of bins is high, low statistics is expected in some bins. Therefore, it has to be taken care of that the distribution of the counts in the bins is described by the right mathematical approach. For example, Gaussian distribution can only be assumed for counting numbers about ten and above. Hence, Poisson distribution is the better choice when statistics is marginal. For the chosen two dimensional fit, a high number of bins has to be used and so, low statistics is expected in some bins. As a result a fit to counts method is used including Poisson statistic. The method is called 2D Fit to Counts Method [53].

5.2.2 General Remarks

The 2D Fit to Counts Method uses a two-dimensional binning in ϕ_h and ϕ_S. For statistical reasons, eight equidistant bins are chosen for each angle resulting in a 8×8 grid, where the bins are numbered serially from 1 to 64 (see figure 5.3).

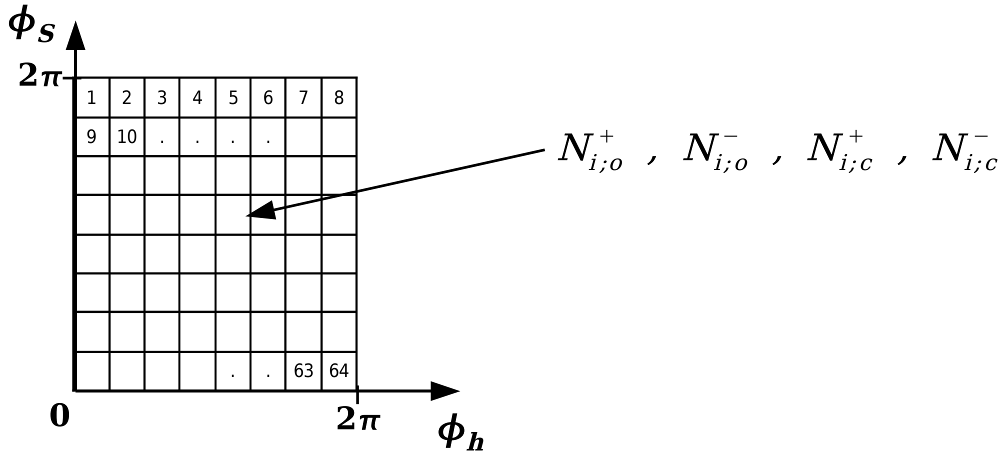

Figure 5.3: Illustration of the 8×8 grid used for the 2D Fit to Counts Method. For each angle ϕ_h and ϕ_S eight equidistant bins are chosen, resulting in 64 bins numbered serially. To every bin i, four counters $N^{\pm}_{i;o,c}$ are assigned, resulting in 256 counters.

According to the bins $i = 1, 2, \ldots, 64$, the four counters $N^{\pm}_{i;o,c}$ defined in formula 5.1 are assigned to them. The counters are filled with the events from the selected sample, as described in section 4.3. For every selected ρ^0-event all required physical information is stored, for example ϕ_h, ϕ_S, degree of polarization or target spin configuration. To correct acceptance effects, the Reasonable Assumption (eq. 5.3) is applied for every single bin i:

$$C = \frac{a^+_{i;o} \cdot a^+_{i;c}}{a^-_{i;o} \cdot a^-_{i;c}}. \tag{5.4}$$

Applied to the physical description of the count rates this yields to four equations:

$$\begin{aligned}
N^+_{i;o} &= C \cdot \frac{a^-_{i;o} \cdot a^-_{i;c}}{a^+_{i;c}} \cdot \left(1 + P_{T;o} \cdot f \cdot A^{\sin(\phi_h - \phi_S)}_{UT,raw} \cdot \sin(\phi_h - \phi_S)\right), && (5.5)\\
N^+_{i;c} &= a^+_{i;c} \cdot \left(1 + P_{T;c} \cdot f \cdot A^{\sin(\phi_h - \phi_S)}_{UT,raw} \cdot \sin(\phi_h - \phi_S)\right), && (5.6)\\
N^-_{i;o} &= a^-_{i;o} \cdot \left(1 - P_{T;o} \cdot f \cdot A^{\sin(\phi_h - \phi_S)}_{UT,raw} \cdot \sin(\phi_h - \phi_S)\right), && (5.7)\\
N^-_{i;c} &= a^-_{i;c} \cdot \left(1 - P_{T;c} \cdot f \cdot A^{\sin(\phi_h - \phi_S)}_{UT,raw} \cdot \sin(\phi_h - \phi_S)\right). && (5.8)
\end{aligned}$$

Now, the task is to solve this nonlinear system, consisting of 256 equations with 194 fit parameters.[3] As a result, the asymmetry amplitude and the acceptance parameters are provided.

For clarity reasons the cell and polarization configuration will be omitted from now on, the fit parameters will be combined to a vector and the fit functions will be given by a function vector. Hence, equations 5.5 - 5.8 can be written as

$$N_j = g_j(\vec{x}), \tag{5.9}$$

with $1 < j < 256$ including the 64 bins as well as the 4 different cell and target configurations. N_j being the number of counts in bin j, and g_j being the associated fit function with parameters $\vec{x} = (x_1\ ,\ x_2\ ,\ \ldots\ ,\ x_{194}) = (a^{\pm}_{1;o,c}\ ,\ \ldots\ ,\ a^{\pm}_{64;o,c}\ ,\ C\ ,\ A^{\sin(\phi_h - \phi_S)}_{UT,raw})$.

According to the discussion from section 5.2.1 it is required to insert Poisson statistic into the approach, which will be done next.

5.2.3 Poisson Statistic

As low event numbers should be allowed in each bin, statistical distributions have to be taken into account at this point. In section 5.2.1 it was already derived that Poisson statistic should be used in the present case.
Given the parameters $\vec{x}$, the probability of N_j in Poisson statistic is:

$$P_j(\vec{x}) = \frac{e^{-g_j(\vec{x})} g_j(\vec{x})^{N_j}}{N_j!}. \tag{5.10}$$

As fit function the likelihood can be used and maximized (maximum likelihood method), which is given for $\vec{x}$ by:

$$\mathcal{L}^*(\vec{x}) = \prod_{j=1}^{m} P_j(\vec{x}), \tag{5.11}$$

---

[3] 256 equations = 4 equations $\cdot$ 64 bins.
194 fit parameter $= 64 \cdot (a^+_{i;c} + a^-_{i;c} + a^-_{i;o}) + C + A^{\sin(\phi_h - \phi_S)}_{UT,raw}$.

where $m = 256$ is the number of equations.
Since maxima are unaffected by monotone transformations, the logarithm can be applied to turn the product into a sum (log likelihood):

$$\mathcal{L}(\vec{x}) = \sum_{j=1}^{m} \ln\left(P_j(\vec{x})\right) \stackrel{5.10}{=} \sum_{j=1}^{m} \left(-g_j(\vec{x}) + N_j - N_j \ln\left(\frac{N_j}{g_j(\vec{x})}\right)\right). \tag{5.12}$$

With the factor -2, the log likelihood corresponds to the deviance and follows a χ^2 distribution. Hence, the problem is now reduced to the minimization of the corresponding deviance given as:

$$\mathcal{D}(\vec{x}) = \sum_{j=1}^{m} \left(2(g_j(\vec{x}) - N_j) + 2N_j \ln\left(\frac{N_j}{g_j(\vec{x})}\right)\right). \tag{5.13}$$

For this non-trivial task the Levenberg-Marquardt Algorithm is used.

5.2.4 The Levenberg-Marquardt Algorithm

The algorithm used to solve the minimization problem of equation 5.13 is the Levenberg-Marquardt Algorithm (LMA) [54, 55]. It can be understood as the combination of the Gauss-Newton Algorithm and the gradient descent method. Its advantage is that it finds a solution, even if the starting points are far away from the final minimum.
This section will first introduce the theoretical approach of the LMA and then apply the LMA to the given problem.

Theoretical Approach for the LMA

The LMA finds the minimum of a function $F(\vec{x})$, defined as a sum of squares of m nonlinear functions f_j:

$$F^*(\vec{x}) = \frac{1}{2}\sum_{j=1}^{m} [f_j(\vec{x})]^2 = \frac{1}{2}||\vec{f}(\vec{x})||^2, \tag{5.14}$$

where $\vec{x} = (x_1, x_2, \ldots, x_n)$ is a vector of n parameters and $\vec{f} = f_1, f_2, \ldots, f_m$ is a vector of m nonlinear functions. With the Jacobian matrix $J(\vec{x}) = \frac{\partial f_j}{\partial x_i}$, $1 \leq j \leq m, 1 \leq i \leq n$, the minimization is done iteratively in k steps by solving the linearized version of the problem:

$$F(\vec{x}) = \frac{1}{2}||\vec{f}(\vec{x}_k)J(\vec{x}_k)(\vec{x} - \vec{x}_k)||^2. \tag{5.15}$$

Minimization with $\nabla F = 0$ leads to:

$$\vec{x}_{min} = \vec{x}_k - (J^T J)^{-1} J^T \vec{f}(\vec{x}_k). \tag{5.16}$$

Solving this equation the standard way would lead to the Gauss-Newton method. The Gauss-Newton method thus has a problem when the starting point is far away from the solution, a case in which the gradient descent method works better. For this reason, the Levenberg-Marquardt Algorithm combines both methods by using a damping term λI additionally, with $\lambda \in \mathbf{R}^+$ and I being the identity matrix:

$$\vec{x}_{min} = \vec{x}_k - (J^T J + \lambda I)^{-1} J^T \vec{f}(\vec{x}_k). \tag{5.17}$$

If $\vec{x}_k$ is distant to the solution, λ is increased by the algorithm and the algorithm works as a gradient descent method. Advancing towards the solution, λ is decreased by the algorithm, so that the rapid convergence characteristic of the Gauss-Newton method maintains. Therefore, the LMA combines the two complementary advantages of the Gauss-Newton and the gradient descent method.
Calculating $\vec{x}_{min}$ as suggested in equation 5.17 requires the calculation of an inverse matrix, which can be very time-consuming. As suggested by [56] this problem can be avoided using the GNU Scientific Library (GSL) [57], as it uses the pseudo inverse matrix for performing the LMA.

Applying the LMA to the 2D Fit to Counts Method

To make use of the LMA in the present analysis, the functions $f_j(\vec{x})$ have to be adapted to the problem of the 2D Fit to Counts Method in equation 5.13. Hence, the functions $f_j(\vec{x})$ have to be chosen in such a way that they are derived from Poisson statistic. For this reason, the deviance of the maximum likelihood $\mathcal{D}(\vec{x})$ has to be adapted to the LMA function $F(\vec{x})$.
Therefore, a square-root has to be introduced to the deviance, since the LMA minimizes F in a quadratic sense. After this adaptation, the target functions for the LMA are derived as

$$f_j(\vec{x}) = \sqrt{\left(2(g_j(\vec{x}) - N_j) + 2N_j \ln\left(\frac{N_j}{g_j(\vec{x})}\right)\right)}. \tag{5.18}$$

Handing over these functions $f_j(\vec{x})$ and their Jacobian matrix $J = \partial f_j / \partial x_i$ to the Levenberg-Marquardt Algorithm of the GSL, the system of nonlinear equations can be solved and the asymmetry amplitude can be extracted.

5.2.5 Corrections due to Finite Bin Size

The asymmetry amplitude extracted from the algorithm as explained so far, is not yet the requested physical asymmetry amplitude. A correction due to the finite bin size has to be performed, because the value for the extracted asymmetry amplitude is obtained by using a binned two dimensional grid in ϕ_h and ϕ_S. This has the effect that the fit is performed at the center of the bin. Therefore, a factor has to be calculated to correct this effect by comparing the mean value of the fit function in a certain bin with the value of the function at the point of evaluation [58].

In the case of the present analysis the fit function is given by:

$$f(\phi_h, \phi_S) = 1 \pm A_{UT}^{\sin(\phi_h - \phi_S)} \cdot \sin(\phi_h - \phi_S). \tag{5.19}$$

Assuming n bins for both angles, the bin widths are $\Delta\phi_{h,S} = 2\pi/n$. Thus, the height of the fit function at the center of the bin (ϕ'_h, ϕ'_S) is:

$$f(\phi'_h + \tfrac{\Delta\phi_h}{2}, \phi'_S + \tfrac{\Delta\phi_S}{2}) = 1 \pm A_{UT,fit}^{\sin(\phi_h-\phi_S)} \cdot \sin\left((\phi'_h + \tfrac{\Delta\phi_h}{2}) - (\phi'_S + \tfrac{\Delta\phi_S}{2})\right). \quad (5.20)$$

This is the value of the asymmetry amplitude extracted by the LMA.

In contrast to that, the true value can be extracted by calculating the integral over the bin, which has to equal the content of the bin. This results in calculating the mean value of the fit function in bin (ϕ'_h, ϕ'_S):

$$\langle f(\phi'_h, \phi'_S)\rangle = \tfrac{1}{\Delta\phi_h\Delta\phi_S} \int_{\phi'_h}^{\phi'_h+\Delta\phi_h} \int_{\phi'_S}^{\phi'_S+\Delta\phi_S} \left(1 \pm A_{UT,true}^{\sin(\phi_h-\phi_S)} \cdot \sin(\phi_h - \phi_S)\right) d\phi_h d\phi_S$$

$$= 1 \pm A_{UT,true}^{\sin(\phi_h-\phi_S)} \cdot \tfrac{2}{\Delta\phi_h} \sin\tfrac{\Delta\phi_h}{2} \cdot \tfrac{2}{\Delta\phi_S} \sin\tfrac{\Delta\phi_S}{2} \cdot \sin\left((\phi'_h + \tfrac{\Delta\phi_h}{2}) - (\phi'_S + \tfrac{\Delta\phi_S}{2})\right). \quad (5.21)$$

The comparison of equation 5.20 with equation 5.21 shows that the two equations are only identical for the limiting case of $n \to \infty$. For all other cases a correction factor can be determined as follows:

$$f_{\text{binning}} = \frac{A_{UT,fit}^{\sin(\phi_h-\phi_S)}}{A_{UT,true}^{\sin(\phi_h-\phi_S)}} = \frac{2}{\Delta\phi_h} \sin\frac{\Delta\phi_h}{2} \cdot \frac{2}{\Delta\phi_S} \sin\frac{\Delta\phi_S}{2} \quad (5.22)$$

In the case of the present analysis an 8×8 binning was chosen, the correction factor then evaluates to:

$$f_{\text{binning}} = \frac{A_{UT,fit}^{\sin(\phi_h-\phi_S)}}{A_{UT,true}^{\sin(\phi_h-\phi_S)}} = 0.949641. \quad (5.23)$$

It should be mentioned that such a correction due to a finite bin size is necessary in all binned fit algorithms.

5.2.6 Obtaining the Physical Asymmetry

To summarize this section, the procedure on how to obtain the asymmetry amplitude $A_{UT}^{\sin(\phi_h-\phi_S)}$ from a given data sample is presented.
First, the *raw* asymmetry amplitude is extracted with the 2D Fit to Counts Method, using the GSL implementation of the Levenberg-Marquardt Algorithm. For this reason, the physical description of the asymmetry amplitude has to be adapted to an appropriate form in order to fit the LMA. The fit takes the target polarization and the target dilution factor into account and uses Poisson statistic.
Second, the extracted raw asymmetry amplitude has to be corrected due to the use of a binned method.
Hence, the final value for the asymmetry amplitude is calculated as follows:

$$A_{UT}^{\sin(\phi_h-\phi_S)} = \frac{A_{UT,raw}^{\sin(\phi_h-\phi_S)}}{f_{\text{binning}}} \quad (5.24)$$

Until this point, the described method is used for extracting the asymmetry amplitude for two opposite polarized periods of data taking (double-periods). For the calculation of the asymmetry amplitude for the whole set of the recorded data, a last step has to be implemented to combine the individual double-periods.

5.3 Extracting the Physical Asymmetry for the whole Data Sample

Up to now, the procedure to extract the physical asymmetry for one double-period was described. The data taken in the year 2007 contains four double-periods, for which the asymmetry amplitude can be extracted using the explained method.
To obtain the overall asymmetry amplitude of all the available periods, the data first has to be grouped in a certain way, then the individual asymmetries have to be combined. This procedure will be the content of this section.

5.3.1 Data Grouping

The extraction of the asymmetry amplitude requires two periods with different target spin polarization configurations (+ and −). These two periods have to be recorded under similar conditions, e.g. same acceptance for the events from the outer (central) target cells. It shows that this requirements are fulfilled best for sequential periods. Table 5.1 gives an overview of how the periods are combined.

Table 5.1: Data grouping into double-periods. Each period is given with its polarization configuration and the obtained statistics.

Double-Period	Periods	Target Polarization	# Rhos
1	W25	+	36,651
	W26	−	40,545
2	W39	−	46,251
	W40	+	29,305
3	W41	+	42,969
	W42a	−	28,288
4	W42b	−	16,503
	W43	+	22,718

5.3.2 Calculating the overall Asymmetry

Using the extraction method explained in section 5.2, the physical asymmetry amplitudes for the several double-periods are calculated. To obtain the asymmetry amplitude for the whole data taking period, the results from the four different double-periods have to be combined. This is done by calculating the weighted mean of the four results from the different double-periods:

$$A_{UT}^{\sin(\phi_h-\phi_S)} = \frac{\sum_{i=1}^{4}\left(A_i/\sigma_i^2\right)}{\sum_{i=1}^{4}\left(1/\sigma_i^2\right)}, \qquad \sigma_{A_{UT}} = \frac{1}{\sqrt{\sum_{i=1}^{4}\left(1/\sigma_i^2\right)}}, \tag{5.25}$$

where A_i denotes the extracted asymmetry amplitudes of the four double-periods i and σ_i denotes the associated errors given by the fit.

The TTSA obtained in this way is calculated for eight different kinematical variables:

$$x_{Bj},\ Q^2,\ p_T,\ y,\ -t',\ p_T^2,\ E_{miss},\ M_\rho.$$

Every variable is split into five bins with approximately the same statistics. With this approach, possible kinematical dependencies of the TTSA can be investigated and compared to theoretical predictions and to results from other experiments.

The results obtained by this method will be presented and discussed next.

6. Results and Discussion

This chapter will present the results obtained for the Transverse-Target Single-Spin Asymmetry Amplitude $A_{UT}^{\sin(\phi_h-\phi_S)}$. The amplitude was extracted using the 2D Fit to Counts Method described in chapter 5, whereby the method was applied on data taken in 2007 at the COMPASS experiment and from events selected as described in chapter 4.3.
The asymmetry amplitudes will be presented (sec. 6.1) and the compatibility of the results will be checked (sec. 6.2). They will be compared to theoretical predictions (sec. 6.3), to measurements and calculations obtained at the HERMES experiment (sec. 6.4) and finally to TTSAs obtained on a deuteron target at the COMPASS experiment (sec. 6.5). Finally, possible further investigations will be discussed (6.6).

6.1 The Calculated Asymmetries

Figure 6.1 gives the TTSAs for the kinematical variables x_{Bj}, Q^2, p_T and y. The values are plotted against the mean value of each variable in every bin. The binning is chosen in such a way that the statistics in every bin is approximately the same. The numerical values for the asymmetries and the numerical values for the bin borders can be found in appendix A. The same holds for figure 6.2 in which the TTSAs for the kinematical variables $-t'$, p_T^2, E_{miss} and M_ρ are presented.
In figure 6.2 it becomes clear that the variables $-t'$ and p_T^2 are strongly correlated, as pointed out in [59]. For COMPASS, p_T^2 is the favored variable of these two variables, because its resolution is significantly better than the one from $-t'$. Additionally, p_T^2 is unbiased in contrast to $-t'$, which is biased due to the fact that t_0 can only be determined in an unsatisfactory way [59]. Anyhow, the TTSAs are given for both values, as theoretical predictions often refer to $-t'$.

Summarizing the results from these plots, it is evident that almost all TTSAs have a negative value. This fact can be strengthened by calculating the overall weighted mean for the individual kinematical variables over the full range of the covered kinematic, which has a distance of over 1.5σ to zero:

$$A_{UT}^{\sin(\phi_h-\phi_S)} = -0.037 \pm 0.023. \tag{6.1}$$

The meaning of these results will be explained in the following by comparing them with theoretical predictions and results from another experiment.

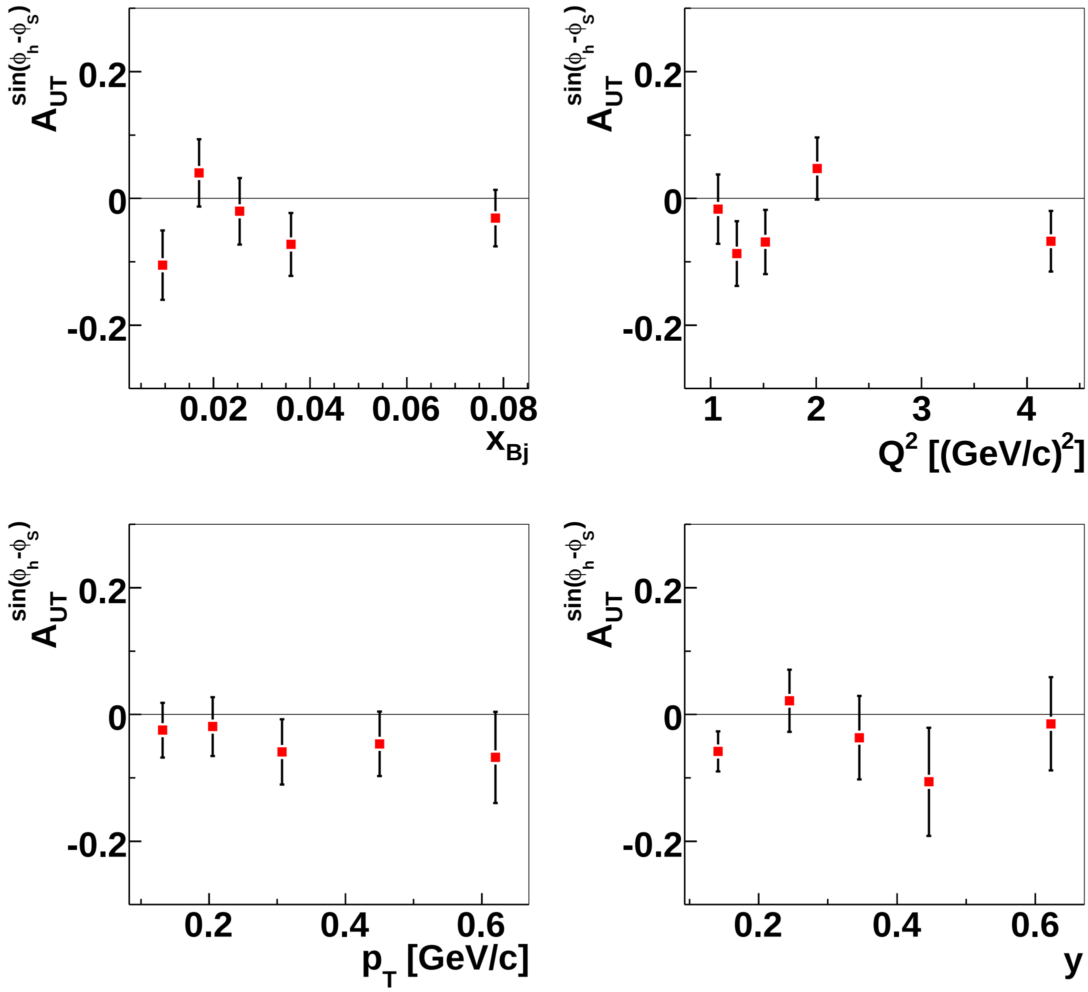

Figure 6.1: Results for the TTSAs $A_{UT}^{\sin(\phi_h-\phi_S)}$ for the kinematical variables x_{Bj}, Q^2, p_t and y. For every variable the asymmetry is split into five bins with approximately the same statistics. The asymmetries are plotted against the mean value of the kinematical variable in the according bin. Almost all asymmetry amplitudes have negative values.
For x_{Bj} especially the bins with a higher value of x_{Bj} are important, since theoretical predictions are only available in this region. In this bins of x_{Bj}, the mean value for Q^2 is also higher than in the lower ones, because x_{Bj} and Q^2 are correlated.

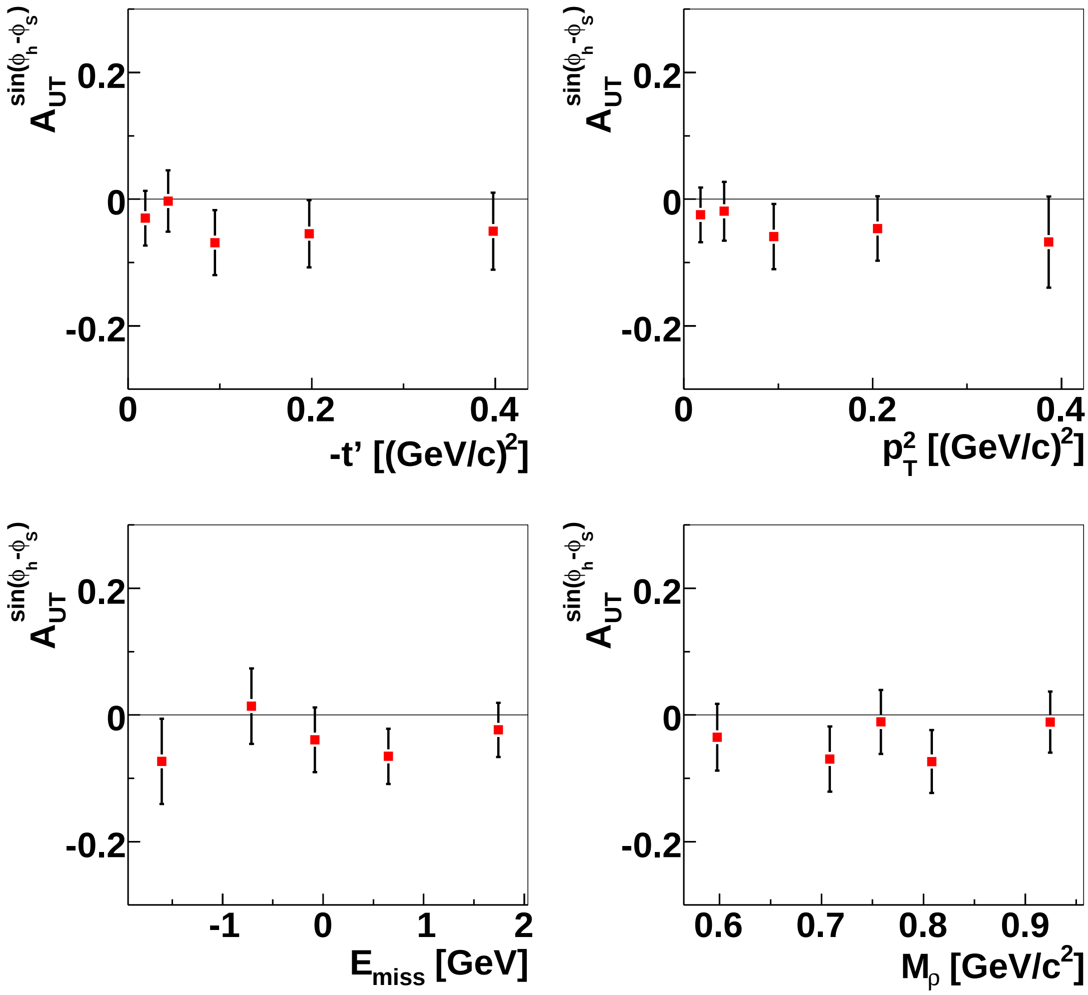

Figure 6.2: Results for the TTSAs $A_{UT}^{\sin(\phi_h-\phi_S)}$ for the kinematical variables $-t'$, p_T^2, E_{miss} and M_ρ. For every variable the asymmetry is split into five bins with approximately the same statistics. The asymmetries are plotted against the mean value of the kinematical variable in the according bin and almost all asymmetry amplitudes have negative values.
The variables p_t^2 and $-t'$ are strongly correlated as pointed out in [59] and as confirmed by the similar results shown in this plot.

6.2 Compatibility of the Results

To examine the consistency of the results calculated from the different double-periods, a check on their compatibility is performed. Therefore, a pull distribution is calculated in the following way:

$$\text{pull} = \frac{A_i - \langle A \rangle}{\sqrt{\sigma^2_{A_i} - \sigma^2_{\langle A \rangle}}} \qquad (i = 1, \ldots, 4), \tag{6.2}$$

with i denoting the four used double-periods, A_i the obtained TTSAs, σ_{A_i} the associated errors, $\langle A \rangle$ the weighted mean TTSA over all periods and $\sigma_{\langle A \rangle}$ the error on the weighted mean.

Figure 6.3 presents the pull distribution as well as the application of a Gaussian fit. As the fit is centered around zero (Mean = 0.11 ± 0.08) with an RMS around one (RMS = 0.98 ± 0.05), the compatibility of the results is confirmed. Around -2 a higher number of entries can be seen, which arise from the fact that double-period W42b/W43 lacked on data quality compared to the other weeks. The number of 160 entries for the distribution is obtained by four double-periods times eight kinematical variables times five kinematical bin ranges.

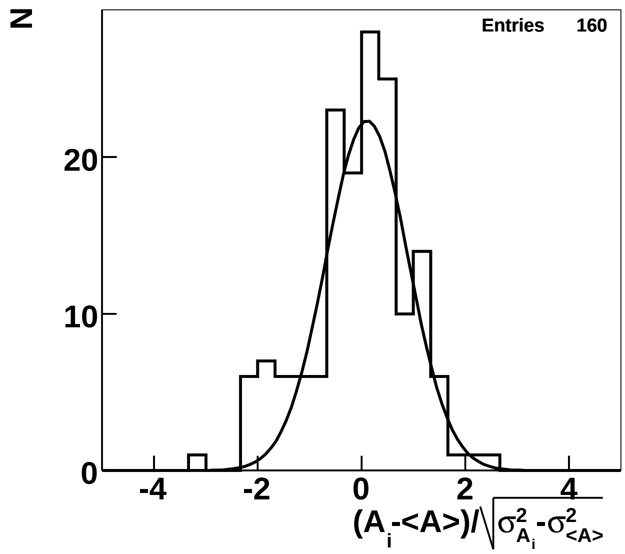

Figure 6.3: Check of the compatibility of the results. A pull distribution is computed using the obtained TTSAs from the several double-periods A_i, the associated errors σ_{A_i}, the weighted mean TTSA over all periods $\langle A \rangle$ and the error on the weighted mean $\sigma_{\langle A \rangle}$. A Gaussian fit on the distribution is centered around zero (Mean = 0.11 ± 0.08) and has an RMS around one (RMS = 0.98 ± 0.05). This fit result confirms the compatibility of the results.
An analysis concerning the high number of entries around -2 resulted in the fact that double-period W42b/W43 lacked on data quality compared to the other periods.

6.3 Comparison with Theoretical Predictions

After introducing some general remarks about the validity of the theoretical predictions with respect to the obtained results, a comparison of the results with calculations from [18] will be discussed.

6.3.1 General Remarks

Two points have to be mentioned before comparing the results with available calculations. First, recent lattice calculations [60] are obtained with the assumption that the total angular momentum of the down-quarks in the nucleon is $J^d = 0$. This is used in the available theoretical predictions and is assumed to hold in the results of this thesis as well.
Second, as already mentioned in the theoretical part of this work (sec. 2.3.2), factorization is only proven for longitudinally polarized photons. As a result of this, only calculations for longitudinally polarized ρ^0-mesons are available. This analysis did not disentangle longitudinally and transversely polarized ρ^0-mesons, which is why it first has to be ensured that longitudinally polarized ρ^0-mesons dominate in the region of interest.

Longitudinally and Transversely Polarized ρ^0-Mesons

Figure 6.4 gives the ratio $R = \frac{\sigma_L}{\sigma_T}$ for different kinematical regions of the COMPASS experiment, with σ_L being the cross section for the longitudinally polarized mesons and σ_T being the cross section for the transversely polarized mesons. The figure shows that in the kinematical region of the present analysis ($Q^2 > 1$ (GeV/c)^2 and mean virtuality $\langle Q^2 \rangle = 2.10$ (GeV/c)^2) σ_L starts to dominate. Hence, the obtained results are comparable to the theoretical predictions.

Polarization of the ρ^0-Mesons in different Q^2 Bins

In order to know which bins are suited best for a comparison with theoretical predictions, a check of the polarization for the different bins in Q^2 is performed.
As mentioned in section 2.3.2, the polarization of the ρ^0-mesons can be determined by looking at the angular distribution of the decay $\rho^0 \to \pi^+\pi^-$. To get information about the fraction of longitudinally polarized mesons in the different Q^2 bins, the $\cos\theta$ distribution is calculated with one of the two following formulas

$$\cos\theta = \frac{\vec{\pi}^+_{RF} \cdot (-\vec{N'}_{RF})}{|\vec{\pi}^+_{RF}| \cdot |\vec{N}_{RF}|} = \frac{\vec{\pi}^+_{RF} \cdot \vec{\rho}_{lab}}{|\vec{\pi}^+_{RF}| \cdot |\vec{\rho}_{lab}|}. \tag{6.3}$$

In this formula, θ is defined in the ρ^0-rest frame as the angle between the momentum-vector of the positive pion π^+_{RF} and the negative direction of the momentum-vector of the recoiling target particle N'_{RF} (see figure 6.5). $\vec{\rho}_{lab}$ is the momentum-vector of the ρ^0-meson in the laboratory frame. The equality of the two formulas is proven in [10].

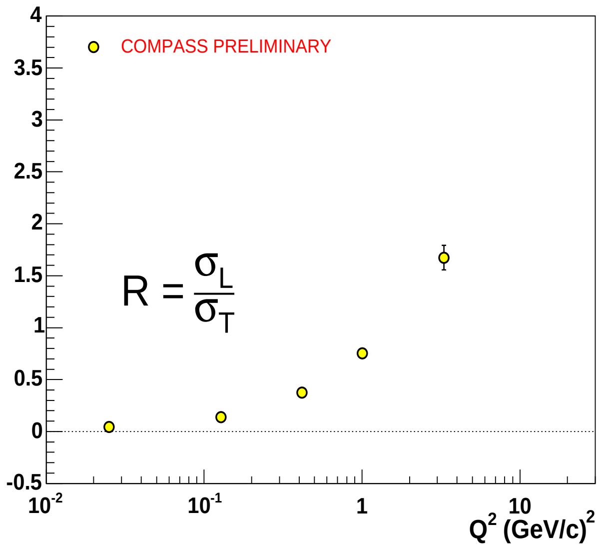

Figure 6.4: Ratio $R = \frac{\sigma_L}{\sigma_T}$ for different kinematical regions of the COMPASS experiment, with σ_L being the cross section for the longitudinally polarized mesons and σ_T being the cross section for the transversely polarized mesons. For the present analysis the range $Q^2 > 1(GeV/c)^2$ is interesting, and a mean virtuality of $\langle Q^2 \rangle = 2.10\ (\mathrm{GeV/c})^2$ is obtained. In this kinematical range the longitudinally polarized cross section dominates. Figure taken from [30].

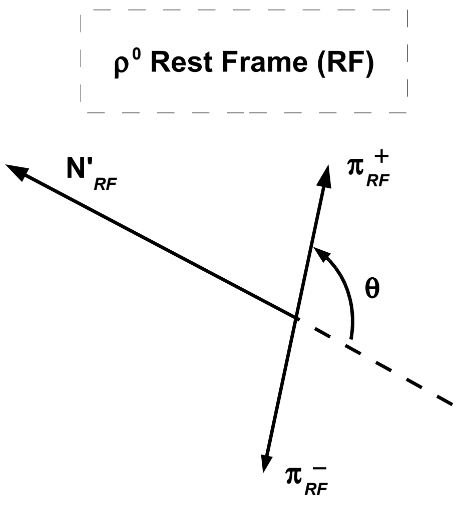

Figure 6.5: Definition of the angle θ in the ρ^0-rest frame as the angle between the momentum-vector of the positive pion and the negative direction of the momentum-vector of the recoiling particle.

The $\cos\theta$ distributions for the five different bins in Q^2 are shown in figure 6.6. It is important to notice that for the used data no acceptance correction is performed. From the shape of these five distributions it can be concluded that for higher values of Q^2 the fraction of longitudinally polarized ρ^0-mesons increases [30]: If the shape is a constant line, there would be an equal share of longitudinally and transversely mesons. If the shape is concave upwards, this would be a sign for a bigger amount of transversely polarized mesons. In the present case, with a concave downwards shape, there are more longitudinally polarized mesons than transversely polarized mesons. Thus, from figure 6.6 it can be concluded that longitudinally polarized ρ^0-mesons dominate in all five bins of Q^2, and, especially in the highest bins, longitudinally polarized mesons are contained almost exclusively.

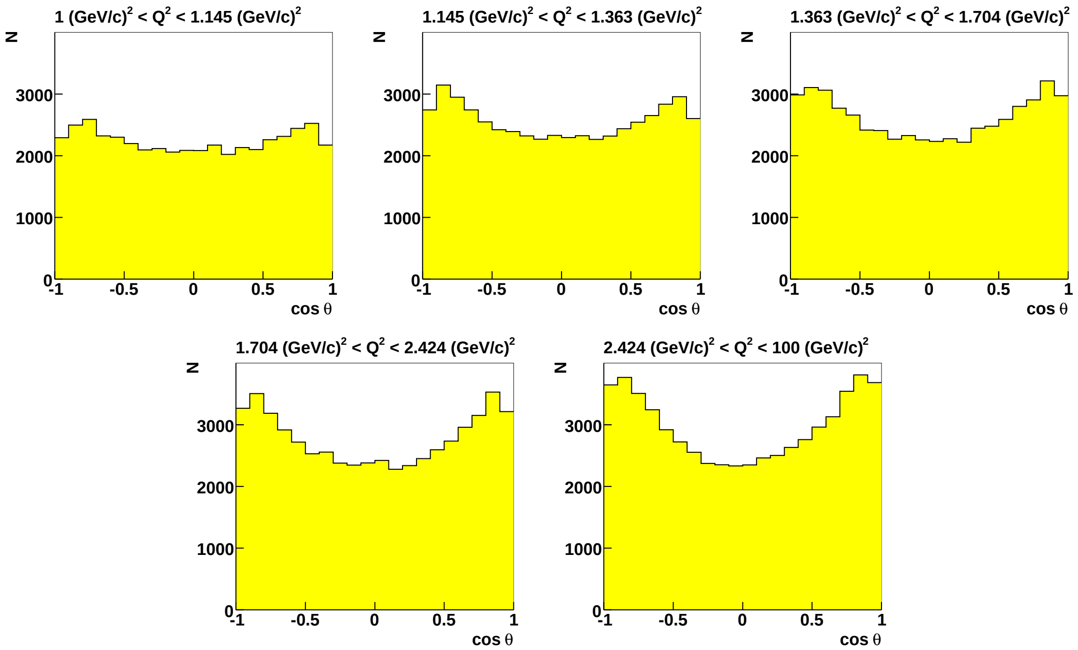

Figure 6.6: $\cos\theta$-distributions for the five different Q^2 bins. From the shape of these distributions it can be concluded that the fraction of longitudinally polarized ρ^0-mesons increases with higher values for Q^2, because the shape is getting more concave downwards with increasing Q^2. For the used data no acceptance correction is performed.

6.3.2 Comparison with Calculations from Goeke et al.

Goeke et al. calculated the total angular momentum J^q carried by the quarks in the proton, depending on the measured TTSA [18]. Their calculations assume the total angular momentum of the down-quarks to be zero ($J^d = 0$). For the total angular momentum of the up-quarks J^u they provide several calculations in different kinematical ranges. All calculations are performed for longitudinally polarized ρ^0-mesons.
To ensure that only TTSAs for longitudinally polarized mesons enter the comparison, and in order to fit the available kinematical ranges, two additional TTSAs in two

additional bins are calculated. These two bins, with specific cuts on Q^2, are presented in figure 6.7 with their $\cos\theta$-distribution and their mean kinematical values. For these bins, the TTSA in the kinematical variable x_{Bj} is calculated and compared to the values from [18].

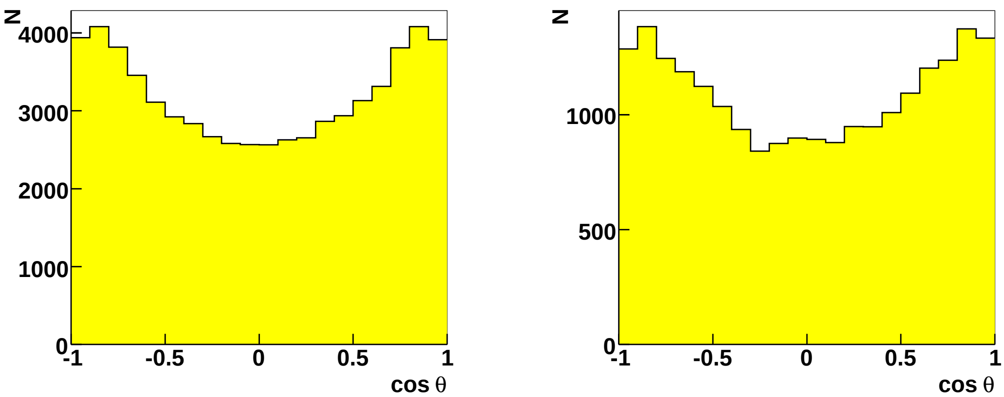

First additional Bin		
$2\ (\mathrm{GeV/c})^2 < Q^2 < 4\ (\mathrm{GeV/c})^2$		
$\langle Q^2 \rangle$	$=$	$2.68\ (\mathrm{GeV/c})^2$
$\langle -t' \rangle$	$=$	$0.130\ (\mathrm{GeV/c})^2$
$\langle p_T^2 \rangle$	$=$	$0.118\ (\mathrm{GeV/c})^2$
$\langle x_{Bj} \rangle$	$=$	0.048

Second additional Bin		
$4\ (\mathrm{GeV/c})^2 \leq Q^2 < 100\ (\mathrm{GeV/c})^2$		
$\langle Q^2 \rangle$	$=$	$6.30\ (\mathrm{GeV/c})^2$
$\langle -t' \rangle$	$=$	$0.178\ (\mathrm{GeV/c})^2$
$\langle p_T^2 \rangle$	$=$	$0.145\ (\mathrm{GeV/c})^2$
$\langle x_{Bj} \rangle$	$=$	0.110

Figure 6.7: Introduction of two additional bins with specific cuts on Q^2. Both bins are dominated by longitudinally polarized ρ^0-mesons, which can be concluded from the $\cos\theta$-distributions. The kinematical ranges are chosen in such a way that they fit to the calculations from [18].

Figure 6.8 compares the TTSAs from the two additional bins with the theoretical predictions obtained by [18]. On the upper part with their calculations based on the kinematical values $Q^2 = 2.5\ (\mathrm{GeV/c})^2$ and $-t = 0.25\ (\mathrm{GeV/c})^2$, and on the lower part with their calculations based on the kinematical values $Q^2 = 5\ (\mathrm{GeV/c})^2$ and $-t = 0.5\ (\mathrm{GeV/c})^2$. In both cases, the kinematical variables are slightly different to the ones obtained in this analysis (see figure 6.7), but in a comparable and tolerable range. When looking at the TTSAs for the two additional bins in this figures, it can be concluded that a positive value of $J^u = 0.4$ is proposed by the result for the total angular momentum of the up-quarks in the proton. It should be mentioned that the results of both additional bins are in good agreement.

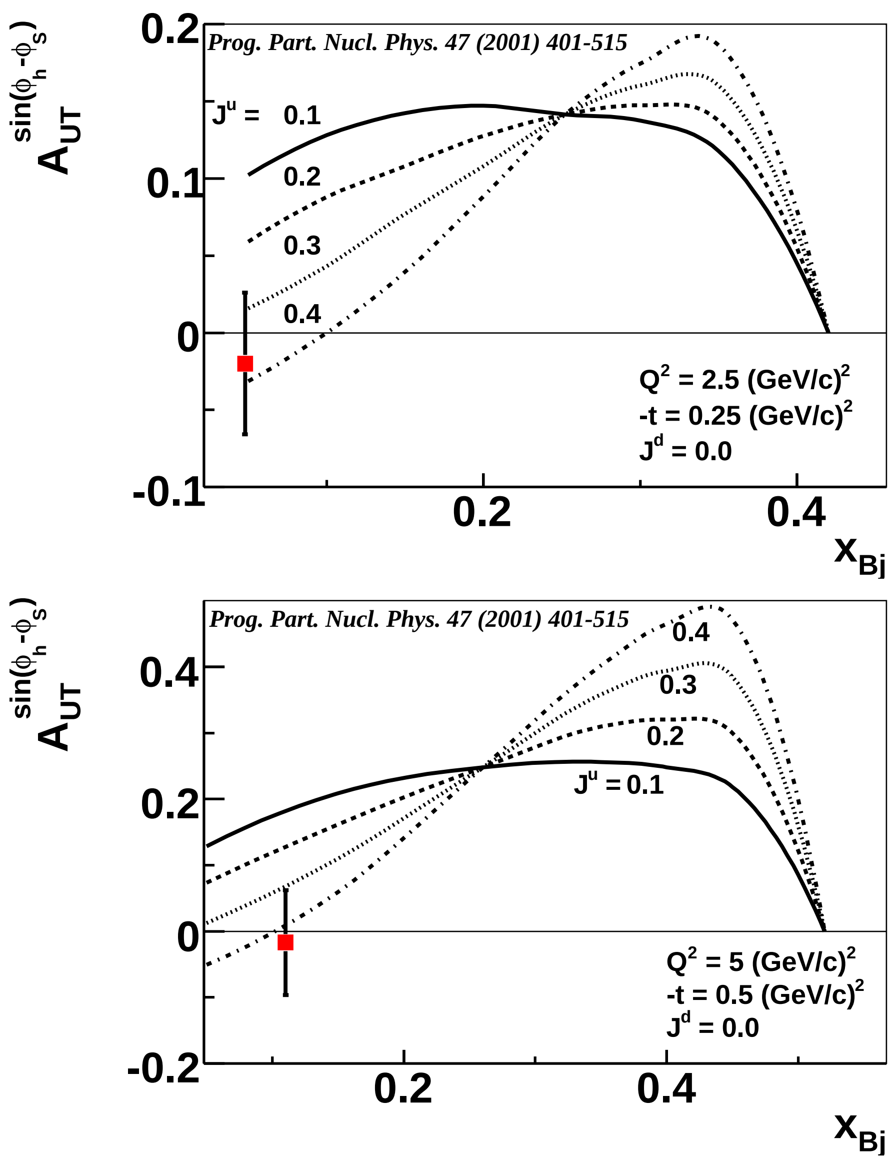

Figure 6.8: Comparison of the obtained TTSAs for the two additional bins, with theoretical predictions from Goeke et al [18]. The figure shows different calculations for the total angular momentum of the up-quarks in the proton: $J^u = 0.1$, $J^u = 0.2$, $J^u = 0.3$ and $J^u = 0.4$ ($J^d = 0.0$ is assumed for all cases). On the upper plot with calculations based on the kinematical values $Q^2 = 2.5\ (\mathrm{GeV/c})^2$ and $-t = 0.25\ (\mathrm{GeV/c})^2$, and on the lower plot calculations based on the kinematical values $Q^2 = 5\ (\mathrm{GeV/c})^2$ and $-t = 0.5\ (\mathrm{GeV/c})^2$. The comparison of these calculations with the obtained TTSAs shows that a positive values of $J^u = 0.4$ is proposed by the result in the present case.
It should be noted that [18] used another coordinate system than this thesis, which is why their calculations have to be adapted by introducing a factor of $-\pi/2$ [21].

6.4 Comparison with Calculations and Measurements from the HERMES Experiment

The HERMES experiment also measured the TTSA on a proton target for exclusive ρ^0-meson production [61]. Therefore, it is appropriate to compare the results from this thesis with the results from the HERMES experiment to search for overlaps and distinctions. Figures 6.9 and 6.10 present these comparisons. At the same time, calculations from [21] are presented in these figures, which show how the total angular momentum of up-quarks in the proton can be accessed with the help of elastic ρ^0 production at HERMES. The theoretical predictions are included by three values for the total angular momentum of up-quarks in the proton, namely $J^u = 0.0$, $J^u = 0.2$ and $J^u = 0.4$ ($J^d = 0.0$ is assumed in all three cases). From the comparison of the obtained TTSAs with this three calculations, it becomes obvious that the present analysis favors positive values for J^u.

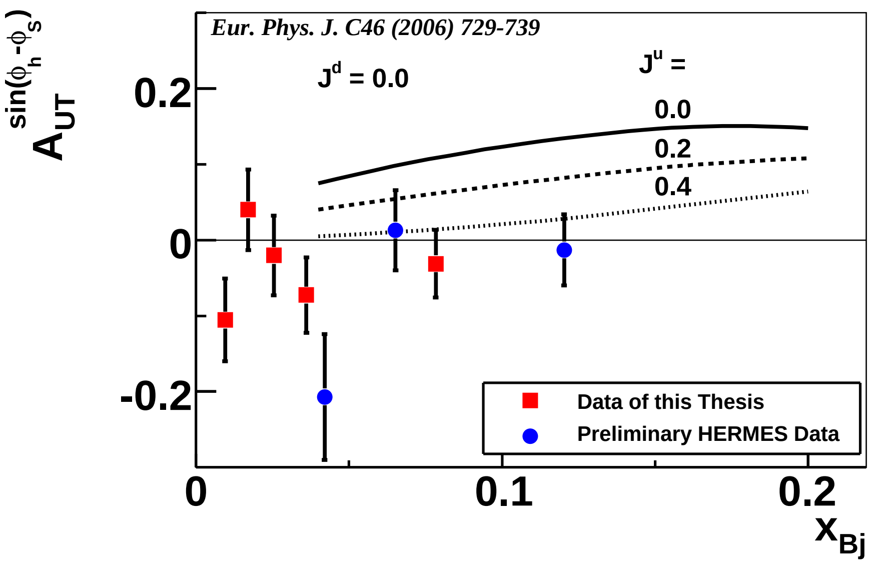

Figure 6.9: Comparison of the obtained TTSAs with theoretical predictions and measurements for x_{Bj} obtained at HERMES. Different predictions from [21] for the total angular momentum of the up-quarks in the proton ($J^u = 0.0$, $J^u = 0.2$, $J^u = 0.4$) are presented ($J^d = 0.0$ is assumed for all cases). The plot shows that positive values for J^u are favored.
Additionally, the plot shows results obtained at the HERMES experiment [61]. All values from the HERMES measurements are in very good agreement with the values obtained in this thesis.

As HERMES measures at another kinematical range than COMPASS, this also shows in the figures: COMPASS is more sensitive to smaller regions of x_{Bj} and higher regions of Q^2 (see figure 6.11). Nevertheless, the figures show that the results for x_{Bj} and $-t'$ from both analyses are within very good agreement in comparable kinematical ranges. This fact is also underlined by the additional comparison of the TTSAs for Q^2, given in figure 6.11.

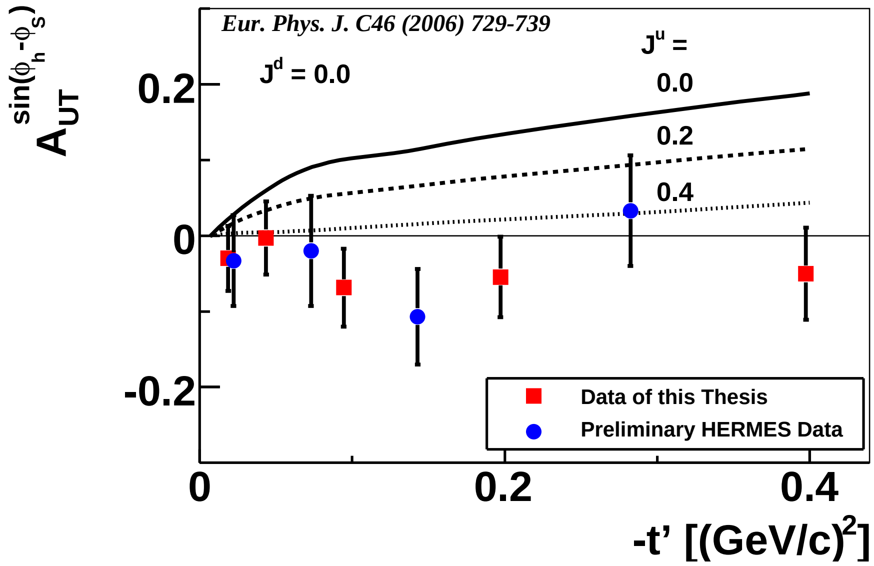

Figure 6.10: Comparison of the obtained TTSAs for $-t'$ with theoretical predictions and measurements from HERMES. For different total angular momentum of the up-quarks in the proton ($J^u = 0.0$, $J^u = 0.2$, $J^u = 0.4$) predictions from [21] are presented ($J^d = 0.0$ is assumed for all cases). The comparison shows that positive values for J^u are favored.
Additionally, the plot shows results from measurements from the HERMES experiment, which are all in very good agreement with the values obtained in this thesis.

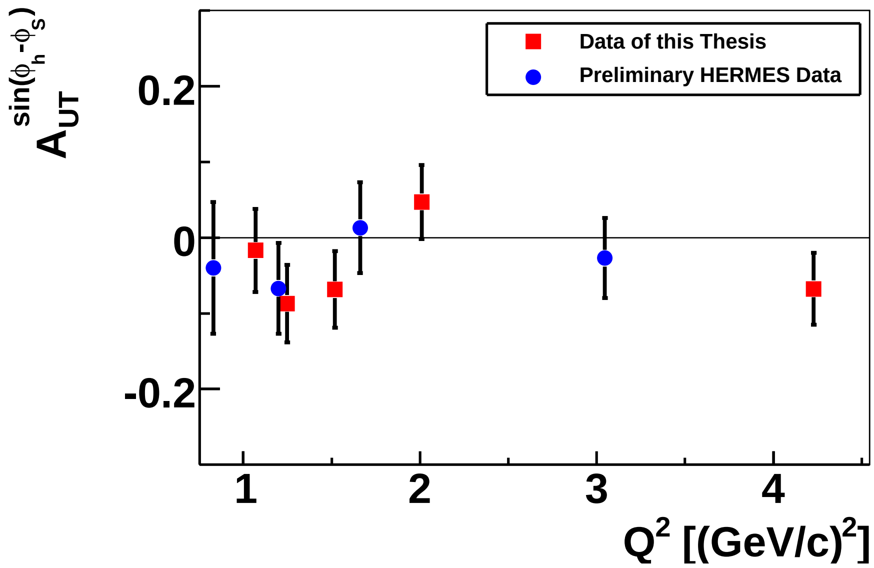

Figure 6.11: Comparison of the obtained TTSAs with measurements for Q^2 at the HERMES experiment. In addition to x_{Bj} and $-t'$, this figure shows a comparison of the TTSAs for Q^2. Again, both experiments are in good agreement within the comparable kinematical ranges.

6.5 Comparison with Data measured on a Deuteron Target at COMPASS

In recent years, COMPASS measured TTSAs on a deuteron target. An analysis for exclusively produced ρ^0-mesons was performed there as well [62]. The kinematical range is exactly the same for the former and the present analysis, which is why it is interesting to compare the two results. This comparison is given in figure 6.12.
The difference of the two TTSAs from the deuteron and the proton is interesting as well. This difference represents the TTSAs expected for the neutron. The plots in figure 6.12 show that non-zero values for the neutron TTSAs are indicated by the data.

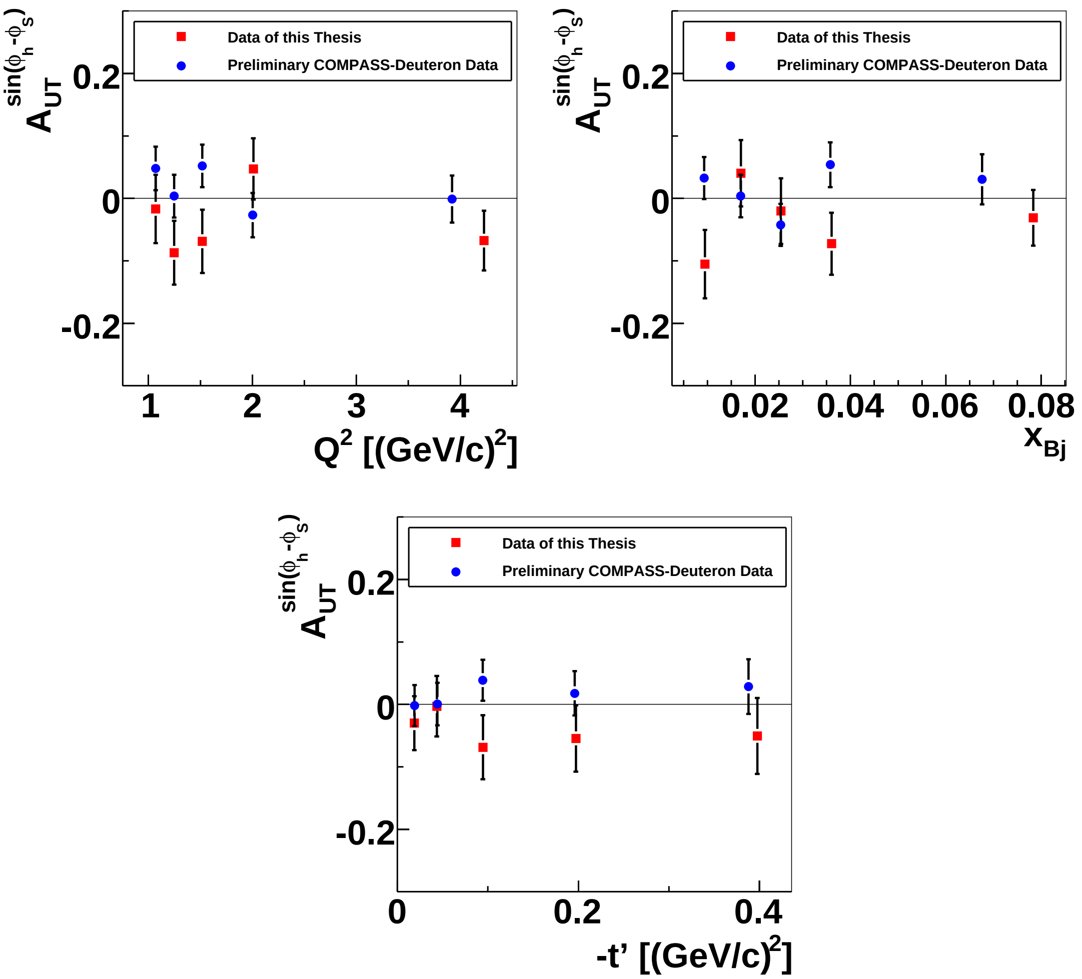

Figure 6.12: Comparison of the TTSAs from this thesis with results from a former COMPASS analysis on a deuteron target [62]. As the two analyses are obtained at the same kinematical range, it is interesting to compare the two results from the different targets. The TTSAs for the neutron would be the difference of the two TTSAs shown. Therefore, non-zero values for the TTSAs of the neutron are indicated by the data.

6.6 Outlook

As a final outlook, this section will mention some aspects which were not included in the main part of this thesis, because the main focus of this work was on extracting the asymmetry amplitude. Nevertheless, these aspects might provide interesting fields to study in the future.

- The comparison of the results from this work with theoretical descriptions shows that only calculations for higher values of x_{Bj} exist. Though, the kinematical range of COMPASS also covers the range of small x_{Bj} in which no theoretical calculations exist. Higher values of x_{Bj} give information about valence quarks, while lower values of x_{Bj} contain information about sea-quarks. Hence, it would be very interesting to obtain calculations in this range of small x_{Bj}, to derive more information about the total angular momentum of sea-quarks.
- The GPDs E and H were not explicitly calculated in this thesis. They were only included indirectly by using the work of [18] and [21], to obtain the total angular momentum of up-quarks in the proton. Especially the work of [18] gives many starting points for the direct calculation of the GPDs E and H. This calculation would be of special interest, because it would provide further information about the spatial distribution of the proton.
- Another topic for a future thesis could be an acceptance corrected disentanglement of the ρ^0-meson in its longitudinal and its transversal component ρ^0_L and ρ^0_T. It is mentioned at several points of this thesis that factorization only holds for longitudinally polarized photons. An analysis disentangling the transverse and the longitudinal part, and calculating their TTSA separately, would be very interesting. This thesis used a graphical way to separate the two parts. An analytic approach for separating these two parts can be found in [30]. There an acceptance correction with the use of Monte Carlo simulations is suggested.

When summarizing these aspects, it can be concluded that there are still many interesting points and fields to study in the exclusive production of ρ^0-mesons at the COMPASS experiment in the future.

7. Summary

The COMPASS experiment at CERN investigates the spin structure of the proton with a 160 GeV μ^+-beam. For this reason, a polarized NH_3 proton target was installed in the spectrometer to study Deep Inelastic Scattering events. The analysis performed for this thesis is based on data taken at the COMPASS experiment in 2007.

The aim of this thesis was to determine the Transverse-Target Single-Spin Asymmetry Amplitude $A_{UT}^{\sin(\phi_h-\phi_S)}$. At the COMPASS experiment, this amplitude is the physical observable to get access to Generalized Parton Distribution Functions. GPDs can be seen as combinations of form factors, parton densities and distribution amplitudes. Thus, they hold a huge potential to gain new information about the structure of the nucleon. In addition to that, Ji pointed out in his sum rule that GPDs can be used to determine the total angular momentum J^q carried by the quarks in the nucleon. Until today, the total angular momentum of the quarks is an unknown part of the spin puzzle, the formula to describe the spin structure of the nucleons.
Two channels exist to get access to GPDs: The Hard Exclusive Meson Production (HEMP) and the Deeply Virtual Compton Scattering (DVCS). This thesis was dedicated to the HEMP channel, especially to exclusively produced ρ^0-mesons.

To prepare the recorded data for the analysis, different studies have to be performed: Studies about the quality of the data, studies about the exact position of the proton target in the reference system of the COMPASS spectrometer and an extensive event selection of exclusively produced ρ^0-mesons.
The method used to extract the asymmetry amplitude from the prepared ρ^0-meson data sample was the so-called 2D Fit to Counts Method. This method performs a two dimensional fit and is using Poisson statistic. The implementation of this fit method lead to a minimization problem, which was solved with the help of the Levenberg-Marquardt-Algorithm, a mathematical tool for solving non-linear systems of equations.

The Transverse-Target Single-Spin Asymmetry Amplitude was extracted for eight kinematical variables, each divided into five different kinematical bin ranges. An overall integrated value for the asymmetry amplitude was calculated to:

$$A_{UT}^{\sin(\phi_h-\phi_S)} = -0.037 \pm 0.023.$$

This result is a significant asymmetry with a distance to zero of more than 1.5σ.

In this thesis, this result was compared to theoretical predictions from Goeke et al. and to experimental results as well as to calculations obtained at the HERMES experiment. The comparison with the theoretical predictions from Goeke et al. shows that

the obtained asymmetry amplitudes favor a positive value of about $J^u = 0.4$ for the total angular momentum carried by the up-quarks in the proton. In this calculations, the total angular momentum J^d for the down-quark in the proton is assumed to be zero. The comparison of the results from this thesis with data measured at the HERMES experiment shows that the HERMES data confirms the obtained results.
Therefore, the obtained results of this thesis give a hint for the fact that the missing part of the nucleon spin puzzle is carried by the total angular momentum of the quarks.

The COMPASS experiment has future plans for measuring GPDs. At the moment, extensive research and studies are performed in order to measure the Deeply Virtual Compton Scattering. From this channel, additional information about the nucleon structure can be expected. One day, this additional information might help to finally solve the spin puzzle.

A. Numerical Values for the calculated TTSAs and for the Binning

In section 6.1 the calculated TTSAs are given in figures. This appendix gives the associated numerical values for them. Additionally, the borders for the chosen binning are presented.

Table A.1: Numerical values for binning and TTSAs for x_{Bj}, Q^2 and p_T.

Bin	Bin Range	$\langle x_{Bj} \rangle$	TTSA	σ_{TTSA}
1	$0.0000 \leq x_{Bj} \leq 0.0132$	0.0095	−0.105	0.055
2	$0.0132 < x_{Bj} \leq 0.0210$	0.0170	0.040	0.053
3	$0.0210 < x_{Bj} \leq 0.0300$	0.0254	−0.020	0.052
4	$0.0300 < x_{Bj} \leq 0.0434$	0.0360	−0.073	0.050
5	$0.0434 < x_{Bj} \leq 2.0000$	0.0784	−0.031	0.045

Bin	Bin Range [(GeV/c)^2]	$\langle Q^2 \rangle$ [(GeV/c)^2]	TTSA	σ_{TTSA}
1	$1.000 \leq Q^2 \leq 1.145$	1.07	−0.017	0.055
2	$1.145 < Q^2 \leq 1.363$	1.25	−0.087	0.051
3	$1.363 < Q^2 \leq 1.704$	1.52	−0.069	0.051
4	$1.704 < Q^2 \leq 2.424$	2.01	0.047	0.049
5	$2.424 < Q^2 \leq 100.0$	4.23	−0.068	0.048

Bin	Bin Range [GeV/c]	$\langle p_T \rangle$ [GeV/c]	TTSA	σ_{TTSA}
1	$0.100 \leq p_T \leq 0.166$	0.132	−0.025	0.043
2	$0.166 < p_T \leq 0.253$	0.205	−0.019	0.046
3	$0.253 < p_T \leq 0.368$	0.307	−0.059	0.051
4	$0.368 < p_T \leq 0.548$	0.450	−0.046	0.051
5	$0.548 < p_T \leq 100.0$	0.620	−0.068	0.072

Table A.2: Numerical values for binning and TTSAs for y, p_T^2, $-t'$, E_{miss} and M_ρ.

Bin	Bin Range	$\langle y \rangle$	TTSA	σ_{TTSA}
1	$0.0 \leq y \leq 0.2$	0.141	−0.058	0.032
2	$0.2 < y \leq 0.3$	0.245	0.022	0.049
3	$0.3 < y \leq 0.4$	0.346	−0.037	0.066
4	$0.4 < y \leq 0.5$	0.446	−0.106	0.085
5	$0.5 < y \leq 2.0$	0.623	−0.015	0.074

Bin	Bin Range [(GeV/c)^2]	$\langle p_T^2 \rangle$ [(GeV/c)^2]	TTSA	σ_{TTSA}
1	$0.000 \leq p_T^2 \leq 0.029$	0.018	−0.025	0.043
2	$0.029 < p_T^2 \leq 0.063$	0.043	−0.019	0.046
3	$0.063 < p_T^2 \leq 0.135$	0.095	−0.059	0.051
4	$0.135 < p_T^2 \leq 0.279$	0.205	−0.046	0.051
5	$0.279 < p_T^2 \leq 100.0$	0.387	−0.068	0.072

Bin	Bin Range [(GeV/c)^2]	$\langle -t' \rangle$ [(GeV/c)^2]	TTSA	σ_{TTSA}
1	$0.000 \leq -t' \leq 0.029$	0.019	−0.030	0.043
2	$0.029 < -t' \leq 0.063$	0.043	−0.003	0.049
3	$0.063 < -t' \leq 0.135$	0.094	−0.069	0.051
4	$0.135 < -t' \leq 0.279$	0.197	−0.055	0.053
5	$0.279 < -t' \leq 100.0$	0.398	−0.050	0.061

Bin	Bin Range [GeV]	$\langle E_{miss} \rangle$ [GeV]	TTSA	σ_{TTSA}
1	$-2.500 \leq E_{miss} \leq -1.072$	−1.604	−0.073	0.067
2	$-1.072 < E_{miss} \leq -0.410$	−0.712	0.014	0.060
3	$-0.410 < E_{miss} \leq 0.226$	−0.082	−0.039	0.051
4	$0.226 < E_{miss} \leq 1.104$	0.649	−0.065	0.044
5	$1.104 < E_{miss} \leq 2.500$	1.742	−0.023	0.043

Bin	Bin Range [GeV/c^2]	$\langle M_\rho \rangle$ [GeV/c^2]	TTSA	σ_{TTSA}
1	$0.400 \leq M_\rho \leq 0.673$	0.598	−0.035	0.053
2	$0.673 < M_\rho \leq 0.736$	0.708	−0.070	0.052
3	$0.736 < M_\rho \leq 0.780$	0.758	−0.011	0.051
4	$0.780 < M_\rho \leq 0.843$	0.808	−0.074	0.050
5	$0.843 < M_\rho \leq 1.100$	0.924	−0.011	0.048

Bibliography

[1] M. Gell-Mann. *A schematic model of baryons and mesons.* Phys. Lett. **8** (1964) 214-215.

[2] G. Zweig. *An SU(3) model for strong interaction symmetry and its breaking.* CERN Report CERN-TH-401 and CERN-TH-412 (1964).

[3] European Muon Collaboration. *A measurement of the spin asymmetry and determination of the structure function g_1 in deep inelastic muon proton scattering.* Phys. Lett. **B206** (1988) 364-370.

[4] R.L. Jaffe and A. Manohar. *The g_1 problem: Deep inelastic electron scattering and the spin of the proton.* Nucl. Phys. **B337** (1990) 509-546.

[5] The COMPASS Collaboration. *The deuteron spin-dependent structure function g_1^d and its first moment.* Phys. Lett. **B647** (2007) 8-17, [hep-ex/0609038v2].

[6] D. Mueller et al. *Wave Functions, Evolution Equations and Evolution Kernels from Light-Ray Operators of QCD.* Fortschr. Phys. **42** (1994) 101-141, [hep-ph/9812448].

[7] A.V. Radyushkin. *Nonforward Parton Distributions.* Phys. Rev. **D56** (1997) 5524-5557, [hep-ph/9704207].

[8] X. Ji. *Gauge-Invariant Decomposition of Nucleon Spin.* Phys. Rev. Lett. **78** (1997) 610-613, [hep-ph/9603249].

[9] COMPASS Collaboration. *COMPASS: A Proposal for a Common Muon and proton Apparatus for Structure and Spectroscopy.* CERN-SPSLC-96-14 (1996).

[10] J. Kiefer. *First Measurement of the Transverse-Target Single-Spin Asymmetry in Exclusive Muon-production of ρ^0 Mesons at COMPASS.* Diploma thesis (2007) Universität Freiburg.

[11] J.C. Collins, D.E. Soper, and G. Sterman. *Factorization of hard processes in QCD.* Adv. Ser. Direct. High Energy Physics. **5** (2004) 1-91, [hep-ph/0409313].

[12] R. Devenish and A. Cooper-Sarkar. *Deep Inelastic Scattering.* Oxford University Press (2004).

[13] J.D. Bjorken and E.A. Paschos. *Inelastic Electron Proton and Gamma Proton Scattering and the Structure of Nucleon.* Phys. Rev. **185** (1969) 1975-1982.

[14] C.G. Callan and D.J. Gross. *High-Energy Electroproduction and the Constitution of the Electric Current.* Phys. Rev. Lett. **22** (1969) 156-159.

[15] X. Ji et al. *QCD Factorization for Semi-Inclusive Deep-Inelastic Scattering at Low Transverse Momentum.* Phys. Rev. **D71** (2005) 034005, [hep-ph/0404183].

[16] COMPASS Collaboration. *A new measurement of the Collins and Sivers asymmetries on a transversely polarised deuteron target.* Nucl. Phys. **B765** (2007) 31-70, [hep-ex/0610068].

[17] W. Käfer. *Measurements of Unpolarized Azimuthal Asymmetries at COMPASS.* Transversity 2008 proceedings (2008), arXiv:0808.0114v1 [hep-ex].

[18] K. Goeke, M.V. Polyakov, and M. Vanderhaeghen. *Hard Exclusive Reactions and the Structure of Hadrons.* Prog. Part. Nucl. Phys. **47** (2001) 401-515, [hep-ph/0106012].

[19] M. Diehl. *Generalized Parton Distributions.* Phys. Rept. **388** (2003) 41-277, [hep-ph/0307382].

[20] A.V. Belitsky and A.V. Radyushkin. *Unraveling hadron structure with generalized parton distributions.* Phys. Rept. **418** (2005) 1-387, [hep-ph/0504030v3].

[21] F. Ellinghaus et al. *Can the angular momentum of u-quarks in the nucleon be accessed at HERMES?* Eur. Phys. J. **C46** (2006) 729-739, [hep-ph/0506264v1].

[22] M. Diehl et al. *Linking parton Distributions to Form Factors and Compton Scattering.* Eur. Phys. J. **C8** (1999) 409-434, [hep-ph/9811253].

[23] B.W. Filippone and X. Ji. *The Spin Structure Of The Nucleon.* Adv. Nucl. Phys. **26** (2001) 1-88, [hep-ph/0101224].

[24] J.C. Collins, L. Frankfurt, and M. Strikman. *Factorization for hard exclusive electroproduction of mesons in QCD.* Phys. Rev. **D58** (1997) 2982-3006, [hep-ph/9611433].

[25] NMC Collaboration. *Exclusive ρ^0 and ϕ muonproduction at large Q^2.* Nucl. Phys. **B429** (1994) 503-529.

[26] E665 Collaboration. *Diffractive production of ρ^0(770) mesons in muon-proton interactions at 470 GeV.* Z. Phys. **C74** (1997) 237-261.

[27] ZEUS Collaboration. *Measurement of the spin-density matrix elements in exclusive electroproduction of ρ^0 mesons at HERA.* Eur. Phys. J. **C12** (2000) 393-410.

[28] H1 Collaboration. *A measurement of the t dependence of the helicity structure of diffractive ρ meson electroproduction at HERA.* Phys. Lett. **B539** (2002) 25-39.

[29] O.A. Grajek, A. Korzenev, and A. Sandacz. *Exclusive ρ^0 and ϕ production from COMPASS 2002 data.* COMPASS Note 2002-15 (2002).

[30] E. Burtin et al. *Angular distributions and $R = \sigma_L/\sigma_T$ for exclusive ρ^0 production.* COMPASS Note 2004-12 (2004).

[31] W.-M. Yao et al. *Review of Particle Physics.* J. Phys. **G33** (2006) 1-1232 `http://pdg.lbl.gov`.

[32] COMPASS Collaboration. *Outline For Generalized Parton Distribution Measurements With COMPASS At CERN.* CERN Report CERN-SPSC-2005-007 (2005).

[33] F. Hermann. *Status of the GANDALF board and studies for the RPD readout.* Talk given at the COMPASS GPD meeting (23.04.08) `http://lxfsrb6103.cern.ch/compass/gpd/meetings/200804_avril23/`.

[34] L. Mankiewicz, G. Piller, and T. Weigl. *Hard Exclusive Meson Production and Nonforward Parton Distributions.* Eur. Phys. J. **C5** (1998) 119-128, [hep-ph/9711227].

[35] M. Vanderhaeghen, P.A.M. Guichon, and M. Guidal. *Hard Electroproduction of Photons and Mesons on the Nucleon.* Phys. Rev. Lett. **80** (1998) 5064-5067.

[36] COMPASS Collaboration. *The COMPASS Experiment at CERN.* Nucl. Instr. Meth. **A577** (2007) 455-518, [hep-ex/0703049].

[37] COMPASS Collaboration. *The upgraded muon beam at the SPS.* Nucl. Instr. Meth. **A343** (1994) 351-362.

[38] G. Abragam and M. Goldman. *Principles of dynamic nuclear polarisation.* Rep. Prog. Phys. **41** (1999) 395-467.

[39] COMPASS Target Group. *40 mm NH3 target 2007 v0.1.* `http://wwwcompass.cern.ch/compass/detector/target/Drawings/NH3target07v01.pdf`.

[40] E. Albrecht et al. *COMPASS RICH-1.* Nucl. Instr. Meth. **A502** (2003) 112-116.

[41] C. Bernet et al. *The COMPASS trigger system for muon scattering.* Nucl. Instr. Meth. **A550** (2005) 217-240.

[42] H. Fischer et al. *Implementation of the dead-time free F1 TDC in the COMPASS detector readout.* Nucl. Instr. Meth. **A461** (2001) 507-510.

[43] H. Fischer et al. *The COMPASS data acquisition system.* IEEE Trans. Nucl. Sci. **49** (2002) 443-447.

[44] B. Gobbo. *CORAL web page.* `http://coral.web.cern.ch/coral/`.

[45] S. Gerassimov. *PHAST web page.* `http://ges.home.cern.ch/ges/phast/`.

[46] R. Brun et al. *ROOT User Guide 5.16.* `http://root.cern.ch/`.

[47] J. Barwind. *Target position during 2007 transversity data taking.* Talk given at the COMPASS Analysis meeting (28.02.08) `http://lxfsrb6103.cern.ch/compass/software/analysis/transparencies/2008/am_080228/`.

[48] The Transversity Group. *Collins and Sivers asymmetries from 2007 proton transverse run.* COMPASS Note 2008-10 (2008).

[49] H. Wollny. *Data Quality and Unbinned Estimator.* Talk given at the COMPASS Transversity meeting (25.07.08) `http://acid01.ts.infn.it/transversity/transv/meetings/m080725/wollny_2008_07_25.pdf`.

[50] M. Stolarski. *SM2 Yoke Problem.* Talk given at the COMPASS Analysis meeting (20.05.08) `http://lxfsrb6103.cern.ch/compass/software/analysis/transparencies/2008/am_080520/`.

[51] A. Sandacz. *Separation of coherent and incoherent exclusive processes.* Talk given at the COMPASS Analysis meeting (02.08.07) `http://lxfsrb6103.cern.ch/compass/software/analysis/transparencies/2007/am_070802/`.

[52] H. Fischer. *Private communications, July 2008.*

[53] G. Mallot. *Principle of a bias-free "2D" transverse asymmetry fit.* Talk given at the COMPASS analysis meeting (11.09.2007) `http://lxfsrb6103.cern.ch/compass/software/analysis/transparencies/2007/am_070911/`.

[54] K. Levenberg. *A Method for the Solution of Certain Problems in Least Squares.* Quart. Appl. Math. **2** (1944) 164-168.

[55] D.W. Marquardt. *An Algorithm for Least-Squares Estimation of Nonlinear Parameters.* J. Soc. Indust. Appl. Math. **11** (1963) 431-441.

[56] A. Vossen. *Transverse Spin Asymmetries at the COMPASS Experiment.* PhD thesis (2008) Universität Freiburg.

[57] B. Gough. *GNU Scientific Library Reference Manual -2nd Edition.* Network Theory Ltd. (2003).

[58] A. Kotzinian. *Remarks on acceptance effects in asymmetry extraction.* COMPASS Note 2007-02 (2007).

[59] A. Sandacz. *Resolutions for 'transverse' variables in ρ^0 production.* Talk given at the COMPASS Analysis meeting (15.01.08) `http://lxfsrb6103.cern.ch/compass/software/analysis/transparencies/2008/am_080115/sandacz_080115.pdf`.

[60] M. Goeckeler et al. *Generalized Parton Distributions from Lattice QCD.* Phys. Rev, Lett. **92** (2004) 042002.

[61] A. Rostomyan and J. Dreschler. *Transverse Target-Spin Asymmetry of Exclusive ρ^0 Meson Production on Proton at HERMES.* DIS2007 proceedings (2007), arXiv:0707.2486v1 [hep-ex].

[62] COMPASS Collaboration. *Extraction of Transverse Target Single Spin Asymmetry for Exclusive ρ^0 Production from COMPASS 2002-2004.* COMPASS Note 2007-09 (2007).

Deutschsprachige Zusammenfassung

Seit bekannt ist, dass das Nukleon eine komplexe Substruktur besitzt, wurden viele experimentelle und theoretische Untersuchungen durchgeführt, um diese Substruktur genauer zu verstehen. So konnte das Stanford Linear Accelerator Center (SLAC) im Jahr 1970 das von Gell-Mann und Zweig vorgeschlagene Quark-Modell bestätigen. Allerdings ist die Zusammensetzung des Spin des Nukleons aus den Helizitäten seiner Konstituenten bis heute ein Rätsel. Als 1983 die European Muon Collaboration (EMC) herausfand, dass der Spin der Quarks nur 30% zum Spin des Nukleon beiträgt, kam es zur sogenannten Spin-Krise, welche sogar das Quark-Modell in Frage stellte. Heutzutage gilt für die Zusammensetzung des Nukleonspin die Summenregel von Jaffe und Manohar:

$$\frac{1}{2}\hbar = \frac{1}{2}\Delta\Sigma + \Delta G + L_q + L_g.$$

Doch wie groß die Nukleonspin-Anteile der Helizitäten $\Delta\Sigma$ der Quarks und ΔG der Gluonen, beziehungsweise die Anteile deren Drehimpulse L_q und L_g sind, ist noch nicht genau bekannt. Während für die Anteile der Helizitäten der Quarks und Gluonen Messwerte existieren ($\Delta\Sigma \approx 0.3$, $\Delta G \approx 0.25$), sind die Anteile der Drehimpulse völlig unbestimmt.
Erst mit den im Jahr 1994 eingeführten generalisierten Partonverteilungensfunktionen (GPDs) wurde eine Möglichkeit gefunden, um mit der Summenregel von Ji den Gesamtdrehimpuls J^q der Quarks und J^g der Gluonen zu bestimmen. Zur Messung von GPDs gibt es dabei zwei Kanäle: Die harte exklusive Erzeugung von Mesonen (HEMP) und die tief-virtuelle Comptonstreuung (DVCS).

Die vorliegende Arbeit beschäftigte sich mit der harten exklusiven Erzeugung von Mesonen, insbesondere mit der Erzeugung von ρ^0-Mesonen. Ziel der Arbeit war es dabei, die Amplitude $A_{UT}^{\sin(\phi_h-\phi_S)}$ der sogenannten "Transverse-Target Single-Spin Asymmetrie" zu extrahieren, welche die physikalische Observable zur Bestimmung von GPDs darstellt. Hierbei wurden 2007 am COMPASS-Experiment aufgezeichnete Daten verwendet.
Das COMPASS-Experiments untersucht am CERN in Genf die Spinstruktur des Nukleons. Zur Messung der tief-unelastischen Streuung wird dabei ein 160-GeV-μ^+-Strahl sowie eine polarisierte NH_3-Protonprobe verwendet.
Hauptgegenstand der durchgeführten Analyse war, neben Überprüfungen der Qualität der Daten und der Selektion der ρ^0-Mesonen aus dem verfügbarem Datensatz, die Implementierung einer Zählratenfitmethode zur Extraktion der Asymmetrie. Diese Fitmethode, welche Poissonstatistik verwendet und in zwei Dimensionen durchgeführt wird,

führt zu einem Minimalisierungsproblem, welches mit Hilfe des Levenberg-Marquardt-Algorithmus gelöst wurde, einem mathematischen Instrument zum Lösen nicht-linearer Gleichungssysteme.

Die Asymmetrie wurde für acht kinematische Variable extrahiert, wobei jede in fünf unterschiedliche kinematische Bereiche unterteilt wurde. Das Ergebnis für eine über alle Bereiche integrierte Asymmetrie ergibt sich dabei zu:

$$A_{UT}^{\sin(\phi_h - \phi_S)} = -0.037 \pm 0.023.$$

Dieses Ergebnis stellt eine signifikante Asymmetrie dar mit einen Abstand von über 1.5σ zur Null.

Die Werte der Asymmetrien zeigen bei einem Vergleich mit theoretischen Vorhersagen von Goeke et al., dass für den Gesamtdrehimpuls der up-Quarks im Proton ein Wert von $J^u = 0.4$ angenommen werden kann, wobei in den Rechnungen von einem Gesamtdrehimpuls $J^d = 0$ der down-Quarks ausgegangen wird. Der Vergleich mit Messungen und theoretischen Voraussagen welche am HERMES Experiment erzielt wurden bekräftigt dieses Resultat und bestätigt die Richtigkeit der durchgeführten Messungen. Somit kann gefolgert werden, dass das in dieser Diplomarbeit erzielte Ergebnis einen Hinweis dafür liefert, dass der fehlende Teil des Spin-Rätsels im Gesamtdrehimpuls der Quarks zu finden ist.

Auch in der Zukunft werden am COMPASS-Experiment generalisierte Partonverteilungensfunktionen untersucht werden. Im Moment werden intensive Studien und Entwicklungsarbeiten betrieben, um die tief-virtuelle Comptonstreuung zu messen. Von diesem Kanal werden weitere Informationen über die Struktur des Nukleons erwartet, sodass eines Tages mithilfe dieser Messungen das Spin-Rätsel endgültig gelöst werden könnte.

Acknowledgements

Als Abschluss dieser Arbeit möchte ich noch einigen Personen meinen Dank aussprechen, ohne deren Hilfe diese Diplomarbeit in dieser Weise nicht zustandegekommen wäre:

- Prof. Horst Fischer für die fachlich und menschlich hervorragende Betreuung während meiner Diplomarbeit. Zudem für das Vertrauen und Verständnis dass er mir in dieser Zeit entgegengebracht hat.
- Prof. Kay Königsmann für meine Aufnahme in seine Arbeitsgruppe.
- Heiner Wollny für unzählige hilfreiche Tipps und Tricks beim alltäglichen Kampf mit PHAST, C++, ROOT, LaTeX, Linux, COMPASS, etc. Durch sein nahezu niemals endendes Wissen in diesen Gebieten hat er großen Anteil an dieser Arbeit. Vielen Dank!
- Wolfgang Käfer für die geduldige Beantwortung vieler Anfängerfragen, v.a. über PHAST, ROOT und die theoretischen Sachverhalte der COMPASS-Physik.
- Jasmin Kiefer für eine Einführung in die CERN-Welt.
- The whole COMPASS collaboration, especially the Transversity- and the GPD-subgroups for giving me the chance to taste the wonderous world of science.
- Den Probelesern meiner Arbeit: Andreas Mutter, Christian Schill und Heiner Wollny.
- Der ganzen Abteilung Königsmann für ein sehr angenehmes Arbeitsklima bei Seminaren, Mittagessen, CERN-Aufenthalten und überhaupt: Andreas, Anselm, Christian, Donghee, Donghwa, Florian, Frank, Heiner, Horst, Jasmin, Julia, Jürgen, Kay, Khalil, Konrad, Louis, Rainer, Roland, Sebastian, Tillmann, Wolfgang.
- Simone, Florian, Moritz, Jannes und Josip für die Jahre des Studiums.
- Julia Boos für die schwere Stunden die sie mit mir und all den physikalischen Fachausdrücken und umständlichen Satzkonstruktionen verlebt hat. Darüberhinaus für den Rückhalt und die Abwechslung in meinem Leben außerhalb der Physik.
- Meinen Eltern und meinem Bruder, die meine Entscheidung ein Zweitstudium in Physik zu beginnen nie in Frage gestellt haben. Genauso wie sie mich in meinen Entscheidungen und Handlungen immer unterstützt und bestätigt haben, was mir erst ermöglicht hat mein Studium zu beenden. Dankeschön!

Erklärung

Diese Arbeit ist von mir selbständig verfasst worden und ich habe keine anderen als die angegebenen Quellen als Hilfsmittel verwendet.

Jochen Barwind, Oktober 2008